INTERFERENCE SUPPRESSION USING KNOWLEDGE-AIDED SUBARRAY PATTERN SYNTHESIS

THESIS

David A. New, 1st Lt, USAF

AFIT-ENG-MS-16-M-037

DEPARTMENT OF THE AIR FORCE
AIR UNIVERSITY

AIR FORCE INSTITUTE OF TECHNOLOGY

Wright-Patterson Air Force Base, Ohio

AFIT-ENG-MS-16-M-037

INTERFERENCE SUPPRESSION USING KNOWLEDGE-AIDED SUBARRAY PATTERN SYNTHESIS

THESIS

Presented to the Faculty

Department of Electrical and Computer Engineering

Graduate School of Engineering and Management

Air Force Institute of Technology

Air University

Air Education and Training Command

in Partial Fulfillment of the Requirements for the

Degree of Master of Science in Electrical Engineering

David A. New, B.S.E.E.

1st Lt, USAF

March 2016

AFIT-ENG-MS-16-M-037

INTERFERENCE SUPPRESSION USING KNOWLEDGE-AIDED SUBARRAY PATTERN SYNTHESIS

THESIS

David A. New, B.S.E.E.
1st Lt, USAF

Committee Membership:

Lt Col Phillip Corbell, PhD
Chair

Dr. Julie Jackson
Member

Lt Col Jeremy Stringer, PhD
Member

AFIT-ENG-MS-16-M-037

Abstract

Most phased array systems subarray many antenna elements into far fewer digitized channels. While having more degrees of freedom (DOF) yields better performance, adding channels to create more digital DOF increases system cost and data throughput requirements. A subarray itself constitutes a phased array with as many DOF as it has antenna element weights. Typically, only one degree of freedom is used to steer the maximum gain direction of the subarray pattern. For typical antenna geometries a single subarray will provide many more spatial DOF than there are digitized channels. The inherent DOF of the subarrays could be used to mitigate selected interference signals with the subarray pattern if the antenna manifold, the angle of arrival (AOA), and the power of interference sources at the array face are known. Interference AOA and power can be derived from external knowledge sources (e.g., intelligence, additional sensor packages, monopulse beams) or can also be found by processing channel data. The AOA and power estimates can then be used to adapt a subarray pattern to null interference and restore dynamic range while allowing digital DOF to be utilized for other purposes (such as clutter mitigation). Simulations are used to illustrate the implementation tradeoffs and a proposed concept of operations for dividing spatial nulling duties between subarray and digital beamformers, referred to herein as Knowledge-Aided Subarray Pattern Synthesis (KASPS). Performance is simulated for multiple antenna geometries and interference parameters. The technique is shown to outperform conventional digital-only adaption for subarrayed antennas and approach optimum performance bounds under some conditions. KASPS is shown to improve performance even with misestimated interference parameters, unknown manifold error, and quantized subarray weights.

AFIT-ENG-MS-16-M-037

This thesis is dedicated to my fiancé for her love and support throughout my Master's education, my parents for instilling strong scholastic values within me from an early age, and my sisters for their consistently inspiring example.

Acknowledgements

I would like to acknowledge my research advisor for affording me this opportunity to take the first steps on his "big idea," and for guiding me through the entire process. I would like to acknowledge my committee members for their essential feedback on delivering my research. Finally, I would like to acknowledge my fellow AFIT radar students- we learned and labored together.

David A. New

Table of Contents

Page

List of Figures

List of Tables

INTERFERENCE SUPPRESSION USING
KNOWLEDGE-AIDED SUBARRAY PATTERN SYNTHESIS

I. Introduction

Many modern phased array antennas consist of many more antenna elements than digitized channels (i.e. the number of analog-to-digital converters (ADCs)). The number of elements is determined by the desired beamwidth, gain, monopulse accuracy, etc. while the number of channels is typically dictated by the application (Moving Target Indication (MTI), angle of arrival (AOA) information, number of simultaneous communication channels, Synthetic Aperture Radar (SAR), etc.) and a set of Electronic Protection (EP) requirements. Connecting elements to channels is the antenna manifold. The antenna manifold is comprised of the analog network of combiners, phase shifters or time delays, amplifiers, and attenuators that constitute subarrays feeding each channel. Subarrays must be dynamically steered in the direction of interest in real time, effectively forming a real beampattern through which each channel receives electromagnetic data. The channel data then enters the signal processing chain responsible for adaptively canceling interference, finding moving targets, measuring signal AOA, etc. A notional concept of the system processing chain can be seen in Figure 1.

The number of channels, C, of a phased array antenna sets the system's number of digital degrees of freedom (DOF), $C-1$. The number of digital DOF has a strong correlation to system capability, performance, robustness, and system cost. The ideal scenario of having a dedicated ADC behind every antenna element is only warranted (or possible) in a small handful of phased array systems due to the high cost. The

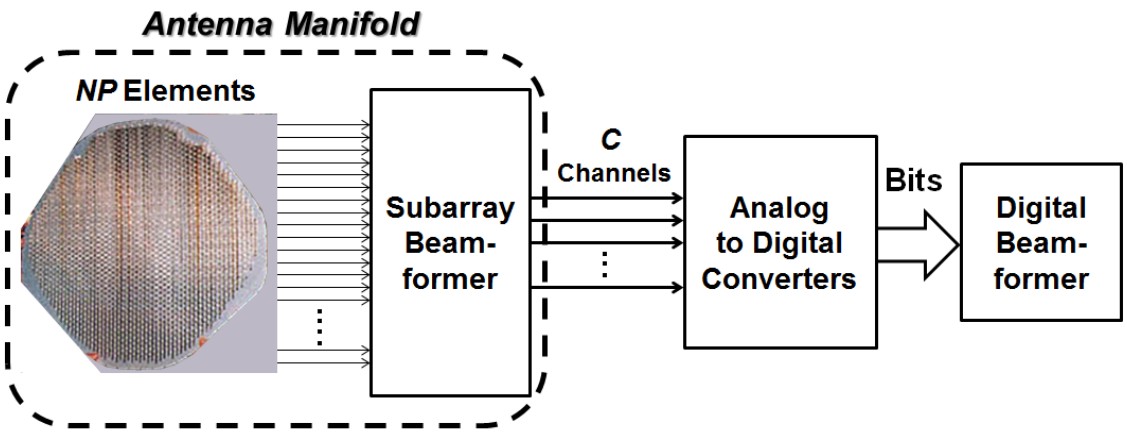

Figure 1. Notional system processing chain of a subarrayed antenna.

costs of increasing channel count is not limited to the material and manufacturing costs of more receive chains and ADCs, but also the burden of processing more digital data as well as the testing and calibration of more channels.

Even when systems have been equipped with a necessary number of channels, there are cases when such a system would greatly benefit from additional spatial DOF. When the subarrays of a phased array system have many elements compared to the number of digitized channels, there is unutilized potential DOF available via the subarray pattern. In order to steer the subarray pattern in the direction of interest, the subarray elements are equipped with the essential hardware (i.e. phase/time delays and attenuators) to create real directional nulls. However, without sampled data from the individual subarray elements, an adaptive weight set based on the interference statistics measured through the subarray manifold cannot be estimated. If one could discern what those weights should be, the subarrays could begin to leverage their spatial DOF to mitigate interference. This research will propose a method referred to asKnowledge-Aided Subarray Pattern Synthesis (KASPS)-Adaptive Digital Beamforming (ADBF) which will leverage the inherent DOF of the subarrays in conjunction with the digital DOF of the subarray channels in order to provide increased interference suppression.

Adaptive digital nulling is always preferable to creating nulls in a real beam pattern. Adaptive antenna patterns implemented in hardware always reduce the peak gain of the mainbeam (relative to the corresponding unadaptive, untapered pattern), resulting in a degraded signal response, whereas adaptive digital nulling preserves mainbeam gain. However, it will shown that there are situations where both adaptive digital nulling in conjunction with creating nulls in the real subarray beam pattern may provide superior performance over using adaptive digital nulling alone. For example, nulls in the subarray beam pattern would be implemented within the manifold prior to the ADCs and could reduce the dynamic range requirements of the receive chain, avoiding saturation and improving the effectiveness of adaptive digital nulling in the processor. Adaptive spatial nulling done in the subarrays could mitigate spatially isolated interference, thereby freeing up digital DOF for Space-Time Adaptive Processing (STAP).

1.1 Goals

The objective of this paper is to illustrate and explore a concept for increasing the spatial interference suppression (i.e., nulling) capabilities of a phased array radar by leveraging the inherent but dormant DOF of its analog subarrays. It will postulate a calibrated (i.e., known) phased array manifold design that when combined with knowledge-aided algorithms, and utilizing adaptive subarray patterns prior to the ADC, may be capable of effectively creating many more spatial nulls than what C channels would conventionally allow.

This research aspires to make three contributions to the field of EP for phased array systems. The first is to offer a proof of concept of the potential benefits of the KASPS-ADBF method. The second goal is to offer a concept of operations for the use of the KASPS-ADBF method. The final goal is to test the sensitivty of the

KASPS-ADBF method.

1.2 Approach

The technical approach of this research is to explore a concept for increasing a subarrayed phased array's spatial interference suppression capabilities by leveraging the inherent but dormant DOF of its subarrays. This research postulates a calibrated (i.e., known) phased array manifold that leverages knowledge-aided algorithms and subarray pattern synthesis to effectively null more interference signals than what adaptive digital processing alone would conventionally allow.

This research will extend the planar phased array system model most recently extended by Lt Col Phillip Corbell in [1]. It is hoped that the developments within this thesis may enable currently fielded phased arrays to improve performance in contested Radio Frequency (RF) environments through modest hardware and software upgrades. While this research is focused on a radar application, it is also applicable to any subarrayed phased array antenna used in a communication, navigation, or remote sensing application, and has the added benefit of being a receive-only (passive) technique.

1.3 Organization

The model originally put forth by J. Ward in [2] and extended in [3] is used as a foundation for this research. The essential elements and capabilities of the model are discussed in the literature review in Chapter II. Assumptions inherent in this research and related research endeavors are also detailed in the literature reveiw. Chapter III explains the methodology used in this research, including the KASPS technique, the trade offs of adapting the subarray pattern versus using digital adaptive processing, the Jammer Parameter Estimation (JPE) algorithm, and a discussion on parameter

sensitivity. Chapter IV presents the results from the techniques outlined in Chapter III, including an sensitivity analysis concerning jammer AOA misestimation, manifold error, and quantization. Chapter V draws conclusions from the results of the research and suggests future work that could be accomplished to further develop the techniques presented here.

II. Background

This research builds upon decades of research across numerous fields, including but not limited to adaptive arrays, Space-Time Adaptive Processing (STAP), and adaptive beamforming. This chapter surveys a selection of the published literature in these fields to provide context to the reader for the developments to follow. The system model used to conduct this research, which simulates a phased array utilizing non-overlapping subarrays is described. The limitations and assumptions inherent to the research are discussed. Finally, a selection of similar research efforts that complement the contributions here are reviewed.

2.1 System Model

The contents of this section describe the model of a digital phased array. In 1991, a team at the Hughes Aircraft Company released an article on STAP which evaluated techniques using an airborne two-dimensional (2-D) phased array side-looking radar model [4]. In 1994 J. Ward used a similar model in review of modern STAP techniques in his technical report titled "Space-time adaptive processing for airborne radar" [2]. This model was extended to account for planar arrays in 2002 by T. Hale [3]. The planar array model developed by T. Hale was extended to account for adaptive transmit patterns and subarrayed antenna architectures in 2006 by P. Corbell [1]. The simulation of adaptive subarray antenna patterns in conjunction with adaptive digital processing to increase interference suppression form the basis for the analysis of this thesis.

The radar model for this research considers an active electronically scanned planar phased array antenna. Figure 2 shows the geometry of the array, which exists in the x-z plane. There are N columns and P rows of elements, resulting in a total of

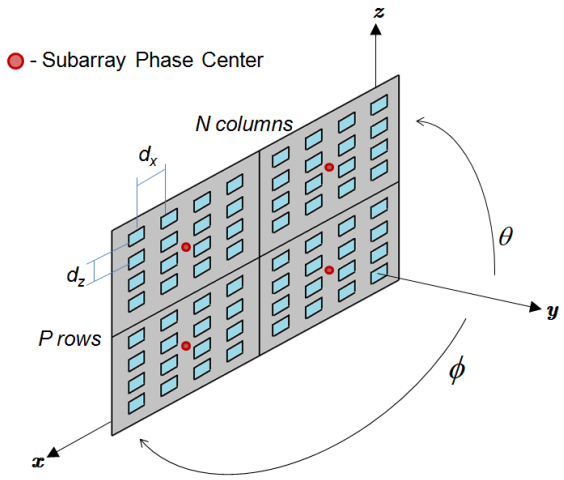

Figure 2. Notional planar phased array, adapted from [1].

NP elements. For an array that is uniformly spaced, distance d_x separates the N columns uniformly in the horizontal dimension, and distance d_z separates the P rows uniformly in the vertical dimension. Radar boresight points in the positive y-axis direction. The radar elevation angle, θ, is measured from the positive y-axis to the positive z-axis, indicating that negative elevations point toward the ground. The radar azimuth angle, ϕ, is measured from the positive y-axis towards the positive x-axis.

Central to this research effort is the accurate simulation of subarrays. The array face can be organized into subarrays in which the received signal from each element is weighed and summed with the received signals from all other elements in that subarray before going to an analog-to-digital converter (ADC) [5]. Each ADC constitutes an independent digitized channel. The radar only has as many digitized channels, C as it has subarrays (i.e., ADCs). The effects of subarraying have been simulated in the past as in [1,6–8]. This research follows the subarray model found in [1,7,8] in which a subarray pattern can be modeled as a programmable element pattern on an array for which the array factor is calculated from the phase centers of the subarrays.

This model defines N_{ch} columns of channels and P_{ch} rows of channels across the

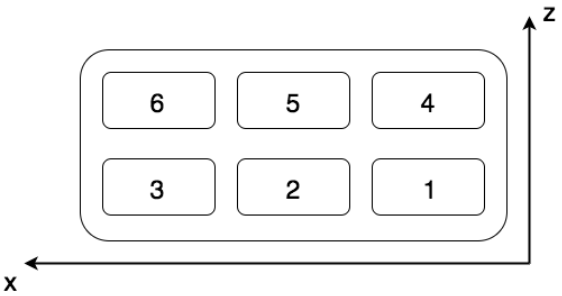

Figure 3. Notional planar phased array, with elements shown as indexed within the radar model. Proper indexing of elements is necessary to ensure phase consistency across the array face and the correct application of weights.

array face. Each channel is comprised of $N_{sub} \times P_{sub}$ elements. Non-overlapping subarrays of a rectangular array can be arranged into columns ($1 \times P_{sub}$), rows ($N_{sub} \times 1$), or rectangles ($N_{sub} \times P_{sub}$). The element locations within a given subarray are defined in the $3 \times N_{sub}P_{sub}$ matrix of element positions, $\mathbf{D}_{sub}$. The phase center locations of each subarray channel are defined in the $3 \times N_{ch}P_{ch}$ matrix of element positions, $\mathbf{D}_{ch}$. Of the $e = 1 \ldots N_{sub}P_{sub}$ elements comprising the subarray, the e^{th} element's position vector is the 3×1 vector $\mathbf{d}_e$. The matrix $\mathbf{D}_{sub}$ can either be dictated by the user, or generated to mimic any planar array geometry. A uniformly spaced subarray is used as an example, in which $N_{sub} = 3$, $P_{sub} = 2$, and $d_x = d_z$. This notional subarray geometry is shown in Figure 3, for which the corresponding matrix $\mathbf{D}_{sub}$ is

$$\mathbf{D}_{sub} = \begin{bmatrix} \mathbf{d}_1 & \mathbf{d}_2 & \mathbf{d}_3 & \mathbf{d}_4 & \mathbf{d}_5 & \mathbf{d}_6 \end{bmatrix} = \begin{bmatrix} 0 & d_x & 2d_x & 0 & d_x & 2d_x \\ 0 & 0 & 0 & 0 & 0 & 0 \\ 0 & 0 & 0 & d_z & d_z & d_z \end{bmatrix}. \tag{1}$$

The numbering of the columns of $\mathbf{D}_{sub}$ as related to the location of the elements on the subarray face, as organized into P_{sub} rows and N_{sub} columns, can be calculated

as

$$P_{row} = \left\lfloor \frac{n-1}{N_{sub}} \right\rfloor + 1,$$
$$N_{col} = ((n-1) \bmod N_{sub}) + 1, \tag{2}$$

in which $\lfloor \rfloor$ indicates rounding down to the nearest integer, and the mod operator results in the remainder after division of the term on the operators left by the term on the operators right. The matrix $\mathbf{D}_{ch}$ is made up of the position vectors describing the phase centers of each subarray. Assuming half wavelength element spacing and non-overlapping subarrays, the distance between subarray phase centers can be calculated as

$$d_{x,ch} = N_{sub}\frac{\lambda_0}{2}, \tag{3}$$
$$d_{z,ch} = P_{sub}\frac{\lambda_0}{2}. \tag{4}$$

The formulation and numbering convention of the $\mathbf{D}_{ch}$ matrix follows the same convention as the $\mathbf{D}_{sub}$ matrix. Thus, for the example provided to describe $\mathbf{D}_{sub}$ above (as in Equation (5)), the $\mathbf{D}_{ch}$ matrix would be defined as

$$\mathbf{D}_{ch} = \begin{bmatrix} \mathbf{d}_1 & \mathbf{d}_2 & \mathbf{d}_3 & \mathbf{d}_4 & \mathbf{d}_5 & \mathbf{d}_6 \end{bmatrix} = \begin{bmatrix} 0 & d_{x,ch} & 2d_{x,ch} & 0 & d_{x,ch} & 2d_{x,ch} \\ 0 & 0 & 0 & 0 & 0 & 0 \\ 0 & 0 & 0 & d_{z,ch} & d_{z,ch} & d_{z,ch} \end{bmatrix}. \tag{5}$$

Together, $\mathbf{D}_{ch}$ and $\mathbf{D}_{sub}$ describe the complete array geometry.

When N_{sub} and P_{sub} are both equal to 1, the $\mathbf{D}_{sub}$ matrix is only a single 3×1 element position vector. Under these conditions, each subarray consists of a single element, and the subarray phase center position vectors (stored in $\mathbf{D}_{ch}$) communicate the locations of each element. Such conditions describe an array with an ADC behind

every element.

2.1.1 Antenna Pattern.

The antenna pattern for the modeled antenna can be formed using a steering vector approach, as outlined in detail in Chapter III of [3] and summarized here. This model is valid for narrowband signals. The spatial frequencies of the antenna pattern in the x and z directions, ϑ_x and ϑ_z respectively, are defined as

$$\vartheta_x = \frac{d_x \cos\theta \sin\phi}{\lambda_0}, \tag{6}$$

$$\vartheta_z = \frac{d_z \sin\theta}{\lambda_0}, \tag{7}$$

where λ_0 is the wavelength of the center operating frequency of the radar and θ and ϕ are a single elevation and azimuth from the full raster of radar elevations and azimuths, $(\boldsymbol{\theta}, \boldsymbol{\phi})$. Azimuthal and elevation steering vectors are are used to formulate the array factors of both the digitized channels and the subarrays. The subarray azimuthal and elevation steering vectors are defined as

$$\mathbf{a}_{sub}(\vartheta_x) = \begin{bmatrix} 1 & e^{i2\pi\vartheta_x} & \dots & e^{i2\pi(N_{sub}-1)\vartheta_x} \end{bmatrix}^T, \tag{8}$$

$$\mathbf{e}_{sub}(\vartheta_z) = \begin{bmatrix} 1 & e^{i2\pi\vartheta_z} & \dots & e^{i2\pi(P_{sub}-1)\vartheta_z} \end{bmatrix}^T. \tag{9}$$

The channel azimuthal and elevation steering vectors are defined as

$$\mathbf{a}_{ch}(\vartheta_{x,ch}) = \begin{bmatrix} 1 & e^{i2\pi\vartheta_{x,ch}} & \dots & e^{i2\pi(N_{ch}-1)\vartheta_{x,ch}} \end{bmatrix}^T, \tag{10}$$

$$\mathbf{e}_{ch}(\vartheta_{z,ch}) = \begin{bmatrix} 1 & e^{i2\pi\vartheta_{z,ch}} & \dots & e^{i2\pi(P_{ch}-1)\vartheta_{z,ch}} \end{bmatrix}^T, \tag{11}$$

when $\vartheta_{x,ch}$ and $\vartheta_{z,ch}$ are calculated using the horizontal and vertical distances between subarray channel phase centers, $d_{x,ch}$ and $d_{z,ch}$ respectively.

The subarray factor, $W_{sub}(\theta,\phi)$ and the digital array factor $W_{ch}(\theta,\phi)$, are formed from the azimuthal and elevation steering vectors as given by

$$W_{sub}(\theta,\phi) = \left[\mathbf{e}_{sub}(\vartheta_z) \otimes \mathbf{a}_{sub}(\vartheta_x)\right]^T, \tag{12}$$

$$W_{ch}(\theta,\phi) = \left[\mathbf{e}_{ch}(\vartheta_{z,ch}) \otimes \mathbf{a}_{ch}(\vartheta_{x,ch})\right]^T. \tag{13}$$

The full antenna pattern is given by

$$G(\theta,\phi) = |W_{ch}(\theta,\phi)|^2 G_{sub}(\theta,\phi), \tag{14}$$

in which $G_{sub}(\theta,\phi)$ is the subarray pattern. The subarray pattern is expressed as

$$G_{sub}(\theta,\phi) = |W_{sub}(\theta,\phi)|^2 g(\theta,\phi), \tag{15}$$

in which $g(\theta,\phi)$ is the element power pattern (simply referred to as the element pattern). It should be noted that when N_{sub} and P_{sub} are both equal to 1, the subarray pattern becomes equivalent to the element pattern. The element pattern is formulated from the element voltage pattern, $f(\theta,\phi)$, as

$$g(\theta,\phi) = |f(\theta,\phi)|^2. \tag{16}$$

The voltage element pattern used in prior models [1–4] utilized a cosine pattern in elevation and azimuth, with a element gain, g_e, and backlobe attenuation factor, b_e, where

$$f(\theta,\phi) = \begin{cases} g_e \cos\theta\cos\phi, & -90^o \geq \phi, \theta \geq 90^o \\ b_e g_e \cos\theta\cos\phi, & 90^o \geq \phi, \theta \geq 270^o. \end{cases} \tag{17}$$

The cosine element pattern experiences steep gain losses for look directions off of

boresight. As this research focuses on radar applications for which wide look angles are desirable, this research models a microstrip radiating element pattern which provides a flatter response across look angles [9]. The microstrip radiating element is more representative of element patterns found in modern radars. The element pattern of the microstrip radiating element is defined as

$$f(\theta,\phi) = \begin{cases} g_e \frac{\sin(S\sin\theta)}{2\sin\left(\frac{S}{2}\sin\theta\right)} \frac{\sin(S\sin\phi)}{2\sin\left(\frac{S}{2}\sin\phi\right)}, & -90^o \geq \phi, \theta \geq 90^o \\ b_e g_e \frac{\sin(S\sin\theta)}{2\sin\left(\frac{S}{2}\sin\theta\right)} \frac{\sin(S\sin\phi)}{2\sin\left(\frac{S}{2}\sin\phi\right)}, & 90^o \geq \phi, \theta \geq 270^o, \end{cases} \tag{18}$$

in which S is the spacing between two slots within the microstrip in electrical degrees. Manipulation of S allows the element designer to widen or narrow the element beamwidth as necessary. Throughout this research S is set to correspond to a 2 dB drop in gain when steered 60^o off boresight.

When the spacing between elements is greater than $\frac{\lambda_0}{2}$, as is clearly satisfied for the array factor $\mathbf{W}_{ch}$ when N_{sub} and P_{sub} are greater than 1, multiple maxima of equal magnitude are formed in the pattern [10]. While the principal maxima in the look direction of interest is referred to as the mainbeam, the other maxima are referred to as grating lobes. The locations of the grating lobes, (θ_{GL}, ϕ_{GL}), can be predicted by

$$\begin{aligned} \theta_{GL} &= \sin^{-1}\left(\sin(\theta_0) \pm \frac{l\lambda_0}{d_{z,ch}}\right), \\ \phi_{GL} &= \sin^{-1}\left(\frac{\cos(\theta_0)\sin(\phi_0) \pm \frac{m\lambda_0}{d_{x,ch}}}{\cos\left(\sin^{-1}\left(\sin(\theta_0) \pm \frac{l\lambda_0}{d_{z,ch}}\right)\right)}\right), \end{aligned} \tag{19}$$

for which $l = 0, 1, 2, \ldots$, $m = 0, 1, 2, \ldots$, and (θ_0, ϕ_0) is the desired look direction [10]. Letting $l = m = 0$ in the Equations in (19) results in the location of the mainbeam. In order for a given l and m combination to yield a real grating lobe in the pattern,

the following condition must be met [5]

$$\left(\cos(\theta_0)\sin(\phi_0) \pm \frac{m\lambda_0}{d_{x,ch}}\right)^2 + \left(\sin(\theta_0) \pm \frac{l\lambda_0}{d_{z,ch}}\right)^2 < 1. \tag{20}$$

The locations of the grating lobes in the digital array factor, $\mathbf{W}_{ch}$, are significant as they can cause ambiguous perceived returns throughout the radar's field of view.

While the development to this point is useful for calculating beam patterns of antennas whose element positions adhere to strictly uniform spacing, a more flexible development will allow for calculation of antenna patterns of arrays with non-uniform element placements. For antenna patterns utilizing a non-uniform element layout, [11] derives the array beam pattern by formulating the array factors as

$$W_{sub}(\theta,\phi) = \left[e^{\frac{i2\pi}{\lambda_0}\hat{\mathbf{k}}(\theta,\phi)\mathbf{D}_{sub}}\right]^T, \tag{21}$$

$$W_{ch}(\theta,\phi) = \left[e^{\frac{i2\pi}{\lambda_0}\hat{\mathbf{k}}(\theta,\phi)\mathbf{D}_{ch}}\right]^T, \tag{22}$$

in which $\hat{\mathbf{k}}(\theta,\phi)$ is the 1×3 pointing vector of unit length. The pointing vector $\hat{\mathbf{k}}(\theta,\phi)$ is expressed as

$$\hat{\mathbf{k}}(\theta,\phi) = \left[\cos(\theta)\sin(\phi), \quad \cos(\theta)\cos(\phi), \quad \sin(\theta)\right]. \tag{23}$$

When the elements are uniformly spaced, the steering vector and arbitrary element placement approach yield equivalent antenna patterns. This equivalence can be understood by observing that

$$e^{\frac{i2\pi}{\lambda_0}\hat{\mathbf{k}}(\theta,\phi)\mathbf{D}_{sub}} = \mathbf{e}_{sub}(\vartheta_z) \otimes \mathbf{a}_{sub}(\vartheta_x), \tag{24}$$

$$e^{\frac{i2\pi}{\lambda_0}\hat{\mathbf{k}}(\theta,\phi)\mathbf{D}_{ch}} = \mathbf{e}_{ch}(\vartheta_{z,ch}) \otimes \mathbf{a}_{ch}(\vartheta_{x,ch}). \tag{25}$$

2.1.2 Noise Model.

The noise model in this research follows the development in [12]. Summarized here, greater detail can also be referenced in Chapter 2 of [2] or Chapter 3 of [3].

The noise in this research is simulated as complex white Gaussian noise of power σ^2, with independent realizations at each element of the array. The assumption of white noise remains valid as long as the Pulse Repetition Frequency (PRF) of the radar is significantly less than the instantaneous bandwidth of the radar waveform [2]. The $N_{sub}P_{sub} \times 1$ single spatial noise snapshot, $\boldsymbol{\chi}_{n,sub}$, is represented as

$$\chi_{n,sub} \sim \mathcal{N}\left(0, \frac{\sigma^2}{2}\right) + i\mathcal{N}\left(0, \frac{\sigma^2}{2}\right), \tag{26}$$

$$\boldsymbol{\chi}_{n,sub} = \left[\chi_{n,sub,1} \quad \cdots \quad \chi_{n,sub,N_{sub}P_{sub}}\right]^T. \tag{27}$$

The $N_{sub}P_{sub} \times N_{sub}P_{sub}$ clairvoyant covariance matrix, $\mathbf{R}_{n,sub}$, is

$$\mathbf{R}_{n,sub} = \mathbb{E}\left\{\boldsymbol{\chi}_{n,sub}\boldsymbol{\chi}_{n,sub}^H\right\} = \sigma^2\mathbf{I}_{MN_{sub}P_{sub}}. \tag{28}$$

The noise values behind each element will change over the duration of time that training data is being collected. The number of training data samples, t, necessary to estimate a full covariance matrix is established by the Reed, Mallett and Brennan Rule from [13]. The Reed, Mallet and Brennan Rule sets the minimum amount of training data, t, necessary to estimate a covariance matrix equal to twice the number of adaptive weights to be calculated. For a fully adaptive array with an ADC behind each element, Reed, Mallet and Brennans rule requires at least $t = 2NP$ samples of support.

The $N_{sub}P_{sub} \times t$ matrix of spatial noise snapshots, $\mathbf{X}_{n,sub}$, is built through con-

catenating t realizations of the single spatial noise snapshot $\boldsymbol{\chi}_{n,sub}$, as

$$\mathbf{X}_{n,sub} = \left[\boldsymbol{\chi}_{n,sub,1} \quad \dots \quad \boldsymbol{\chi}_{n,sub,t}\right]. \tag{29}$$

With the full set of noise snapshots, $\mathbf{X}_{n,sub}$, collected, it is now possible to estimate the covariance matrix, $\hat{\mathbf{R}}_{n,sub}$, by averaging over the outer product of all t spatial snapshots, $\mathbf{X}_{n,sub}$, as

$$\hat{\mathbf{R}}_{n,sub} = \frac{1}{t}\left[\mathbf{X}_{n,sub}\mathbf{X}_{n,sub}^{H}\right]. \tag{30}$$

There will be deviations in the values of $\hat{\mathbf{R}}_{n,sub}$ from their true values in $\mathbf{R}_{n,sub}$, as infinite realizations of training data would be required to perfectly estimate the covariance matrix and only t are collected.

To represent the noise as it is summed in the digitized channels, the $N_{ch}P_{ch} \times 1$ single noise spatial snapshot $\boldsymbol{\chi}_{n,ch}$, is given by

$$\chi_{n,ch} \sim \mathcal{N}\left(0, \frac{N_{sub}P_{sub}\sigma^2}{2}\right) + i\mathcal{N}\left(0, \frac{N_{sub}P_{sub}\sigma^2}{2}\right), \tag{31}$$

$$\boldsymbol{\chi}_{n,ch} = \left[\chi_{n,ch,1} \quad \dots \quad \chi_{n,ch,N_{ch}P_{ch}}\right]^{T}. \tag{32}$$

Note that under the subarrayed model in which there is not an ADC behind each element, the necessary amount of sample support, t, for estimating the covariance matrix [13] has decreased based on the dimensionality of the channels ($t = N_{ch}P_{ch}$). The $N_{ch}P_{ch} \times N_{ch}P_{ch}$ clairvoyant noise covariance matrix as formed through the digitized channels of the antenna, $\mathbf{R}_{n,ch}$ is defined as

$$\mathbf{R}_{n,ch} = \mathbb{E}\left\{\boldsymbol{\chi}_{n,ch}\boldsymbol{\chi}_{n,ch}^{H}\right\} = \sigma^2 N_{sub}P_{sub}\mathbf{I}_{N_{ch}P_{ch}}, \tag{33}$$

where the N_{sub} and P_{sub} terms increase the power of the noise linearly based on the number of elements over which the noise is being summed in each channel [1]. The

$N_{ch}P_{ch} \times t$ collection of spatial noise snapshots, $\mathbf{X}_{n,ch}$ is built through concatenating t realizations of the single spatial noise snapshot $\boldsymbol{\chi}_{n,ch}$, as

$$\mathbf{X}_{n,ch} = [\boldsymbol{\chi}_{n,ch,1} \quad \dots \quad \boldsymbol{\chi}_{n,ch,t}]. \tag{34}$$

The estimated covariance matrix, $\hat{\mathbf{R}}_{n,ch}$, is given by

$$\hat{\mathbf{R}}_{n,ch} = \frac{1}{t}\left[\mathbf{X}_{n,ch}\mathbf{X}_{n,ch}^{H}\right]. \tag{35}$$

2.1.3 Jamming Model.

The interference sources simulated in this research are modeled after barrage noise jammers. According to United States Federal Standard 1037c [14], barrage jamming "is accomplished by transmitting a band of frequencies that is large with respect to the bandwidth of a single emitter." The jammers in this research model are simulated by complex white Gaussian noise in the far field. The jammer quantity (J), effective radiated power spectral density (S_j), range (R_j), and location in elevation and azimuth (θ_j,ϕ_j) are determined by the scenario. In a scenario with J jammers, the jammers number $b = 1 \dots J$. Thus, the radiated power spectral density of the b^{th} jammer is $S_{j,b}$, the range of the b^{th} jammer is $R_{j,b}$, and the elevation and azimuth of the b^{th} jammer are $(\theta_{j,b}, \phi_{j,b})$. The power of the b^{th} jammer, $P_{j,sub,b}$, for a single subarray as incident through the element pattern is given by

$$P_{j,sub,b} = \frac{S_{j,b} g\left(\theta_{j,b}, \phi_{j,b}\right) \lambda_0^2}{\left(4\pi\right)^2 R_{j,b}^2 L_s}. \tag{36}$$

The output of the b^{th} jammer as received at the subarray face at a single instance,

$\alpha_{j,sub,b}$, is drawn as a complex white Gaussian noise sample as

$$\alpha_{j,sub,b} \sim \mathcal{N}\left(0, \frac{P_{j,sub,b}}{2}\right) + i\mathcal{N}\left(0, \frac{P_{j,sub,b}}{2}\right). \tag{37}$$

The $N_{sub}P_{sub} \times 1$ spatial snapshot from the b^{th} jammer, $\boldsymbol{\chi}_{j,sub,b}$, represents the jamming value $\alpha_{j,sub,b}$ as received by each of the $N_{sub}P_{sub}$ subarray elements

$$\boldsymbol{\chi}_{j,sub,b} = \left[\mathbf{e}_{sub}\left(\vartheta_{z,sub,b}\right) \otimes \mathbf{a}_{sub}\left(\vartheta_{x,sub,b}\right)\right] \alpha_{j,sub,b}. \tag{38}$$

For non-uniform element locations, the spatial snapshot of the b^{th} jammer can be calculated as

$$\boldsymbol{\chi}_{j,sub,b} = \alpha_{j,sub,b}\left[e^{\frac{i2\pi}{\lambda_0}\hat{\mathbf{k}}\left(\theta_{j,b},\phi_{j,b}\right)\mathbf{D}_{sub}}\right]^T. \tag{39}$$

The $N_{sub}P_{sub} \times 1$ spatial snapshot from all J jammers in the scenario, $\boldsymbol{\chi}_{j,sub}$, is formed by adding all of the individual snapshots

$$\boldsymbol{\chi}_{j,sub} = \boldsymbol{\chi}_{j,sub,1} + \cdots + \boldsymbol{\chi}_{j,sub,b} + \cdots + \boldsymbol{\chi}_{j,sub,J}. \tag{40}$$

The clairvoyant jamming covariance matrix of a lone subarray, $\mathbf{R}_{j,sub}$, is

$$\mathbf{R}_{j,sub} = \mathbb{E}\left\{\boldsymbol{\chi}_{j,sub}\boldsymbol{\chi}_{j,sub}^H\right\}, \tag{41}$$

$$\mathbf{R}_{j,sub} = \sum_{b=1}^{J} P_{j,sub,b}\left(\theta_{j,b},\phi_{j,b}\right)\left[e^{\frac{i2\pi}{\lambda_0}\hat{\mathbf{k}}\left(\theta_{j,b},\phi_{j,b}\right)\mathbf{D}_{sub}}\right]^H\left[e^{\frac{i2\pi}{\lambda_0}\hat{\mathbf{k}}\left(\theta_{j,b},\phi_{j,b}\right)\mathbf{D}_{sub}}\right]. \tag{42}$$

The $1 \times t$ vector of jammer amplitudes, $\boldsymbol{\alpha}_{j,sub,b}$, received by the subarray from the b^{th} jammer provide the necessary set of observations to constitute a full set of training data [13]. The jammer amplitudes are modeled as complex white Gaussian

noise, and consist of samples of $\alpha_{j,sub,b}$ as

$$\boldsymbol{\alpha}_{j,sub,b} = \left[\alpha_{j,sub,b,1} \quad \dots \quad \alpha_{j,sub,b,t}\right]. \tag{43}$$

Considering the b^{th} jammer in the scene, the $N_{sub}P_{sub} \times t$ space time jammer snapshot of the subarray, $\mathbf{X}_{j,sub,b}$, is given by

$$\mathbf{X}_{j,sub,b} = \left[\mathbf{e}_{sub}\left(\vartheta_{z,b}\right) \otimes \mathbf{a}_{sub}\left(\vartheta_{x,b}\right)\right] \boldsymbol{\alpha}_{j,sub,b}, \tag{44}$$

or in the case of non-uniform element spacing via

$$\mathbf{X}_{j,sub,b} = \left[e^{\frac{i2\pi}{\lambda_0}\hat{\mathbf{k}}\left(\theta_{j,b},\phi_{j,b}\right)\mathbf{D}_{sub}}\right]^T \boldsymbol{\alpha}_{j,sub,b}. \tag{45}$$

The collection of spatial snapshots from all jammers in the scene, $\mathbf{X}_{j,sub}$, is created by summing the spatial snapshots of all of the individual J jammers

$$\mathbf{X}_{j,sub} = \mathbf{X}_{j,sub,1} + \cdots + \mathbf{X}_{j,sub,b} + \cdots + \mathbf{X}_{j,sub,J}. \tag{46}$$

The estimated jammer covariance matrix is then formed from the outer product of the jammer space time snapshot, as

$$\hat{\mathbf{R}}_{j,sub} = \frac{1}{t}\left[\mathbf{X}_{j,sub}\mathbf{X}_{j,sub}^H\right] \tag{47}$$

in the case that

$$\mathbb{E}\left\{\boldsymbol{\alpha}_{j,sub,b}\,\boldsymbol{\alpha}_{j,sub,f}\right\} = 0, \quad \forall \quad b \neq f. \tag{48}$$

The power of the b^{th} jammer incident upon the antenna as received through the

subarray pattern, $P_{j,ch,b}\left(\theta_{j,b},\phi_{j,b}\right)$, is given by

$$P_{j,ch,b}=\frac{S_{j,b}G_{sub}\left(\theta_{j,b},\phi_{j,b}\right)\lambda_0^2}{\left(4\pi\right)^2R_{j,b}^2L_s}. \tag{49}$$

The output of the b^{th} jammer as received at the array face at a single instance, $\alpha_{j,ch,b}$, is drawn as a complex white Gaussian noise sample as

$$\alpha_{j,ch,b}\sim\mathcal{N}\left(0,\frac{P_{j,ch,b}}{2}\right)+i\mathcal{N}\left(0,\frac{P_{j,ch,b}}{2}\right). \tag{50}$$

The $N_{ch}P_{ch}\times1$ spatial snapshot from the b^{th} jammer represents the jamming value $\alpha_{j,ch,b}$ as received by each of the $N_{ch}P_{ch}$ array channels

$$\boldsymbol{\chi}_{j,ch,b}=\left[\mathbf{e}_{ch}\left(\vartheta_{z,ch,b}\right)\otimes\mathbf{a}_{ch}\left(\vartheta_{x,ch,b}\right)\right]\alpha_{j,ch,b}. \tag{51}$$

For non-uniform element locations, the spatial snapshot of the b^{th} jammer can be calculated as

$$\boldsymbol{\chi}_{j,ch,b}=\alpha_{j,ch,b}\left[e^{\frac{i2\pi}{\lambda_0}\hat{\mathbf{k}}\left(\theta_{j,b},\phi_{j,b}\right)\mathbf{D}_{ch}}\right]^T. \tag{52}$$

The $N_{ch}P_{ch}\times1$ spatial snapshot from all J jammers in the scenario, $\boldsymbol{\chi}_{j,ch}$, is formed by adding all of the individual snapshots

$$\boldsymbol{\chi}_{j,ch}=\boldsymbol{\chi}_{j,ch,1}+\cdots+\boldsymbol{\chi}_{j,ch,b}+\cdots+\boldsymbol{\chi}_{j,ch,J}. \tag{53}$$

The clairvoyant jammer covariance matrix as seen through the digitized channels, $\mathbf{R}_{j,ch}$, will be of $N_{ch}P_{ch}\times N_{ch}P_{ch}$ dimensionality and is equivalent to the expectation of the outer product of the collection of spatial jammer snapshots as formed through

the digitized channels, $\mathbf{X}_{j,ch}$, as given by

$$\mathbf{R}_{j,ch} = \mathbb{E}\left\{\boldsymbol{\chi}_{j,ch}\boldsymbol{\chi}_{j,ch}^{H}\right\}, \tag{54}$$

$$\mathbf{R}_{j,ch} = \sum_{b=1}^{J} P_{j,ch,b}\left(\theta_{j,b},\phi_{j,b}\right)\left[e^{\frac{i2\pi}{\lambda_0}\hat{\mathbf{k}}\left(\theta_{j,b},\phi_{j,b}\right)\mathbf{D}_{ch}}\right]^{H}\left[e^{\frac{i2\pi}{\lambda_0}\hat{\mathbf{k}}\left(\theta_{j,b},\phi_{j,b}\right)\mathbf{D}_{ch}}\right]. \tag{55}$$

The $1 \times t$ vector of jammer amplitudes received through the digitized channels from the b^{th} jammer, $\boldsymbol{\alpha}_{j,ch,b}$, provides the necessary set of observations to constitute a full set of training data [13]. The jammer amplitudes are modeled as complex white Gaussian noise, and consist of samples of $\alpha_{j,ch,b}$ as

$$\boldsymbol{\alpha}_{j,ch,b} = \left[\alpha_{j,ch,b,1} \quad \ldots \quad \alpha_{j,ch,b,t}\right]. \tag{56}$$

The $N_{ch}P_{ch} \times t$ collection of spatial jammer snapshots from the b^{th} jammer, $\mathbf{X}_{j,ch,b}$, is calculated using $\boldsymbol{\alpha}_{j,ch,b}$ as

$$\mathbf{X}_{j,ch,b} = \left[\mathbf{e}_{ch}\left(\vartheta_{z,ch,b}\right) \otimes \mathbf{a}_{ch}\left(\vartheta_{x,ch,b}\right)\right]\boldsymbol{\alpha}_{j,ch,b}, \tag{57}$$

or in the case of non-uniform element locations via

$$\mathbf{X}_{j,ch,b} = \left[e^{\frac{i2\pi}{\lambda_0}\hat{\mathbf{k}}\left(\theta_{j,b},\phi_{j,b}\right)\mathbf{D}_{ch}}\right]^{T}\boldsymbol{\alpha}_{j,ch,b}. \tag{58}$$

The spatial snapshot of all jammers in the scene, $\mathbf{X}_{j,ch}$, is created by summing the spatial snapshots of all of the individual J jammers

$$\mathbf{X}_{j,ch} = \mathbf{X}_{j,ch,1} + \cdots + \mathbf{X}_{j,ch,b} + \cdots + \mathbf{X}_{j,ch,J}. \tag{59}$$

The estimated jammer covariance matrix is calculated by taking the outer product

of the collection of spatial jammer snapshots, as

$$\hat{\mathbf{R}}_{j,ch} = \frac{1}{t}\left[\mathbf{X}_{j,ch}\mathbf{X}_{j,ch}^{H}\right], \tag{60}$$

in the case that

$$\mathbb{E}\left\{\boldsymbol{\alpha}_{j,ch,b}\,\boldsymbol{\alpha}_{j,ch,f}\right\} = 0, \quad \forall \quad b \neq f. \tag{61}$$

The full collection of spatial snapshots which encompass both the noise and jammer components is found by summing the snapshots from each model, as shown, whether from the single subarray or channel perspective

$$\mathbf{X}_{sub} = \mathbf{X}_{n,sub} + \mathbf{X}_{j,sub}, \tag{62}$$

$$\mathbf{X}_{ch} = \mathbf{X}_{n,ch} + \mathbf{X}_{j,ch}. \tag{63}$$

The same relationship holds for clairvoyant and estimated covariance matrices for the single subarray and channel perspectives

$$\mathbf{R}_{sub} = \mathbf{R}_{n,sub} + \mathbf{R}_{j,sub}, \tag{64}$$

$$\hat{\mathbf{R}}_{sub} = \hat{\mathbf{R}}_{n,sub} + \hat{\mathbf{R}}_{j,sub}, \tag{65}$$

$$\mathbf{R}_{ch} = \mathbf{R}_{n,ch} + \mathbf{R}_{j,ch}, \tag{66}$$

$$\hat{\mathbf{R}}_{ch} = \hat{\mathbf{R}}_{n,ch} + \hat{\mathbf{R}}_{j,ch}. \tag{67}$$

2.2 Model Limitations and Assumptions

The airborne radar model used in this research is constrained by a number of assumptions and limitations, which were deemed to be outside the scope of the research objective. Many of these limitations and assumptions, as they pertain to the modeling of subarrays and other factors, are documented here.

2.2.1 Limitations of Subarrayed Model.

Phased array antennas may utilize a subarray architecture for a variety of reasons. It may be because the expense of an ADC behind each element is too costly, or the data handling and processing burdens would be too great. Subarrays also enable the ability to use a single array for multiple functions simultaneously, including radar, communications, electronic warfare, etc.

By assuming the array elements utilize half-wavelength spacing, grating lobes in the total antenna pattern, $\mathbf{G}$, are avoided. However, in synthesizing an array factor, $\mathbf{W}_{pc}$ (Equation (13)), from the phase centers of the C non-overlapping subbarrays the half-wavelength distance is exceeded and grating lobes can be observed. In practice, the array factor is multiplied by the subarray pattern, $\mathbf{G}_{sub}$ (Equation (15)), resulting in the original antenna pattern $\mathbf{G}$ (Equation (14)) [15].

Under narrowband conditions and using the element spacing described above, the nulls of $\mathbf{G}_{sub}$ align with the grating lobes of $\mathbf{W}_{pc}$, and cancel the grating lobes. However, as soon as the frequency of the incident signal starts deviating from the narrowband, the nulls of $\mathbf{G}_{sub}$ can become disaligned with the grating lobes of $\mathbf{W}_{pc}$, causing grating lobes in the resultant antenna pattern $\mathbf{G}$. This research does not consider frequencies other than those matched to the half-wavelength element spacing of the central operating frequency, λ_0. However, misalignment of $\mathbf{G}_{sub}$ and $\mathbf{W}_{pc}$ can also occur from machining errors in the aperture [16], or errors in the manifold calibration. Additionally, to have perfect knowledge of an array manifold requires constant recalibration [17] which is typically not practical in an operating environment. Grating lobes arising from aperture errors or in the subarray architecture or manifold calibration errors are not examined in this research.

When phase shifters behind each element are used to steer the beam, deviations from the narrowband can result in an effect referred to as "phase squint" [5]. The

instantaneous employable bandwidth of the array (in percent) is roughly equal to the beamwidth of the subarray (in degrees) [18]. "Phase squint" can cause a shift in the subarray factor to the point where the nulls become misaligned and fail to suppress the array pattern grating lobes. This research does not consider frequencies other than those matched to the half-wavelength element spacing, and so the effects of "phase squint" are not examined. Arrays that use time delays as a means of phase manipulation are not susceptible to "phase squint."

A common practice in antennas utilizing subarrayed architectures is to overlap the subarrays in order to achieve better sidelobe performance [19], [20]. Overlapping refers to a technique in which the return from a single element may contribute to two or more different subarray channels. Using an overlapping subarray architecture changes the shape of the subarray pattern, $\mathbf{G}_{sub}$. Thus, overlapping subarrays can be designed to suppress the grating lobes of the array factor, $\mathbf{W}_{pc}$, for frequencies outside of the center operating frequency of the array. Overlapping subarrays can be used to counteract the effects of "phase squint," or grating lobes arising from aperture errors or manifold calibration errors. The technique of overlapping subarrays is not modeled in this research.

Other random sources of array error are not accounted for. For instance, the effects of random phase and amplitude errors when setting adaptive weights are not considered. Thus the increased sidelobe levels, pointing errors, and directivity decreases that stem from such error [5] are unexamined. Methods of accounting for and minimizing such errors for different subarray construction methods are analyzed in [15]. (The effects of phase and amplitude quantization, however, and the resulting "quantization lobes," are accounted for in the radar model and explored in this research in Section 4.3.3).

This research makes the assumption that every element of the array has an iden-

tical element pattern, shown in Equation (16), which fails to account for the effect of mutual coupling. In practice, centrally located elements of an array will have similar element patterns, while element patterns from the array edges will be asymmetrical [5]. This will have an effect on the mainbeam and sidelobe gain levels of the antenna pattern. With control over the source voltage to each element, and a knowledge of each element's pattern in the presence of mutual coupling, low-sidelobe patterns can be synthesized. The practice is not dissimilar in nature to array tapering, in which different windows can be applied to phase weights to improve sidelobe performance. Many such windows and their performance are examined in [21]. However, no array tapering techniques are examined in this research.

Finally, little consideration was given to the optimality of the chosen subarray configurations of the proceeding scenarios, which can be graded on a number of factors (such as sidelobe level after adaptation, conduciveness to super resolution techniques, suitability for difference beamforming, etc). The optimality of subarray configurations is considered in depth in [22].

2.2.2 Other Limitations and Assumptions.

The airborne radar model used in this research does rely on various other assumptions unrelated to the subarray simulation. For instance, Doppler tolerance is assumed for all transmitted waveforms. This simplifies the time frequency autocorrelation function to 1. This model does not account for aircraft flying at a crab angle, thus the Doppler shift of a return at boresight (y-positive axis to the radar) is always equal to 0. This model also discounts the effects of sky clutter, as they are assumed negligible compared to the effects of the ground clutter, interference, and noise signals.

The model presented does not include modeling of clutter. Inclusion of a clutter

model would not only allow for analysis on the real versus digital adaptation tradeoffs on ground clutter, but would introduce a Doppler dependence on what is presented here as a spatial analysis.

In the realm of interference suppression, techniques must sometimes be used to prevent adapting the array weights from repressing target returns in the mainbeam [23]. In the past, target returns were generally much weaker than sidelobe jamming signals, and limited degrees of freedom (DOF) constrained the ability to place nulls. In modern radars that place more power on the target and have more DOF, care must be taken that the target return is not adaptively nulled. Different time domain, frequency domain, and angle domain techniques, such as those examined in [23] seek to prevent target nulling in the mainbeam. The techniques presented herein have similarities to the "sample-and-hold" method presented in [23], but in general such techniques are not considered in this research.

This model does not account for multi-path reflections of jamming signals off of aircraft surfaces. Such reflections can decorrelate the jamming signal, and require the placement of widened nulls [24]. In order to reduce the null width, multipath techniques and rapid adaptation of element weights are required. Reflections of jamming signals off aircraft surfaces and the methods to account for them are not considered in this research.

Finally, the techniques herein do not consider phase-only weighting algorithms. While amplitude-phase weights are required for an optimal weighting solution [25], some manifolds may only provide phase weighting capability. In this case a unique solution to the weighting vector does not exist. Many algorithmic techniques have been developed to calculate the optimum set of phase-only weights, such as in [26,27]

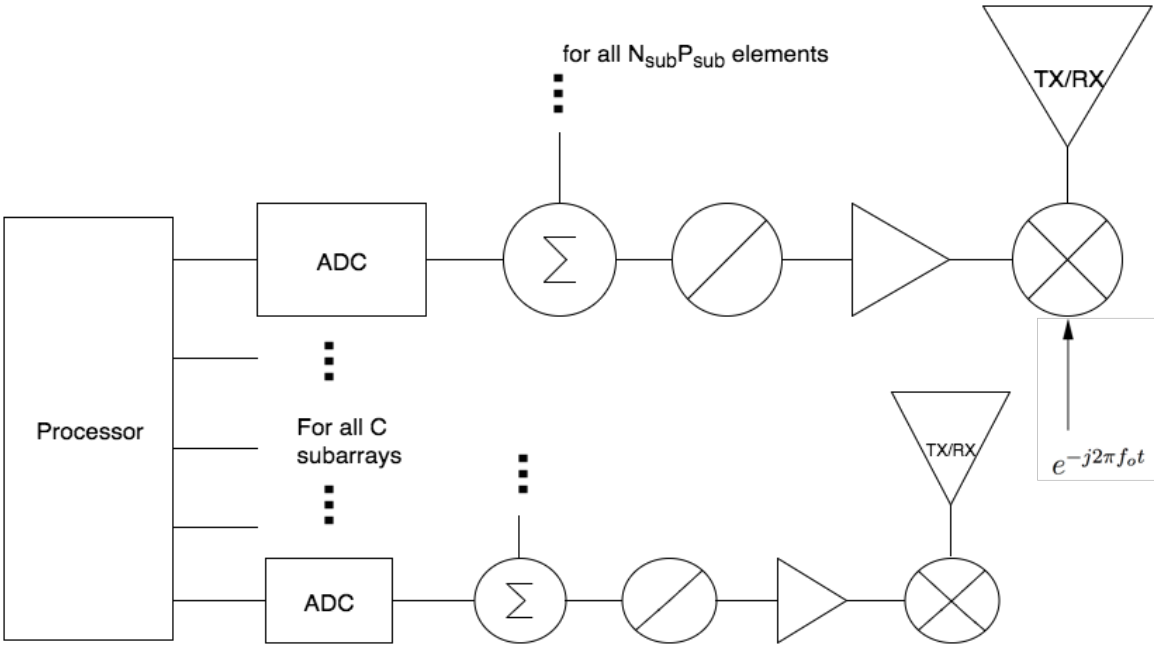

Figure 4. Modeled receive/transmit chain, consisting of a microstrip radiating antenna element followed by a mixdown stage, and an attenuator and phase shifter which allow individual weights to be placed on each element. The elements sum into a single ADC for each subarray.

2.3 Spatial Filtering

The model described in Section 2.1 will be used to evaluate the performance of different spatial filters in suppressing spatially localised interference. The antenna pattern defined by Equation (14) constitutes a spatial filter. The pattern can be steered or adapted using weights. The application of different weights constitute unique spatial filters. The mechanisms to calculate different spatial filters, and the metrics used to evaluate them are described in this section. Figure 4 shows the receive chain for the radar model in which the manifold connecting the antenna and radar processor is assumed to be known and calibrated unless otherwise stated. The figure depicts the phase shifter and attenuator hardware via which the subarray weights are implemented and the radar processor in which the digital channel weights are applied.

2.3.1 Non-Adaptive Spatial Filter.

In order to steer the antenna pattern for maximum gain in the desired look direction, (θ_0, ϕ_0), both the digital array factor and subarray factor are steered toward that direction. As such, both a set of weights to be applied digitally to the channels, $\mathbf{w}_{ch}$, and a set of weights to be applied in hardware behind the subarray elements, $\mathbf{w}_{sub}$, must be calculated. Steering weights are calculated from the antenna geometry.

When considering the set of digital steering weights, a steering vector $\mathbf{v}_{ch}(\theta, \phi)$ of length $N_{ch}P_{ch}$ for a single (θ_0, ϕ_0) look angle is represented mathematically as

$$\mathbf{v}_{ch}(\theta_0, \phi_0) = \mathbf{e}_{ch}\left(\vartheta_{z,ch,0}\right) \otimes \mathbf{a}_{ch}\left(\vartheta_{x,ch,0}\right), \tag{68}$$

or when using non-uniform elements, as:

$$\mathbf{v}_{ch}(\theta_0, \phi_0) = e^{\frac{i2\pi}{\lambda_0}\hat{\mathbf{k}}(\theta_0,\phi_0)\mathbf{D}_{ch}}, \tag{69}$$

where each of the $N_{ch}P_{ch}$ values correspond to a channel of the array.

When considering the set of weights to be applied in hardware behind the subarray elements, a steering vector $\mathbf{v}_{sub}(\theta_0, \phi_0)$ of length $N_{sub}P_{sub}$ for a single (θ_0, ϕ_0) look angle is represented mathematically as

$$\mathbf{v}_{sub}\left(\theta_0, \phi_0\right) = \mathbf{e}_{sub}\left(\vartheta_{z,0}\right) \otimes \mathbf{a}_{sub}\left(\vartheta_{x,0}\right), \tag{70}$$

or when using non-uniform elements, as

$$\mathbf{v}_{sub}\left(\theta_0, \phi_0\right) = e^{\frac{i2\pi}{\lambda_0}\hat{\mathbf{k}}\mathbf{D}_{sub}}, \tag{71}$$

where each of the $N_{sub}P_{sub}$ values correspond to an element of the subarray. It is

important to have accurate knowledge of the array manifold (as stored in $\mathbf{D}_{ch}$ and $\mathbf{D}_{sub}$) so that the steering vector is accurately matched to the array. If the manifold is not well known the steering vector will be mismatched to the array. Steering vector mismatch will lead to suboptimal target signal power output through the spatial filter [28].

These steering vectors are equivalent to the weight vectors that will steer the digital array factor and subarray factor to the given look direction, yielding

$$\mathbf{w}_{ch}\left(\theta_0, \phi_0\right) = \mathbf{v}_{ch}\left(\theta_0, \phi_0\right), \tag{72}$$

$$\mathbf{w}_{sub}\left(\theta_0, \phi_0\right) = \mathbf{v}_{sub}\left(\theta_0, \phi_0\right). \tag{73}$$

The weights are used to steer their respective array factors as given by

$$W_{ch}\left(\theta, \phi\right) = \left[e^{\frac{i2\pi}{\lambda_0}\hat{\mathbf{k}}(\theta,\phi)\mathbf{D}_{ch}}\right]^T \mathbf{w}_{ch}\left(\theta_0, \phi_0\right), \tag{74}$$

$$W_{sub}\left(\theta, \phi\right) = \left[e^{\frac{i2\pi}{\lambda_0}\hat{\mathbf{k}}(\theta,\phi)\mathbf{D}_{sub}}\right]^T \mathbf{w}_{sub}\left(\theta_0, \phi_0\right). \tag{75}$$

When both of these sets of weights are steered towards a target and used to formulate the antenna pattern given by Equation (14), the resultant antenna pattern is referred to as the signal matched filter [29].

2.3.2 Optimum and Adaptive Spatial Filters.

In order to spatially filter interference, the weights are derived from estimates of the interference statistics as measured through the array manifold. Both $\mathbf{R}_{ch}$ and $\mathbf{R}_{sub}$ are non-singular and of full rank (as will always be the case due to the assumption of white Gaussian noise in the receive chain of each element). As $\mathbf{R}_{ch}$ and $\mathbf{R}_{sub}$ are of differing dimensionalities, the weight sets calculated from each will afford a differing number of DOF. First consider the weight set of the digitized array factor.

Of the $N_{ch}P_{ch}$ eigenvalues of the $N_{ch}P_{ch} \times N_{ch}P_{ch}$ covariance matrix, one will be set by the look angle of the array. Thus, $N_{ch}P_{ch} - 1$ eigenvalues remain to fulfill other constraints, such as casting nulls in the digital array factor. As such, $N_{ch}P_{ch} - 1$ is the number of adaptive DOF of the digital array factor. By following the same logic it can be concluded that $N_{sub}P_{sub} - 1$ is the number of adaptive DOF of the subarray factor. Therefore, if both array factors are made adaptive, one could potentially utilize $(N_{ch}P_{ch} - 1) + (N_{sub}P_{sub} - 1)$ adaptive DOF. When there is an ADC behind every element, the adaptive DOF simplifies to $NP - 1$.

The steering vector $\mathbf{v}_{ch}(\theta_0, \phi_0)$ can be used to calculate the optimum weights $\mathbf{w}_{ch}(\theta_0, \phi_0)$, also referred to as the Weiner filter, to apply to the digital channels. The Weiner-Hopf equation minimizes the mean square error between an estimated random process and a desired random process [30,31]. As the motivation of this research is to suppress barrage noise jamming signals impinging on a planar array, a matrix form of the Weiner-Hopf equation utilizing DOF in both azimuth and elevation can be used to calculate the optimum weight vector [32]

$$\mathbf{w}_{ch}(\theta_0, \phi_0) = \mathbf{R}_{ch}^{-1}\mathbf{v}_{ch}(\theta_0, \phi_0), \tag{76}$$

and the steering vector $\mathbf{v}_{sub}(\theta_0, \phi_0)$ can be similarly used to calculate the optimum weights to apply in hardware to the subarray elements

$$\mathbf{w}_{sub}(\theta_0, \phi_0) = \mathbf{R}_{sub}^{-1}\mathbf{v}_{sub}(\theta_0, \phi_0). \tag{77}$$

When both weight sets are calculated using clairvoyant knowledge of the noise and jamming statistics, and when used to form their respective array factors (as in Equations (74) and (75)) the resultant antenna pattern is referred to as the optimum spatial filter [29].

When clairvoyant knowledge of the noise and jamming statistics is not available, the weight sets can be adapted to estimated noise and jamming statistics as given by

$$\hat{\mathbf{w}}_{ch}(\theta_0, \phi_0) = \hat{\mathbf{R}}_{ch}^{-1}\mathbf{v}_{ch}(\theta_0, \phi_0), \tag{78}$$

$$\hat{\mathbf{w}}_{sub}(\theta_0, \phi_0) = \hat{\mathbf{R}}_{sub}^{-1}\mathbf{v}_{sub}(\theta_0, \phi_0). \tag{79}$$

When both weight sets are calculated using estimated knowledge of the noise and jamming statistics, and when used to form their respective array factors (as in Equations (74) and (75)) the resultant antenna pattern is referred to as the adaptive spatial filter [29].

2.3.3 Interference Mitigation Metrics.

In order to evaluate the performance of differing spatial filters, a number of interference mitigation metrics can be utilized. The Signal-to-Noise Ratio (SNR) for any given (θ, ϕ) through the subarrayed antenna is given by

$$SNR_{sub}(\theta, \phi) = N_{ch}P_{ch}\xi_m(\theta, \phi), \tag{80}$$

in which ξ_m represents the per-sample SNR for a single subarray, defined as

$$\xi_m(\theta, \phi) = \frac{P_t G(\theta, \phi) G_{sub}(\theta, \phi) \lambda_0^2 \sigma_t}{(4\pi)^3 L_s N_{sub} P_{sub} \sigma^2 R_t^4}, \tag{81}$$

in which P_t is the transmit power, $G(\theta, \phi)$ references the antenna pattern on transmit, $g(\theta, \phi)$ references the element pattern on receive, σ_t is the target Radar Cross Section (RCS), σ^2 is the noise power, R_t is the target range, and in which the noise power is coherently summed for all $N_{sub}P_{sub}$ elements of the subarray before the ADC. The

Signal-to-Interference and Noise Ratio (SINR) output of the subarrayed antenna is

$$SINR_{sub}(\theta,\phi) = \frac{\sigma^2 N_{sub} P_{sub} \xi_m(\theta,\phi) \left|\mathbf{w}_{ch}^H(\theta_0,\phi_0)\mathbf{v}_{ch}(\theta_0,\phi_0)\right|^2}{(\mathbf{w}_{ch}^H(\theta_0,\phi_0)\mathbf{R}_{ch}\mathbf{w}_{ch}(\theta_0,\phi_0))}, \tag{82}$$

in which N_{sub} and P_{sub} appear in the numerator to cancel the noise component of $\xi_m(\theta,\phi)$.

The coverage improvement metric for the subarrayed case utilizes $JNSR_{sub}$, defined as

$$JNSR_{sub}(\theta,\phi) = \frac{\mathbf{w}_{ch}(\theta_0,\phi_0)^H \mathbf{R}_{ch} \mathbf{w}_{ch}(\theta_0,\phi_0)}{\sigma^2 N_{sub} P_{sub} \xi_m(\theta,\phi) \left|\mathbf{w}_{ch}(\theta_0,\phi_0)^H \mathbf{v}_{ch}(\theta_0,\phi_0)\right|^2} = SINR_{sub}(\theta,\phi)^{-1}. \tag{83}$$

2.3.4 System Performance Metrics.

The percentage of the scannable volume denied to the system due to jamming serves as an important metric for evaluating a system's spatial nulling capability. A system's coverage area is defined here as the scannable area in azimuth and elevation over which the system is designed to operate. Coverage statistics are used in determining a particular adaptive antenna pattern's effectiveness in suppressing interference [33].

It is useful to calculate the Jamming and Noise-to-Signal Ratio (JNSR) over a search volume while fixing the interference sources, to gauge the impact of jamming as a function of look angle (for an example, see Figure 20). The JNSR can be quantified by plotting the percentage of the field of view having a JNSR that is less than a threshold.

While JNSR is useful for analyzing the effect of a single adaptive filtering method, it is useful to have a metric which compares the results of two different filtering methods. The Coverage Improvement Factor (CIF) is a ratio which shows the improvement

of an adaptive technique over the quiescent (i.e. non-adaptive) response at one particular look angle by comparing the JNSR of each [33], as given by

$$CIF(\theta,\phi) = \frac{JNSR_Q(\theta,\phi)}{JNSR_A(\theta,\phi)}, \tag{84}$$

for which $JNSR_Q$ is the JNSR of the quiescent response and $JNSR_A$ is the JNSR of the adaptive response. The CIF statistics can be visualized by plotting the field of view percentage at which the adaptive response provides a given level of JNSR improvement relative to the non-adaptive response.

2.4 Relevant Research Efforts

A variety of research efforts with related motives have been undertaken in recent years. Many of these are based on underwater SOund Navigation And Ranging (SONAR) applications that have analogs to the RF environment. In [34] methods for nulling transient interference sources in short time intervals are examined. Restricting the time interval for adaptation causes the unwanted effect of error in the weights which are generated (error which could supercede any performance gains from a faster adaptive interval). Thus, for short interval adaptation, weights are able to be generated. The goal of the research was to effectively null the transient interferer with a limit on the number of weights. The few weights adapted to the transient interferer are then only applied on the time scale in which the transient interferer is present, and the full set of adaptive weights is used for the long duration interference sources.

Multi-rate adaptive nulling within the field of SONAR is examined in [35] and [36]. Receive arrays of SONAR systems can grow to very large sizes, with a similarly large number of elements. A larger number of elements requires a longer snapshot to be

taken in order to create a covariance matrix. In the time it takes some SONAR systems to create this covariance matrix, as limited by both the number of samples that need to be gathered and the time it takes for a wavefront to traverse the entire array face, interferers may have moved by a nontrivial amount. Cox proposes a solution not dissimilar to the one developed in [34] in which a lower rank covariance matrix is simultaneously formed at a more frequent interval. In this lower rank subspace, moving interferers can be tracked and nulled while the larger covariance matrix is being built, thus allowing weaker signals to be detected despite the presence of moving interferers.

In the field of radar, strides have been made in using adaptive algorithms to improve nulling in the presence of interference. In [37] and various associated reports ([38], [39]), the processing limits that can be imposed through adaptive beamforming are examined. For large arrays which have an ADC behind each element, adapting on all DOF for every iteration is very processor intensive. Rabideau proposes a method by which known jammers, once initially found, are nulled at a seperate processor stage controlling a subset of the total DOF. Thus, the processor does not have to waste power by readapting to known jamming presences. Of course, motion of the acquired jammers can then cause significant performance drop off.

As a known antenna manifold is central to the argument of this thesis, it is worthy to note [17] which proposes an algorithm that uses knowledge of the statistics of sea clutter to recalibrate the manifold of a ship-borne radar system while deployed. Such an algorithm, in conjuction with knowledge-aided techniques such as those postulated by DARPA's KASSPER program [40], could in the future potentially be capable of calibrating an airborne radar antenna using the clutter statistics of a known patch of ground while in operation.

Spectral estimation using subarrayed phased array antennas has already been

postulated, initially in [8] and extended in [7]. Both offerings feature the practicality that a fully known antenna manifold is not required (as many radar subarrayed radar systems contain thousands of elements). Rather, they calculate the MUltiple SIgnal Classification (MUSIC) spectrum form the subarray phase centers using the known subarray gains. While practical, this approach constrains the number of angle of arrivals (AOAs) returned to the $C-1$ channel limit inherent to eigenvalue based spectral analysis techniques [41].

It should be mentioned that any of a long lineage of algorithmic spectral estimation techniques (i.e. those found in [41–43] to note a few main contributions) could, and potentially should, be applied in providing the "knowledge" component necessary for the analog subarray adaptation presented in this thesis. Of historical note in relation to this thesis is [44] which first boasted the ability to estimate the AOAs of multiple signal sources using an adaptive antenna array. Berni's algorithm harnessed a control loop which was designed to adaptively cancel incident signals with the analog beam pattern. The concavities of the final pattern after all signals were cancelled offered up to $C-1$ AOA estimates. Berni's method was unique in that it combined analog beamforming and digital processing, and as such offers a historical analog to this thesis today.

III. Methodology

The investigative method of this research is software simulation. The spatial filters evaluated in this research are formed using five different methods. Each of the methods will be explained, culminating in the Knowledge-Aided Subarray Pattern Synthesis (KASPS)-Adaptive Digital Beamforming (ADBF) method which is the major contribution of this research. Next, a concept of operations for the KASPS-ADBF method is postulated. In demonstrating the KASPS-ADBF method, prior knowledge of the jamming signal angle of arrival (AOA) in elevation and azimuth, (θ_j, ϕ_j), and jammer power at the array face is assumed (i.e., knowledge-aided). To investigate the effectiveness of the KASPS-ADBF method in the presence of AOA estimation error, aperture error, and when the subarray weights are quantized (a necessity of hardware implementation; hardware represented in Figure 4), a sensitivity analysis of the KASPS technique will be performed.

3.1 Antenna Pattern Methodologies

In Section 2.3 it was shown how weight sets can be calculated to either steer or adapt the digital array factor and subarray factor. In this section it will be shown how these weights can be calculated and applied in order to spatially filter via five different methods of varying levels of adaptivity. Figure 5 may be referenced to provide the reader with a quick visual reference for the technique used to create the results in question. Digital Beam Steering (DBS) refers to an array with an analog-to-digital converter (ADC) behind every element for which no digital adaptivity has been applied. ADBF refers to an array with an ADC behind every element for which digital adaptivity has been applied. Subarray Beam Steering (SBS)-DBS refers to a subarrayed array for which no digital adaptivity or subarray adaptivity has

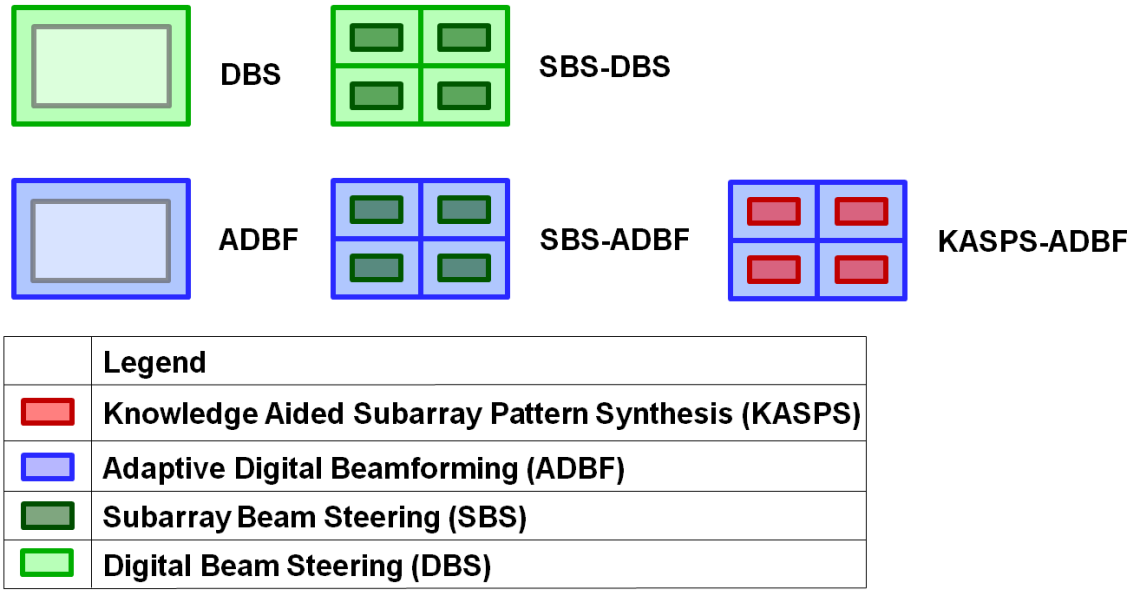

Figure 5. Legend for the pattern forming techniques used to generate the results throughout Chapter IV.

been applied. SBS-ADBF refers to a subarrayed array for which digital adaptivity has been applied but subarray adaptivity has not. Finally, KASPS-ADBF refers to a subarrayed array for which digital adaptivity is applied while subarray pattern synthesis is also in use.

3.1.1 Digital Beam Steering (DBS).

For arrays which possess an ADC behind every element ($N_{sub} = P_{sub} = 1$), all weighting may occur digitally. Thus, there are no hardware weights in the element receive chains, and only the set of digital weights, $\mathbf{w}_{ch}$, is calculated. The antenna pattern of such an array may be steered by this digital weight set, as described in Section 2.3.1. This method is referred to herein as DBS. The resulting antenna pattern constitutes a non-adaptive spatial filter, and in a noise-only environment will provide the best Signal-to-Noise Ratio (SNR) for the desired look direction. The digital weight set is used to non-adaptively steer the beam as depicted in Figure 6.

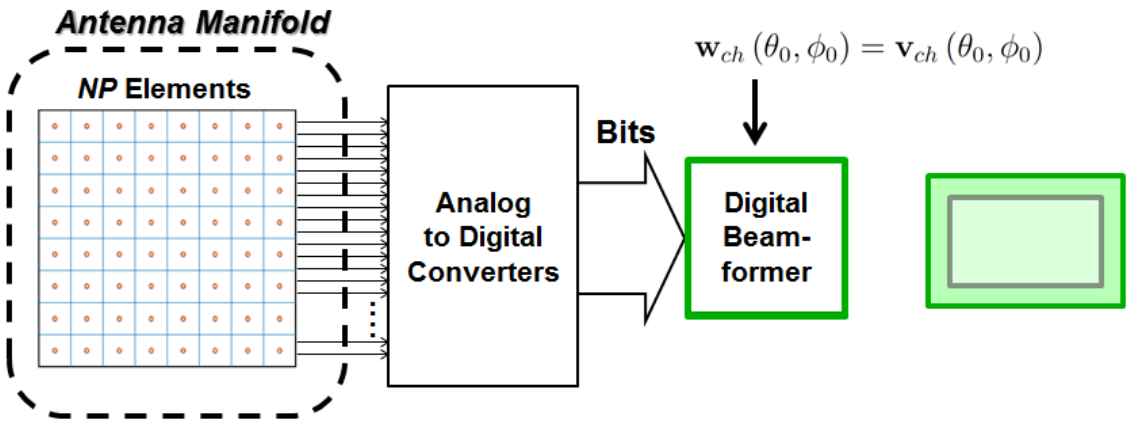

Figure 6. Processing chain depicting how digital weights are used to steer the beam of an array with an ADC behind each element.

3.1.2 Adaptive Digital Beam Forming (ADBF).

In keeping with an array possessing an ADC behind every element ($N_{sub} = P_{sub} = 1$) for which only the set of digital weights is calculated, $\mathbf{w}_{ch}$ may be adapted to the noise and interference of the environment. The antenna pattern of such an array is formed by this digital weight set, as described in Section 2.3.2. This method is referred to herein as ADBF. The resulting antenna pattern constitutes an adaptive spatial filter, and in a noise plus interference environment will provide the best Jamming and Noise-to-Signal Ratio (JNSR) for the desired look direction. Having an ADC behind each element yields a "fully adaptive" solution, as this configuration yields the highest number of adaptive degrees of freedom (DOF) ($NP - 1$). The digital weight set is used to adaptively form the beam as depicted in Figure 7.

3.1.3 Subarray Beam Steering-Digital Beam Steering (SBS-DBS).

When subarrays are introduced into the array architecture ($N_{sub} > 1$ and/or $P_{sub} > 1$), the set of subarray weights must be calculated in addition to the set of digital weights. In the absence of interference, an antenna may steer each of the subarrays towards a direction of interest and also steer the digital array factor towards

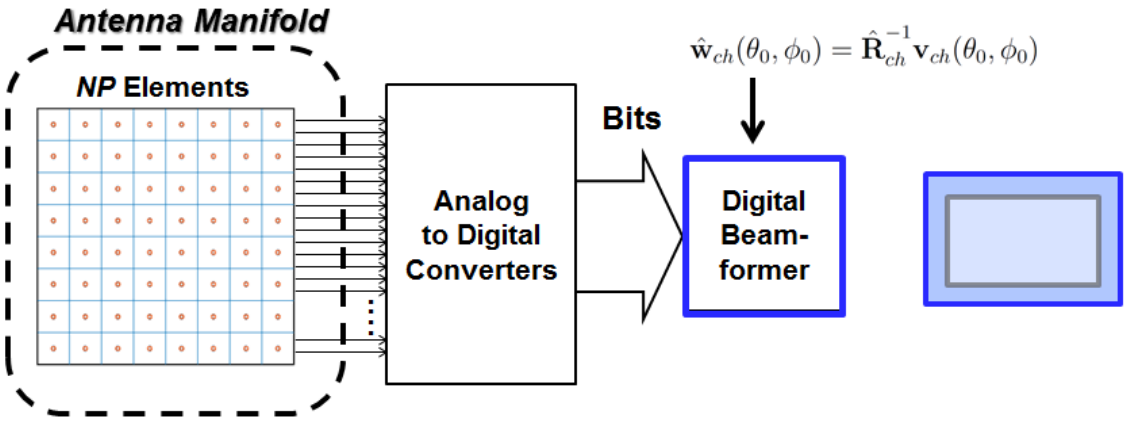

Figure 7. Processing chain depicting how digital weights are used to adapt the beam of an array with an ADC behind each element.

the direction of interest in order to place maximum subarray gain on a target. This method is referred to herein as SBS-DBS. The subarray factor and digital array factor of such an array may be steered by their respective weight sets, as described in Section 2.3.1. As such, the resultant antenna pattern constitutes the non-adaptive spatial filter. The antenna pattern of this spatial filter is formed by the subarray and digital weight sets, as depicted in Figure 8.

3.1.4 Subarray Beam Steering-Adaptive Digital Beam Forming (SBS-ADBF).

As noted above, when subarrays are introduced into the array architecture ($N_{sub} > 1$ and/or $P_{sub} > 1$), the set of subarray weights must be calculated in addition to the set of digital weights. Conventional subarrayed antennas steer each of the subarrays towards the direction of interest in order to place maximum subarray gain on the target, and then adapt the digital array factor in order to mitigate interference received through the subarray pattern. This method is referred to herein as SBS-ADBF. The subarray factor of such an array may be steered by the subarray weight set, as described in Section 2.3.1. The digital array factor is adapted to the noise and

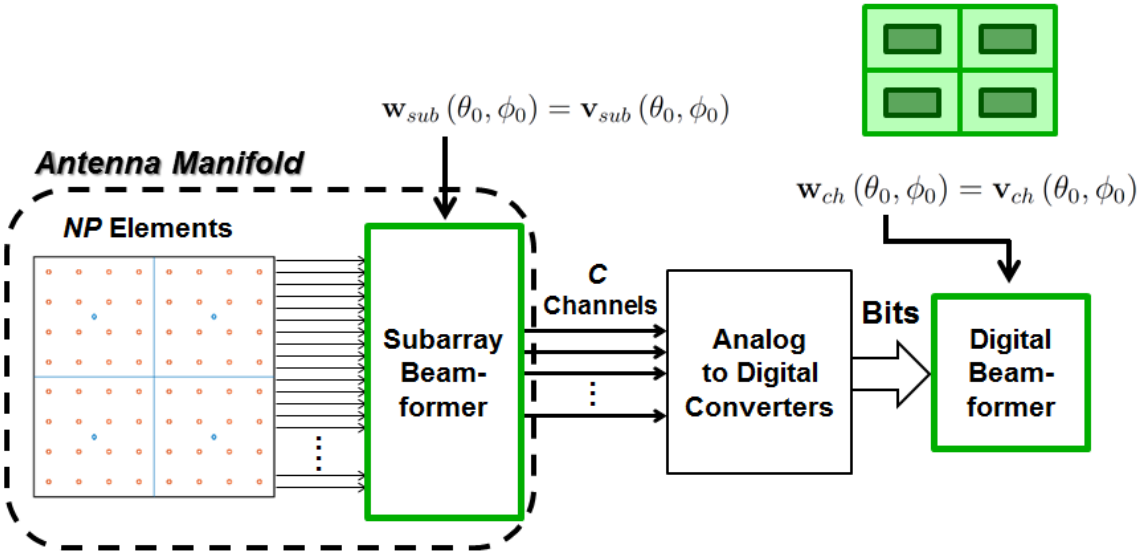

Figure 8. Processing chain depicting how both subarray and digital weights are used to steer the beam of a subarrayed antenna.

interference of the environment as received through the subarray factor. As such, the subarray factor is reflective of the non-adaptive spatial filter and the digital array factor is reflective of the adaptive spatial filter. The antenna pattern of this spatial filter is formed by the subarray and digital weight sets, as depicted in Figure 9.

3.1.5 Knowledge Aided Subarray Pattern Synthesis-Adaptive Digital Beam Forming (KASPS-ADBF).

In order to improve the interference suppression capabilities of subarrayed systems, it may be advantageous to use the subarray weights to adapt the subarray factor to the noise and interference of the environment, as is shown in Equation (79), as is done in ADBF. However, calculating adaptive subarray weights in practice presents a challenge not faced in calculating adaptive digital weights. In calculating the adaptive digital weight set the covariance matrix, $\hat{\mathbf{R}}_{ch}$, can be estimated in the radar processor. By contrast, there is no way to observe the subarray covariance matrix, $\hat{\mathbf{R}}_{sub}$, within the antenna manifold. Thus, a synthetic covariance matrix, $\bar{\mathbf{R}}_{sub}$, must be generated

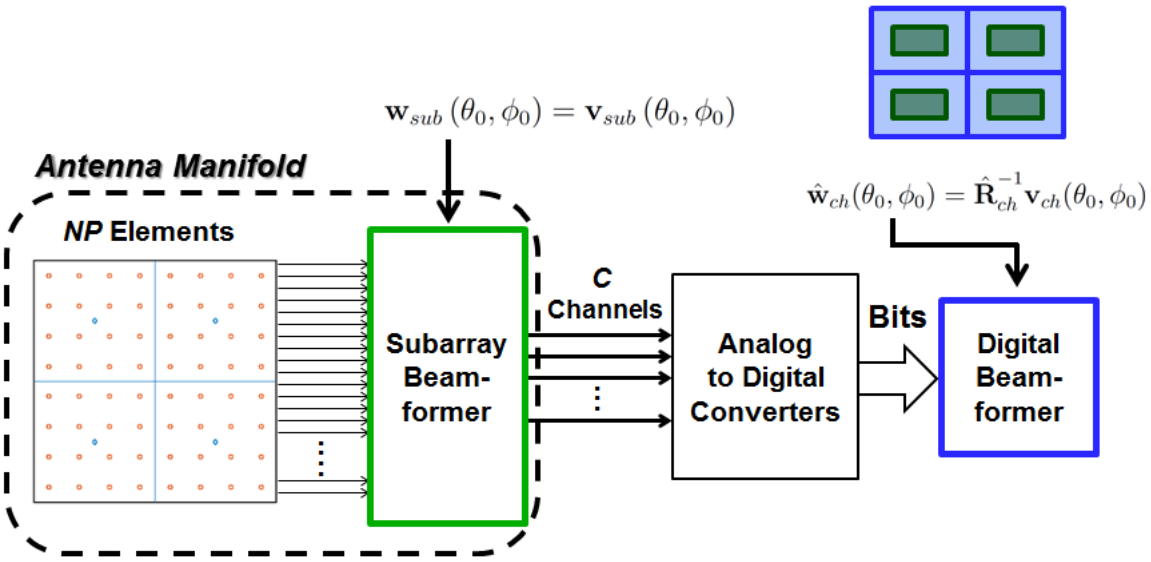

Figure 9. Processing chain depicting how subarray weights are used to steer the subarray factor and digital weights are used to adapt the digital array factor of a subarrayed antenna.

(as opposed to measured) in order to facilitate the calculation of the adaptive subarray weights

$$\bar{\mathbf{w}}_{sub}(\theta_0, \phi_0) = \bar{\mathbf{R}}_{sub}^{-1}\mathbf{v}_{sub}(\theta_0, \phi_0). \tag{85}$$

The subarray covariance matrix, $\bar{\mathbf{R}}_{sub}$, can be synthesized in keeping with the development throughout Section 2.1 culminating in Equation (65). However, this synthesis requires knowledge of the jammer locations in azimuth and elevation, and the jammer power at the array face. Appendix A proposes methods by which this information may be known. Throughout this research, knowledge of the jammer parameters will be assumed unless otherwise stated. With the set of adaptive subarray weights and adaptive digital weights generated, the beam pattern may be formed as depicted in Figure 10.

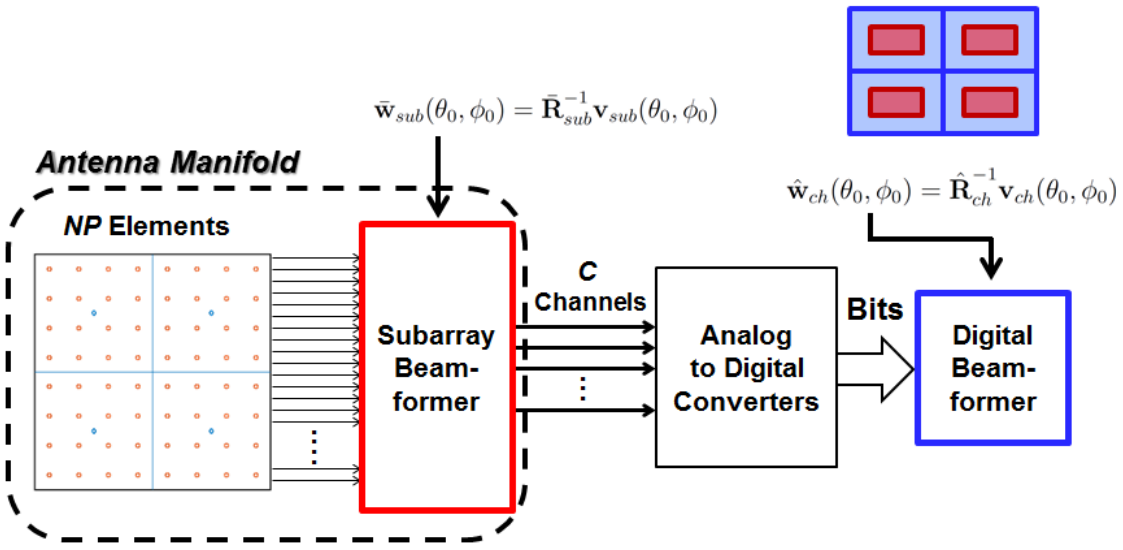

Figure 10. Processing chain depicting how both subarray weights and digital weights may be used to adapt the antenna pattern of a subarrayed antenna.

3.2 KASPS Concept of Operations

The KASPS-ADBF pattern forming method as described in Section 3.1 places real nulls in the direction of all jammers. This strategy, however, is not necessarily the best usage of the real and digital DOF of the array. Consider a simple scenario in which the desired look angle is $(5^o, -25^o)$, Jammer 1 is at $(5^o, -30^o)$, and Jammer 2 is at $(5^o, 25^o)$. If the phased array only has two channels, then there are not enough digital DOF to null both jammers. Thus, in this scenario the radar performance may be improved by using KASPS to suppress interference. However, it is not necessary to suppress both jamming signals using the subarray pattern. The first jammer is very near to the desired look angle. Placing a null in the subarray pattern so close to the look angle would lead to a large loss of gain in the look direction, which would reduce the signal strength of a hypothetical target return from that direction. Thus, in certain cases, it is advantageous to use the subarray pattern to null select interference signals, thereby freeing the digital DOF to null the remaining signals. This decision, made within the radar processor, is implemented in the synthesis of $\bar{\mathbf{R}}_{sub}$. If $\bar{\mathbf{R}}_{sub}$

is synthesized to only acknowledge the existence of the jamming signal for which nullification is desired (in this case, Jammer 2 at $(5^o, 25^o)$). The resultant subarray weight set, $\bar{\mathbf{w}}_{sub}$, when applied to the subarray elements will only null Jammer 2. The radar processor will then observe a new covariance matrix through the digitized channels, $\hat{\mathbf{R}}_{ch}$, for which Jammer 2 has been made minimum. The digital weights, $\hat{\mathbf{w}}_{ch}$ are calculated using Equation (78). As Jammer 2 will effectively no longer be sensed by the radar processor, the digital weights, $\hat{\mathbf{w}}_{ch}$, will then null Jammer 1 with the lone digital DOF available to the system.

In this research, the decision to null a jammer digitally or via the subarray pattern is made via the KASPS algorithm, represented in Figure 11. Consider again the example given above (and illustrated in Figure 12) with 2 jammers in the scene J is equal to 2. The radar determines a location of interest and steers the mainbeam towards that location. It is not placing any subarray pattern nulls so the constraint list (i.e., the nulls to be placed in the subarray pattern) is empty. The JNSR is measured without any subarray pattern nulls, meaning that only ADBF is being used to suppress any interference. The JNSR is then measured with a subarray null placed towards the first jammer. The JNSR is then measured with a null placed towards the second jammer. The three measurements are compared. If the nulls have not improved the JNSR, the unadapted subarray pattern is used. If one of the nulled subarray patterns produces the lowest JNSR, it is stored as a constraint in the KASPS constraint list. Now the algorithm will test to see if adding an additional null to the constraint already found will yield even better performance. With only one other jammer to test for the second null, J now equals 1. The second null is cast in the pattern and the JNSR is measured. If the JNSR has been improved, both subarray pattern nulls will be cast. If the JNSR has not been improved only the initial subarray pattern null will be cast. In this way, the performance of the array, for a

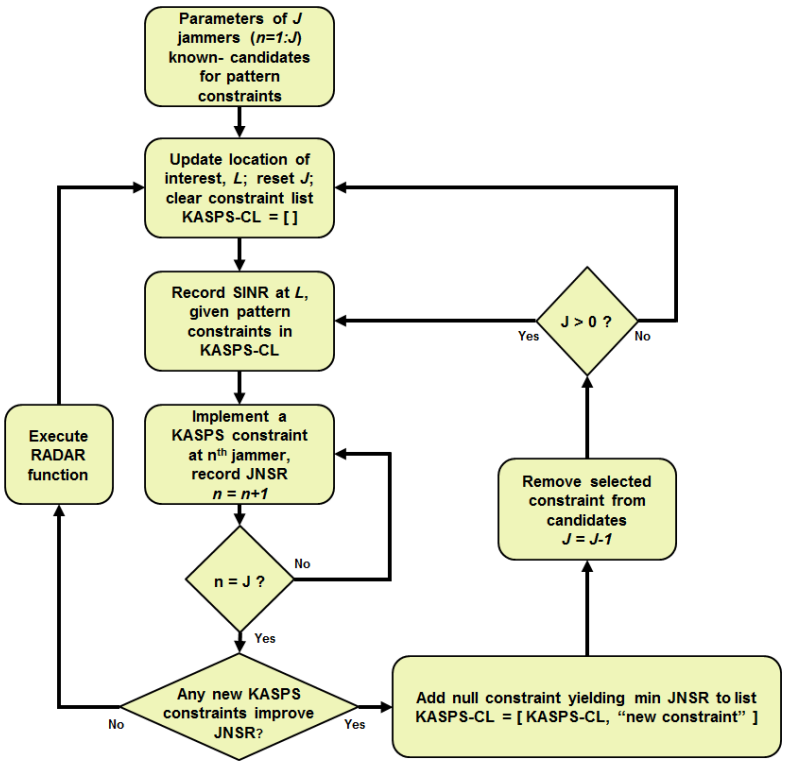

Figure 11. Flow diagram demonstrating how the subarray pattern nulling decision is algorithmically determined.

given look angle, can be iteratively improved. Figure 12 demonstrates the subarray pattern jammer nulling decision for the example, as made at each look angle across the field of view. At the look angle discussed in the example, $(5^o, -25^o)$, it can be seen that only one of the jamming signals is nulled by the subarray pattern. This algorithm has not been found to be optimal, nor analyzed for processing efficiency. It is being postulated here as a concept of operations to demonstrate the potential benefits of the KASPS technique. More refined algorithmic solutions utilizing the KASPS technique could and should be developed.

3.3 Sensitivity Analysis

The performance of the KASPS-ADBF method will degrade in the presence of AOA estimation error, aperture error, or when the hardware subarray weights are

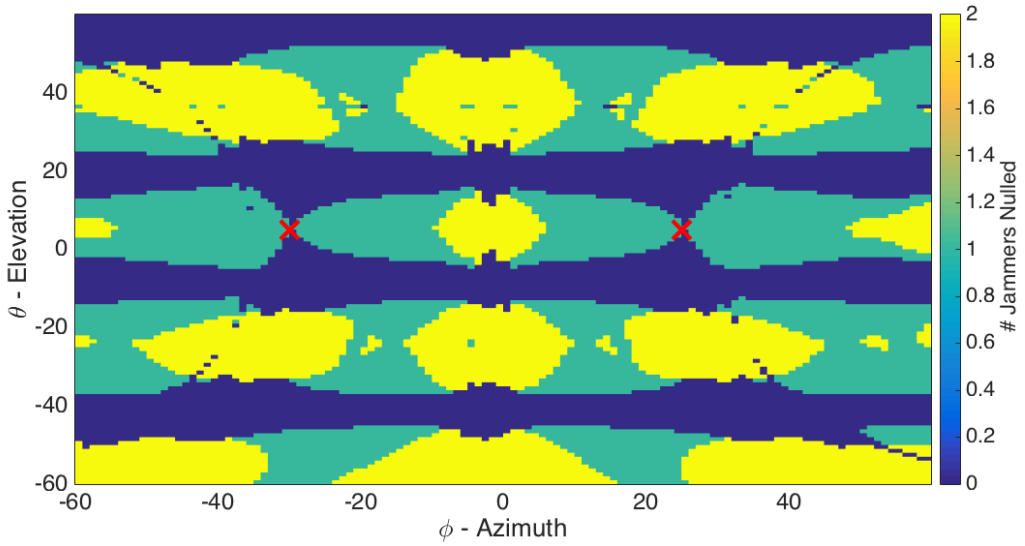

Figure 12. The various colored fields indicate the number of jammers nulled by the subarray pattern for the given look angle, as determined by the KASPS algorithm, detailed in Figure 11. Red X's indicate the jammer locations.

quantized. Each of these sources of error are examined independently.

3.3.1 Angle of Arrival Estimation Error.

The KASPS technique relies on accurate knowledge of the AOAs of interfering signals, and of the power of those signals at the array face. Whether this information is known from external sources or was estimated by the radar, error in the interference AOA will result in nulls which are not accurately centered on the interfering signal. Thus, the interference will not be reduced by the subarray factor to the fullest extent possible, and may still appear as a strong jamming source at the radar processor. While the majority of results in this thesis are solved without accounting for the effects of jammer AOA error, jammer AOA is purposefully placed in error in a series of increasing 1^o steps so that the performance of KASPS in the presence of jamming AOA estimation error can be analyzed in Section 4.3.1.

3.3.2 Aperture Error.

The KASPS technique assumes a known and calibrated antenna manifold. Imperfect knowledge of the manifold can result from a number of sources, including an un-calibrated manifold or machining errors of the aperture. In order to analyze the effects of aperture error on the KASPS-ADBF method, a matrix of the true element positions, $\mathbf{D}$ is defined, and a matrix of estimated element positions, $\hat{\mathbf{D}}$ is defined. The matrix $\hat{\mathbf{D}}$ represents where the radar processor believes the elements lie. The radar processor, in this research, assumes perfectly uniform half-wavelength spaced elements. The true element positions are placed in error by a random amount of some percentage, X, of the half-wavelength spacing distance, as given by

$$e_x \sim \mathcal{N}\left(0, \frac{Xd_x}{100}\right), \tag{86}$$

$$\mathbf{e}_x = [e_{x,1} \quad \dots \quad e_{x,NP}], \tag{87}$$

$$e_z \sim \mathcal{N}\left(0, \frac{Xd_z}{100}\right), \tag{88}$$

$$\mathbf{e}_z = [e_{z,1} \quad \dots \quad e_{z,NP}], \tag{89}$$

$$\mathbf{E} = \begin{bmatrix} \mathbf{e}_x \\ 0_{1xNP} \\ \mathbf{e}_z \end{bmatrix}, \tag{90}$$

$$\mathbf{D} = \hat{\mathbf{D}} + \mathbf{E}. \tag{91}$$

When the adaptive digital weight set is calculated by the radar processor (as in Equation (78)), the estimated covariance matrix $\hat{\mathbf{R}}$ reflects the statistics of the signal received through the true aperture, $\mathbf{D}$. The steering vector, $\hat{\mathbf{v}}(\theta_0, \phi_0)$, however, is formed using the radar processor's calibrated but flawed knowledge of the aperture, denoted as $\hat{\mathbf{D}}$. This effect is called steering vector mismatch [28] and results in a

mismatched adaptive spatial filter, $\widehat{\mathbf{w}}(\theta, \phi)$. Imperfections of the filter will result in degraded JNSR, calculated by

$$JNSR_{sub}(\theta, \phi) = \frac{\widehat{\mathbf{w}}_{ch}(\theta_0, \phi_0)^H \mathbf{R}_{ch} \widehat{\mathbf{w}}_{ch}(\theta_0, \phi_0)}{\sigma^2 N_{sub} P_{sub} \xi_m(\theta, \phi) \left| \widehat{\mathbf{w}}_{ch}(\theta_0, \phi_0)^H \mathbf{v}_{ch}(\theta_0, \phi_0) \right|^2}. \tag{92}$$

The KASPS technique relies on synthesizing covariance matrix $\bar{\mathbf{R}}_{sub}$ in order to generate the adaptive subarray weights, $\bar{\mathbf{w}}_{sub}$. In this case, imperfect knowledge of the aperture will also affect the $\bar{\mathbf{R}}_{sub}$ synthesis. The adaptive subarray weights are then in error due to both the mismatched synthesized covariance matrix, $\widehat{\bar{\mathbf{R}}}_{sub}$, and the mismatched steering vector $\hat{\mathbf{v}}_{sub}(\theta_0, \phi_0)$, and are calculated as

$$\widehat{\bar{\mathbf{w}}}_{sub}(\theta_0, \phi_0) = \widehat{\bar{\mathbf{R}}}_{sub}^{-1} \hat{\mathbf{v}}_{sub}(\theta_0, \phi_0). \tag{93}$$

Thus, the resultant JNSR is affected by the mismatch of both $\widehat{\mathbf{w}}_{ch}(\theta_0, \phi_0)$ and $\widehat{\bar{\mathbf{w}}}_{sub}(\theta_0, \phi_0)$. While most results in this thesis are reported without accounting for the aperture error effects, Section 4.3.2 analyzes the impact of increasing amounts of aperture error (X). As such, the performance of KASPS-ADBF is analyzed as a function of manifold error.

3.3.3 Weight Quantization.

In real hardware applications, an infinite resolution in setting phase and gain weights, and infinite dynamic range in setting gain weights is not possible [45]. The resolution of the phase of the weights is limited by the number of bits in the phase shifter and the resolution of the gain of the weights is limited by the number of bits in the attenuator (phase shifter and attenuator pictured in Figure 4). Weight quantization can limit the system's ability to accurately steer the beam or place nulls in jammer directions if insufficient bits in gain and phase are available, which can lead

to quantization lobes in the antenna pattern [5]. Thus, in order to simulate realizable systems, after the real subarray phase weights, $\bar{\mathbf{w}}_{sub}$, are synthesized they must be quantized based on system specifications, as in [45]. While the majority of results in this thesis are solved without accounting for the effects of quantization, Section 4.3.3 provides an investigation into the effects of quantization on the KASPS technique.

IV. Results

This chapter presents the results of executing the methodology described in Chapter III. In order to demonstrate comparable results across all techniques considered herein, only two scenarios are considered.

Scenario 1 is comprised of a 8 x 8 array ($N = P = 8$) with the system properties displayed in Table 1. Scenario 1 will be considered in both an "ideal" sense (i.e. analog-to-digital converter (ADC) behind each element) and as a subarrayed architecture (detailed in Table 5) so that the differences in performance between the two architectures may be identified. The transmit power, P_t, was chosen to set the maximum Signal-to-Noise Ratio (SNR) of the system equal to 10 dB. Parameters are held constant across all techniques for Scenario 1. Table 2 describes a set of jammers and their properties. Various subsets of this larger set of jammers will be used in Scenario 1 throughout the chapter. Scenario 1 was tailored to be purposefully simple, so that the mechanism and efficacy of the Knowledge-Aided Subarray Pattern Synthesis (KASPS) method may be clearly observed.

Scenario 2 was designed to represent a more realistic radar of larger dimensions so that the real-world applicability of KASPS may be approximated. Scenario 2 is comprised of a 20 x 20 array ($N = P = 20$) with the system properties displayed in Table 3. Scenario 2 will also be considered in both an "ideal" sense (i.e. ADC behind each element) and as a subarrayed architecture (detailed in Table 7) so that the differences in performance between the two architectures may be identified. The transmit power, P_t, was chosen to set the maximum SNR of the system equal to 10 dB. These values are held constant across the host of techniques being analyzed in Scenario 2.

Table 1. System properties for Scenario 1.

Parameter	L_s (dB)	θ_0 (GHz)	σ_t (m^2)	P_t (kW)	R_t (m)	σ^2 (kW)
Value	3	1.24	10	10	2000	$1.25x10^{-12}$

Table 2. Jammer parameters for scenarios analyzed throughout Chapter IV.

Jammer	ϕ (^{o})	θ (^{o})	S_j (W)	R_j (km)
1	-30^o	5^o	100	100
2	25^o	-25^o	100	100
3	-15^o	-35^o	100	100
4	0^o	-40^o	100	100
5	15^o	15^o	100	100
6	-40^o	-10^o	100	100
7	8^o	-20^o	100	100
8	-30^o	15^o	100	100

Table 3. System properties for Scenario 2.

Parameter	L_s (dB)	λ_0 (GHz)	σ_t (m^2)	P_t (kW)	R_t (m)	σ^2 (kW)
Value	3	10	10	2.7	2000	$1.25x10^{-12}$

4.1 Performance Bounds

Table 4 describes an antenna with no subarrays (an ADC behind each element), yielding 63 digital degrees of freedom (DOF). Figure 13 shows the Noise-to-Signal Ratio (NSR) when $J = 0$ calculated using the antenna from Table 4. Figure 14 shows the gain pattern of a single element of the array (Equation (16)). By comparing Figure 13 to Figure 14, it becomes apparent that the contour of the NSR output across the field of view correlates to the dropoff in element pattern gain. Thus, minimum NSR (which is -10 dB) occurs at boresight, $(0^o, 0^o)$, and increases to maximum (-6 dB) as either azimuth (ϕ^o) or elevation (θ^o) reaches 60^o (the extent of the field of view examined). The result seen in Figure 13 serves as the "best" (i.e., noise only) result that can be obtained from the Scenario. As such, Figure 13 represents an upper bound on performance, as compared to performances observed in the presence of interference. In keeping with the use of these results as an upper bound on performance, these results were calculated using clairvoyant knowledge of the noise (as opposed to estimating the noise covariance matrix from training data). All results for non-subarrayed (i.e., "ideal") antennas throughout this chapter are calculated with clairvoyant covariance matrices so as to establish upper bounds on performance. The blue (+) line of Figure 28 shows the coverage statistics of the noise only response by indicating the percentage of the field of view (from -60^o to 60^o in elevation and azimuth) from Figure 13 for which Jamming and Noise-to-Signal Ratio (JNSR) is less than the value specified on the x-axis. For instance, it can be observed from Figure 28 that under these conditions 98% of the look angles experience less than 0 dB JNSR. For coverage statistics plots, curves exhibiting better performance will approach the upper left hand corner.

Table 5 describes the subarrayed antenna used in Scenario 1. This antenna contains an ADC behind each of the 4 subarrays, yielding a maximum of 3 adaptive

Table 4. Antenna properties for the "idealized" case of Scenario 1 (shown in Figure 13).

Parameter	N_{ch}	P_{ch}	N_{sub}	P_{sub}
Value	8	8	1	1

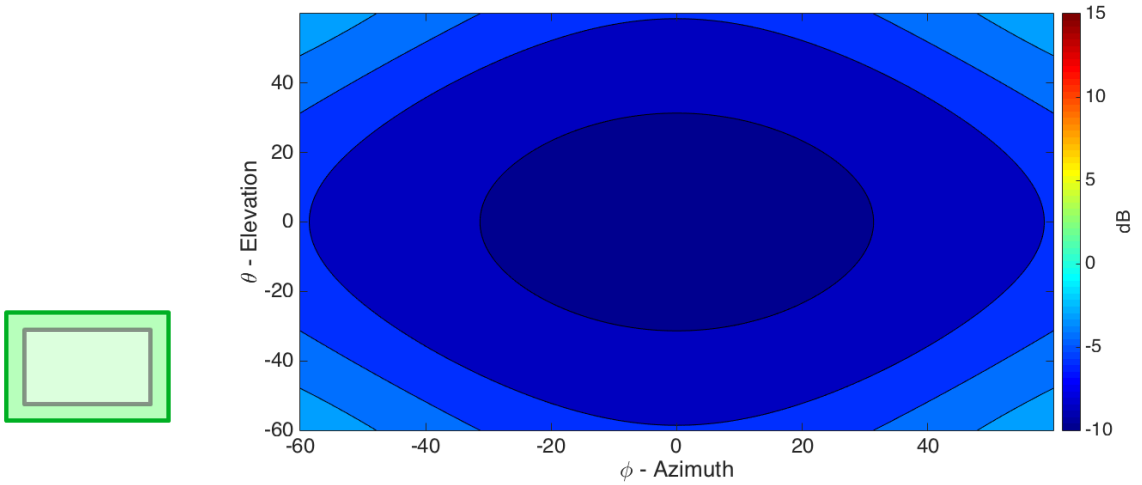

(a) DBS (b) JNSR Output

Figure 13. JNSR output for the non-subarrayed 8 x 8 antenna described in Table 4 in a noise only environment.

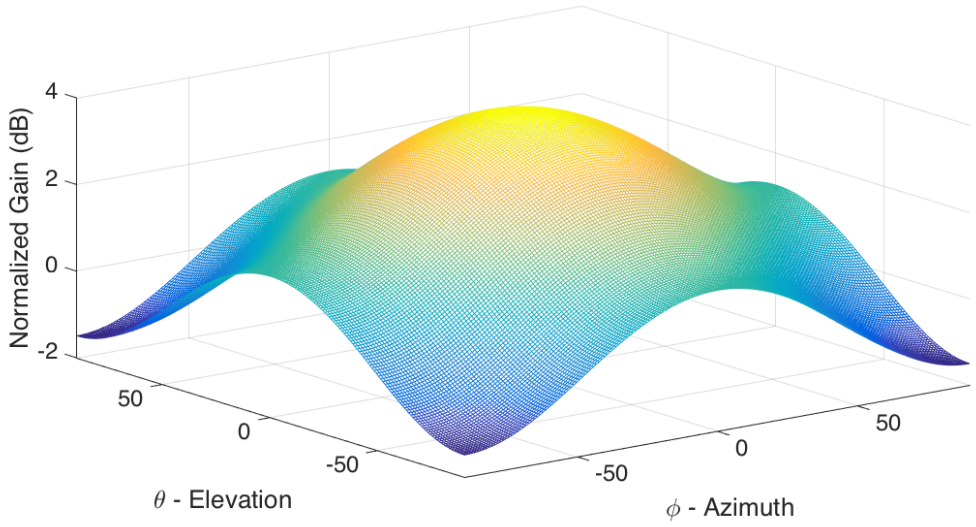

Figure 14. Single element gain pattern, given by Equation (16).

Table 5. Antenna properties for the subarrayed case of Scenario 1.

Parameter	N_{ch}	P_{ch}	N_{sub}	P_{sub}
Value	2	2	4	4

digital DOF. Each subarray contains 16 elements, which are theoretically capable of providing 15 spatial DOF. Figure 15 shows the NSR calculated for the noise only case using the antenna from Table 5. By comparing Figure 15 to Figure 13, it can be seen that practically equivalent outputs are obtained, as would be expected due to the equivalency of the antenna patterns from both architectures as detailed in Section 2.1.1. The subarrayed results are very slightly degraded because they were generated using covariance matrices estimated from $t = 2NP$ training data observations as opposed to clairvoyant knowledge of the noise and jamming statistics. All results for subarrayed antennas are calculated with covariance matrices estimated from $t = 2NP$ training data observations in an effort to depict realistic performance. Despite equivalent antenna patterns, however, the digital array factors of the two architectures are not equivalent. This will result in different responses from each array architecture once jamming is introduced.

Section 3.1 describes the method by which digital weights, $\hat{\mathbf{w}}_{ch}$, may be applied to each digitized channel to digitally null interference sources, referred to as Adaptive Digital Beamforming (ADBF). For the antenna described by Table 4, 63 digital DOF are available for adaptive mitigation of jamming signals. Introducing Jammer 1 from Table 2 and using the "ideal" antenna described in Table 4, and applying the ADBF method results in the JNSR output seen in Figure 16. Observing the same environment through the subarrayed antenna described in Table 5, and applying ADBF results in the JNSR output seen in Figure 17. This subarrayed antenna posseses 3 digital DOF, so it would be reasonable to assume that ADBF would be sufficient to

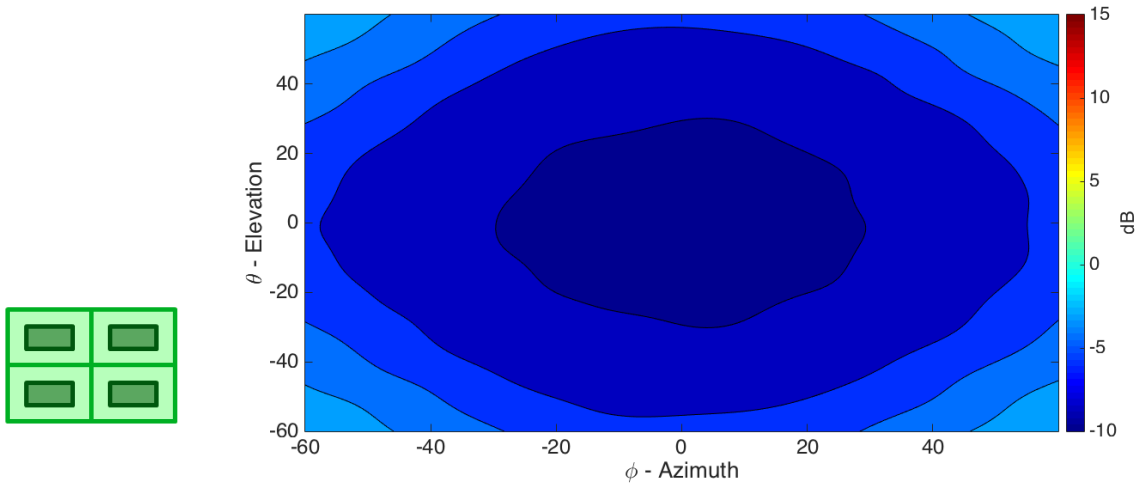

(a) SBS-DBS (b) JNSR Output

Figure 15. JNSR output for the subarrayed antenna described in Table 5 in a noise only environment.

fully suppress the interference from a single jammer. And yet, additional regions of degraded performance are clearly observable in the field of view.

The additional degraded regions in Figure 17 represent ambiguous returns due to grating lobes in the digital array factor, as examined in Section 2.1.1. For instance, when the radar has a look angle of $(5^o, 0^o)$, Equation (19) can be used to show the presence of a grating lobe very near the jammer location, $(5^o, -30.1^o)$. Thus, when the radar is steered towards $(5^o, 0^o)$, the perceived return from that direction will include the returns from all grating lobes, which include $(-24.4^o, -33.3^o)$, $(36^o, -38.1^o)$, $(-24.4^o, 0^o)$, $(36^o, 0^o)$, $(-24.4^o, 33.3^o)$, $(5^o, 30.1^o)$, and $(36^o, 38.1^o)$, as attenuated by the subarray pattern. Streaks of low JNSR can also be witnessed through the degraded regions of Figure 17. The digital array factor and quiescent subarray pattern for a radar look angle of $(5^o, 0^o)$ are shown in Figure 18 and Figure 19 respectively so that the reader may observe these effects. The quiescent nulls in the subarray pattern aline with the streaks of low JNSR in Figure 17, suggesting that quiescent subarray

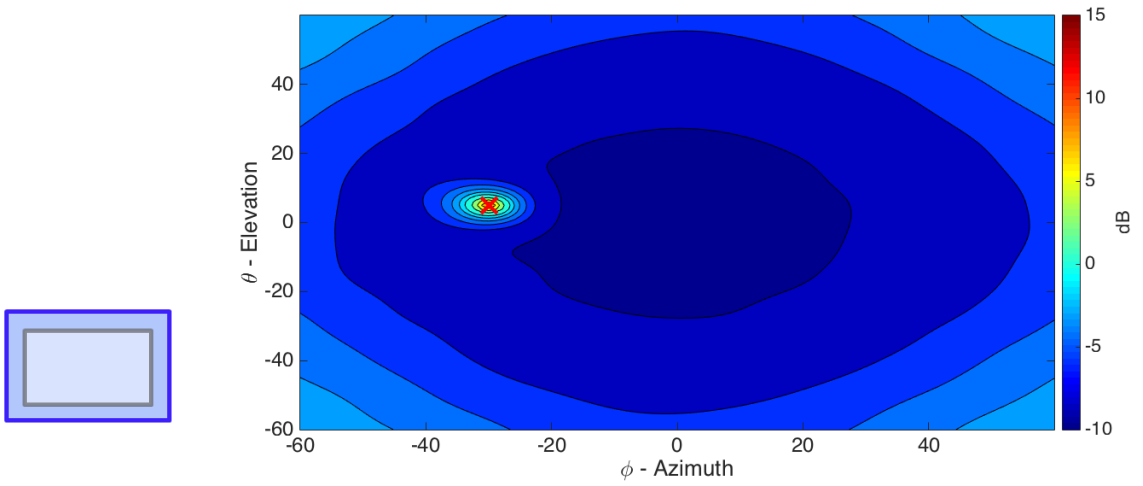

(a) ADBF (b) JNSR Output

Figure 16. JNSR output after ADBF for the antenna described in Table 4 with Jammer 1 from Table 2 present. The red X indicates jammer location.

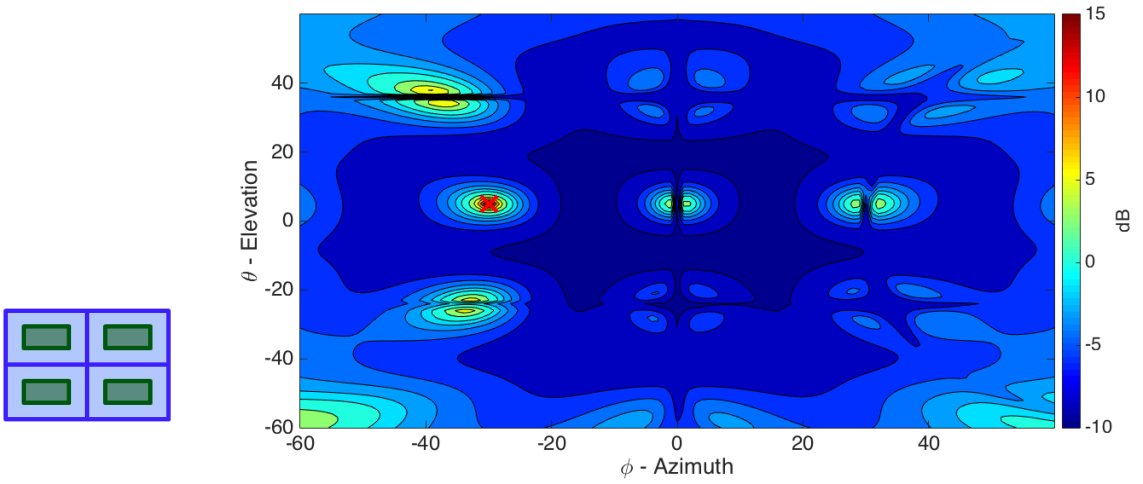

(a) SBS-ADBF (b) JNSR Output

Figure 17. JNSR output after SBS-ADBF for the antenna described in Table 5 with Jammer 1 from Table 2 present. The red X indicates jammer location.

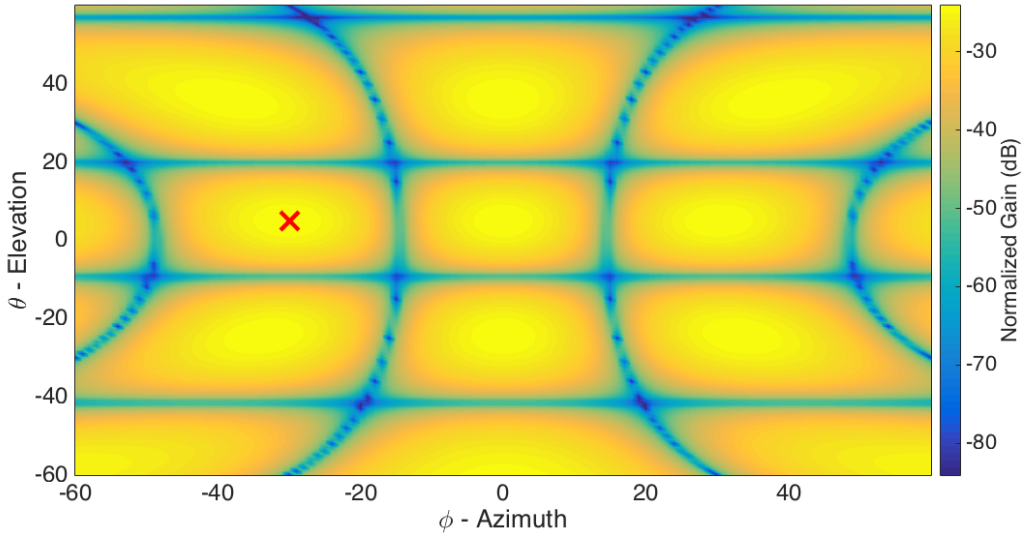

Figure 18. Digital array factor when the radar mainbeam is steered towards $(5, 0)$. The red X indicates the location of Jammer 1 from Table 2.

pattern nulls can heavily mitigate jamming effects in the array factor grating lobes. It will be shown later that synthesized subarray pattern nulls can be used to mitigate the ambiguous jammer returns intentionally.

Figure 20 shows the JNSR output when digital adaptation is being applied to the scenario containing the antenna from Table 4, and Jammers 1-4 from Table 2. The orange (*) line of Figure 28 shows the JNSR coverage statistics for these conditions, in which the digital DOF outnumber the jamming signals.

In contrast to Figure 20, Figure 21 shows the JNSR output without adaptive processing for the same scenario, which shows high degradation. This highlights the power of digital adaptation to improve performance in an otherwise inoperable environment when sufficient digital DOF are available.

Figure 22 shows the JNSR when digital adaption is used on the antenna in Table 5 and Jammers 1-4 from Table 2. Under these conditions, the yellow (x) line from Figure 28 shows the coverage statistics. The digital DOF are not sufficient to null all four jamming sources, resulting in a largely inoperable environment for the radar, as is

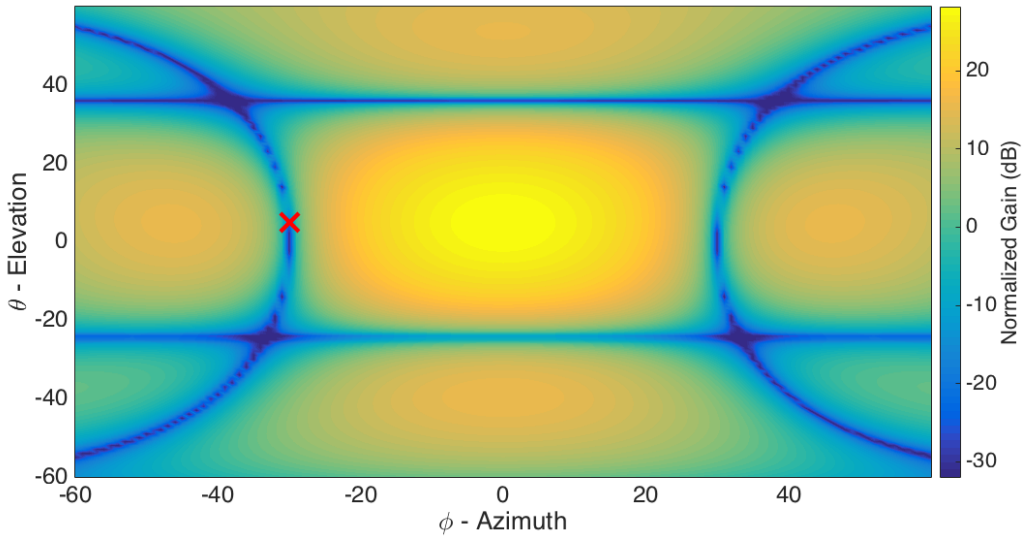

Figure 19. Subarray pattern when the radar mainbeam is steered towards $(5, 0)$. The red X indicates the location of Jammer 1 from Table 2.

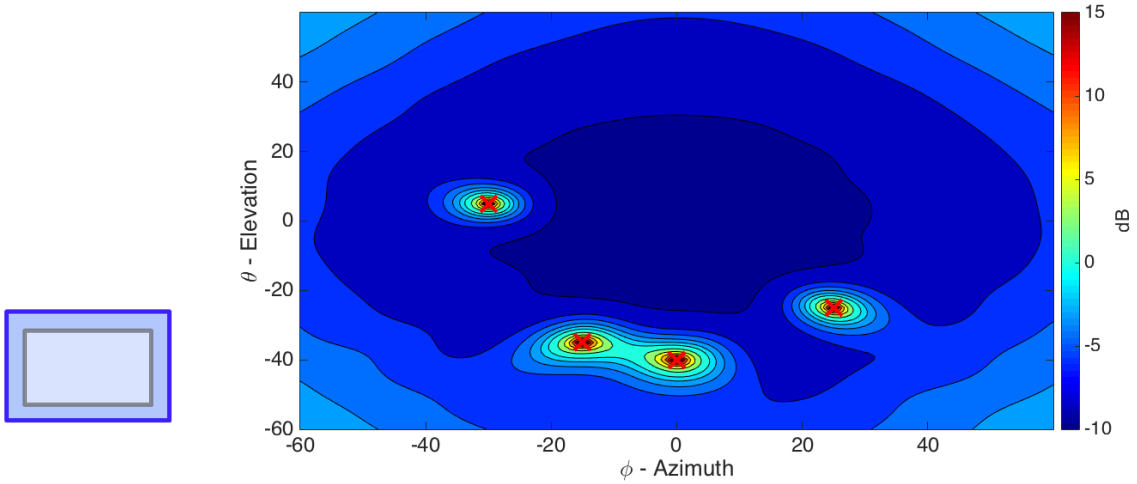

(a) ADBF (b) JNSR Output

Figure 20. JNSR output after ADBF for the antenna described in Table 4 with Jammers 1-4 from Table 2 present. The red X's indicate jammer locations.

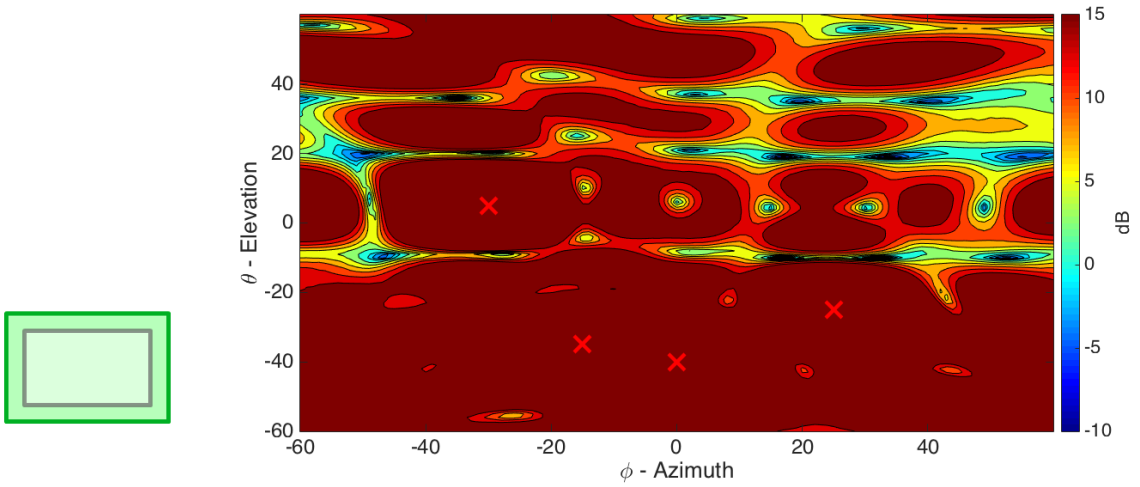

(a) DBS (b) JNSR Output

Figure 21. JNSR output with no adaptation for the antenna described in Table 4 with Jammers 1-4 from Table 2 present. The red X's indicate jammer locations.

expected. Examination of Figure 22 reveals regions of performance comparable to that of the non-subarrayed scenario (i.e. the regions surrounding $(5^o, -10^o)$, $(-5^o, 15^o)$, etc). These regions occur where one or more of the jamming signals has fallen into a quiescent null of the subarray pattern, $\mathbf{G}_{sub}$. When this occurs, the ADCs sense three or fewer jamming signals, and the digital DOF become sufficient to digitally null those jammers. However, this phenomenon does not provide consistent coverage across the desired scan area for reliable radar operation. The effects of having insufficient DOF can be observed for large areas of the field of view.

4.2 Knowledge-Aided Subarray Pattern Synthesis (KASPS) Results

Section 3.1 describes the method by which KASPS-ADBF is applied, and Section 3.2 describes a concept of operations in utilizing that method. The set of subarray weights, $\bar{\mathbf{w}}_{sub}$, may be synthesized and applied to the subarray elements in order to place spatial nulls in the subarray pattern, $\mathbf{G}_{sub}$, towards selected jamming signals.

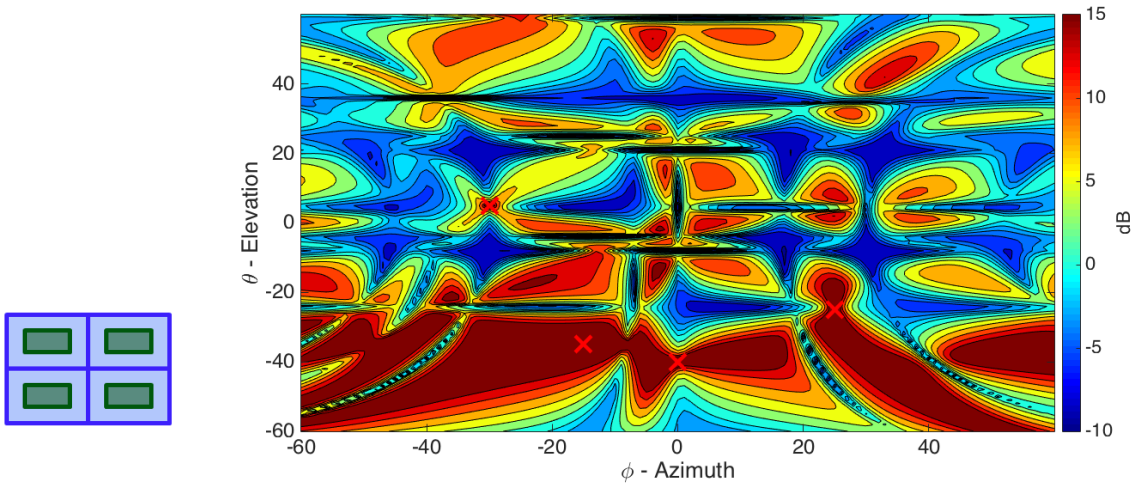

(a) SBS-ADBF (b) JNSR Output

Figure 22. JNSR output for the antenna described in Table 5 with Jammers 1-4 from Table 2 present and ADBF applied. The red X's indicate jammer locations.

For an environment which includes Jammer 1 from Table 2 and the antenna from Table 5, using this technique to cast a null in the subarray pattern toward Jammer 1 yields the JNSR output observed in Figure 23. We can initially observe that the regions of degradation arising from digital array factor grating lobe ambiguities, as seen in Figure 17, are no longer present. This suggests that KASPS can improve performance, even in situations for which $J \leq C - 1$. However, comparison of Figure 17 and Figure 23 in the region closely surrounding Jammer 1 shows degradation JNSR values. This is because the subarray null towards Jammer 1 is being placed in that direction for all look angles. Thus, when trying to look near the Jammer 1 location, the null in that direction greatly reduces the gain of the subarray pattern towards the hypothetical target. The result is a decreased signal return power, which greatly reduces the SNR, regardless of the presence of interference.

Figure 24 shows the SNR returned at each scan angle within the field of view (Equation (81)) with a subarray null consistently pointed in the direction of Jammer

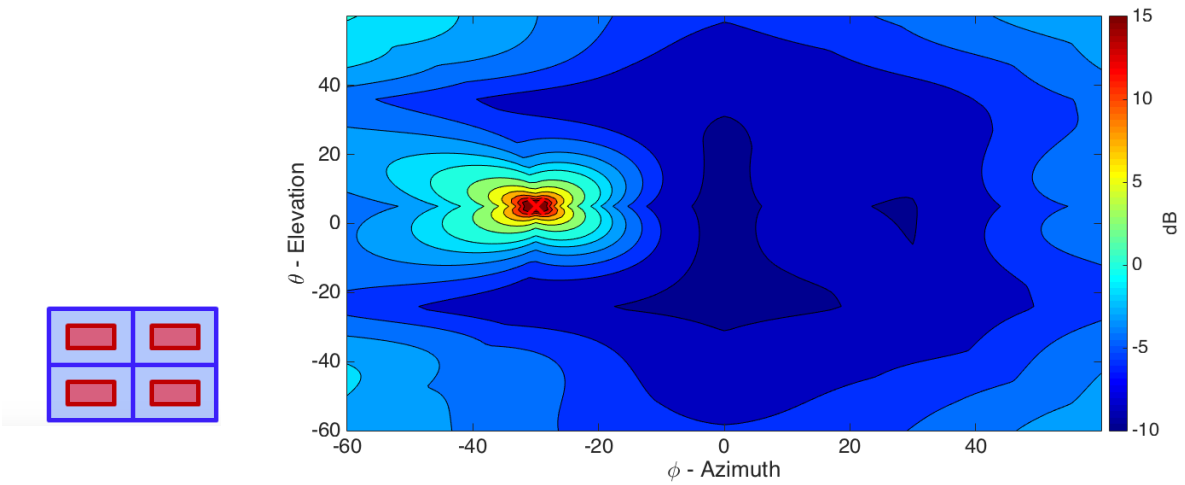

(a) KASPS-ADBF (b) JNSR Output

Figure 23. JNSR output for the antenna described in Table 5 with Jammer 1 from Table 2 present, in which Jammer 1 is being nulled with KASPS. The red X indicates the jammer location.

1. Reduction of SNR is clearly visible for look angles near the null of the pattern (note that when the look angle is exactly the same as the desired direction of the null, the null is essentially cancelled, as evidenced by the SNR return where the two exactly coincide). Thus, it is disadvantageous to cast nulls with the subarray pattern near the desired look angle. The KASPS algorithm, described in Section 3.2, tests the performance between nulling a given jammer with the subarray pattern versus nulling the jammer with the digital array factor in order to yield a "best" solution for any given look angle and jammer laydown.

Figure 25 shows the JNSR output from the environment consisting of Jammers 1-4 from Table 2 and the antenna from Table 5 when using the KASPS algorithm to selectively place subarray pattern nulls based on the concept of operations described in Section 3.2. The purple (o) line of Figure 28 shows the JNSR statistics. Figure 26 shows how many nulls were cast in the subarray pattern for each look angle in

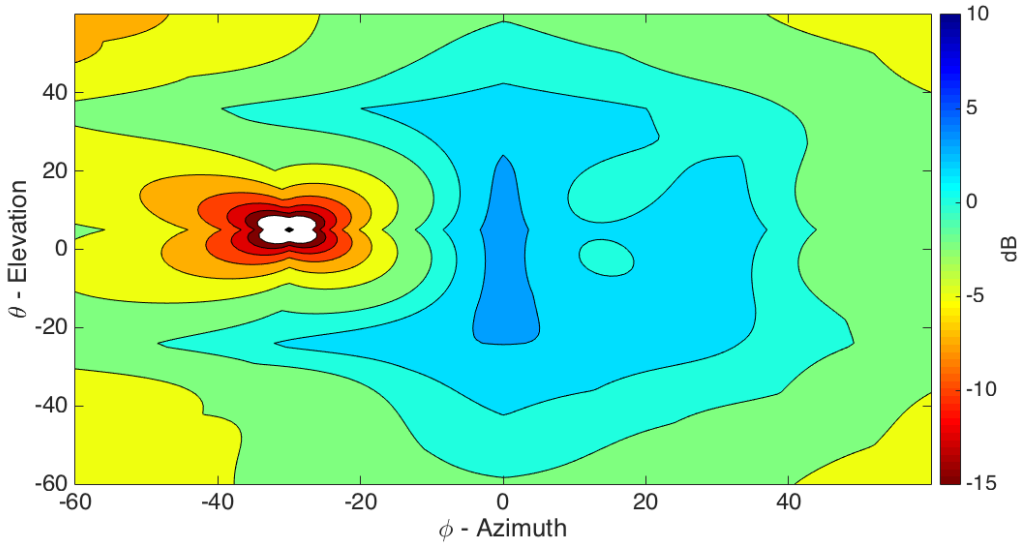

Figure 24. ξ_m, the SNR in a single subarray channel (Equation (81)), when a subarray pattern null is cast in the direction of Jammer 1 from Table 2 for the antenna described by Table 5.

the raster. There are a number of look angles for which the conventional SBS-ADBF method do in fact yield the best JNSR. Over the vast majority of the field of view, however, casting subarray pattern nulls has improved performance. Figure 27 shows the jammer nulling decision across the full raster of look angles for each individual jammer. As has been discussed, the decision to cast a given subarray null seems to be patterned off of the a function of the grating lobes of the digital array factor based on look angle and jammer location. Regions closely surrounding a given jammer are best left to be nulled using ADBF, so as to not decrease SNR. Regions in which the grating lobes of the digital array factor create ambiguous interference returns greatly improve when subarray pattern nulls are cast using the KASPS method.

Figure 28 overlays the coverage statistic curves as calculated from Figures 13, 20, 22, and Figure 25. To summarize, the "Ideal, No Jamming" curve shows the coverage statistics for the case in which there is an ADC behind every element in a noise only environment. As such, this curve represents the best possible coverage statistics, with signal degradation being only a function of the dropoff of the element

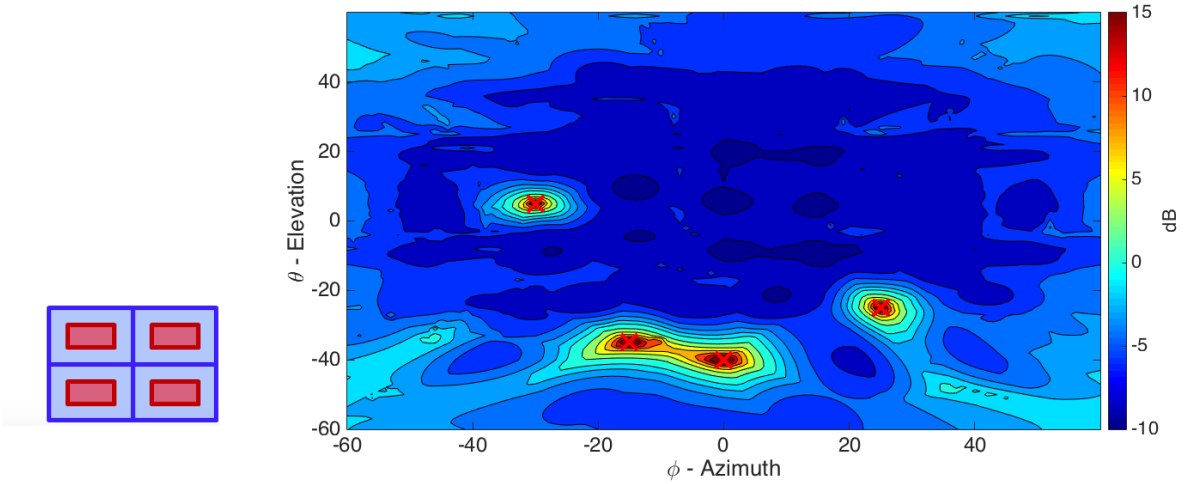

(a) KASPS-ADBF (b) JNSR Output

Figure 25. JNSR output for the antenna described in Table 5 with Jammers 1-4 from Table 2 present, in which the KASPS algorithm has determined which jamming signals are nulled by the subarray pattern and which are nulled using ADBF. The red X's indicate jammer locations.

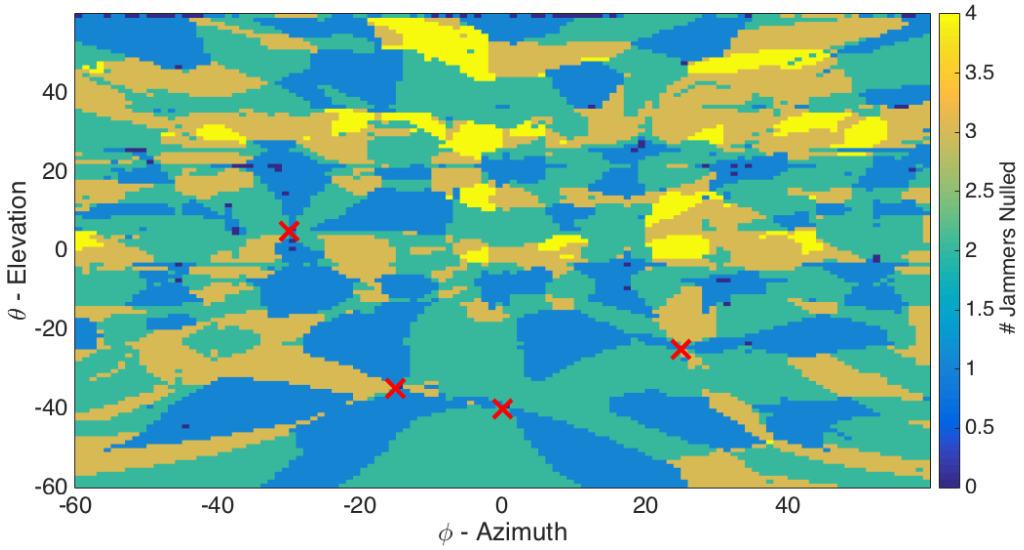

Figure 26. This environment includes Jammers 1-4 from Table 2 and the antenna from Table 5. For each look angle, the number of jammers that are nulled by the subarray pattern (as determined by the KASPS algorithm) is indicated by the colored field.

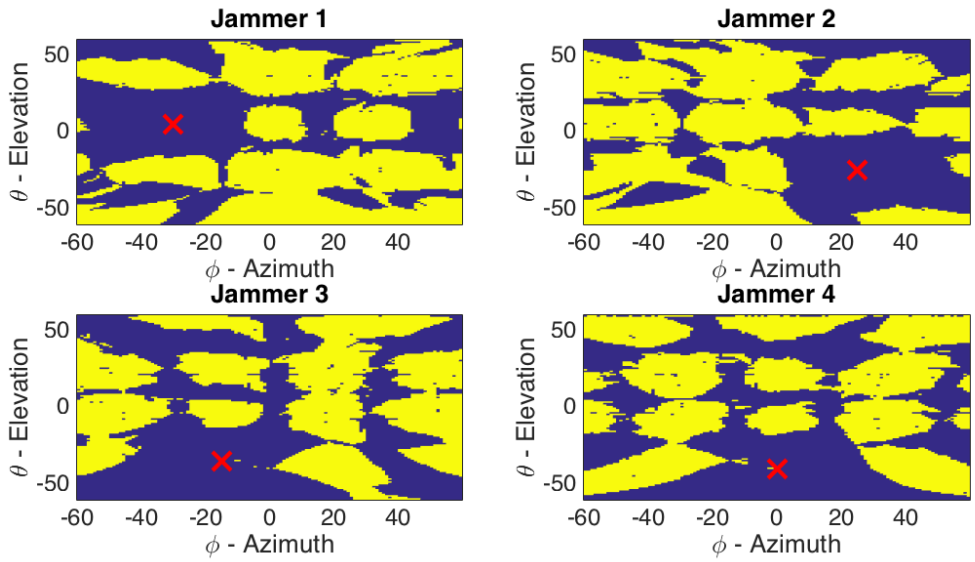

Figure 27. This environment includes Jammers 1-4 from Table 2 and the antenna from Table 5. For each look angle, a yellow field indicates that a subarray pattern null was cast in the direction of the jammer and a purple field indicates that no subarray pattern null was cast in the direction of the jammer (as determined by the KASPS algorithm).

pattern. The "Ideal ADBF" curve shows the coverage statistic for the case in which there is an ADC behind every element, Jammers 1-4 from Table 2 present, and in which ADBF is being used to suppress the interference. This curve can be seen to represent the best possible nulling solution for this particular jammer laydown. The "SBS-ADBF" curve shows the coverage statistics for the subarrayed antenna from Table 5, Jammers 1-4 from Table 2 present, and in which ADBF is being used to suppress the interference. Due to the insufficient DOF the curve shows large amounts of degradation from the ideal nulling solution. Finally, the "KASPS-ADBF" curve shows the coverage statistics for the subarrayed antenna from Table 5, Jammers 1-4 from Table 2 present, and in which the KASPS algorithm is being used in concert with ADBF to suppress the interference. It can be seen that this curve approaches the ideal nulling solution, and shows vast improvement over using ADBF alone.

To measure the improvement of one given adaptation scheme over another, the Coverage Improvement Factor (CIF) metric (Equation (84)) is used [33]. Figures 29,

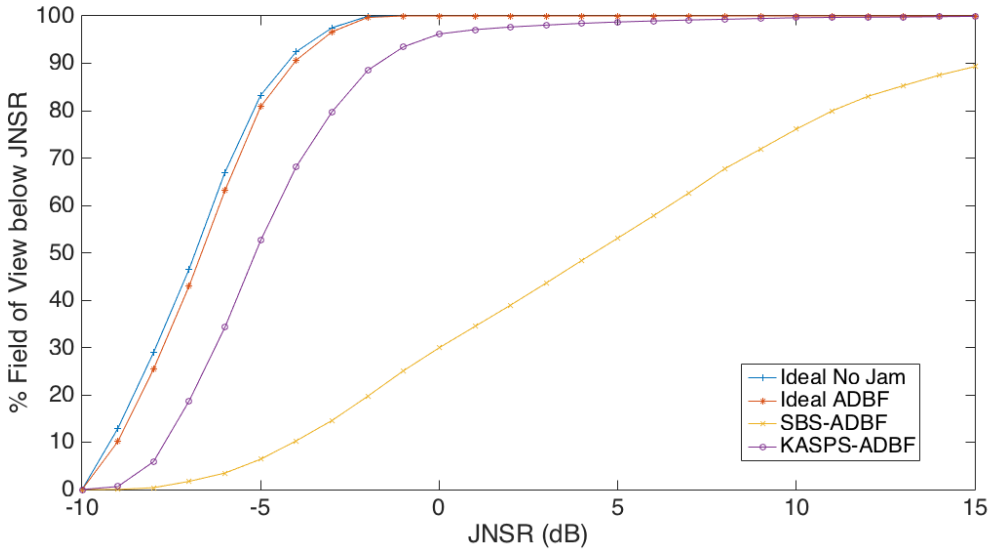

Figure 28. The percentage of the look angles for which JNSR is less than the x-axis value, comparing 4 different adaptation scenarios.

30, and 31 show the CIF across the field of view for each of the three nulling solutions as compared to the unadaptive SBS-DBS (i.e., quiescent antenna pattern) solution shown in Figure 21. Of the three nulling solutions examined, all three provide comprehensive improvement over the unadapted case. Figure 32 shows the CIF statistics for the three different interference suppression schemes. The improvement of the KASPS-ADBF method can again be observed to approach the performance of the ideal nulling solution, while the improvement afforded by the SBS-ADBF technique obviously suffers from insufficient DOF.

Up through this point, all results have been the result of a single jammer laydown (utilizing the jammers described in Table 2). In order to show the utility of the technique for any jammer laydown, Figure 33 shows the mean coverage statistics of four different nulling solutions as applied to 100 different random 4 jammer laydowns. Each jammer laydown consists of 4 jammers whose azimuth and elevation are uniformly distributed across the field of view. The error-bars in Figure 33 show the standard deviation of the data. The KASPS-ADBF technique outperforms

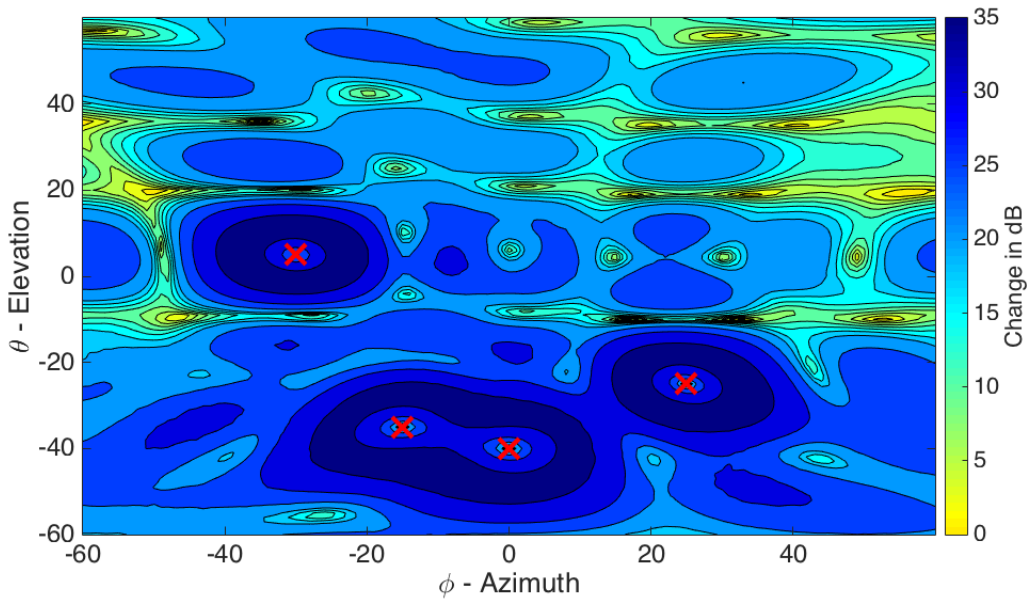

Figure 29. CIF of the ADBF solution shown in Figure 20 over the unadapted solution shown in Figure 21 for the environment consisting of Jammers 1-4 from Table 2. The red X's indicate jammer locations.

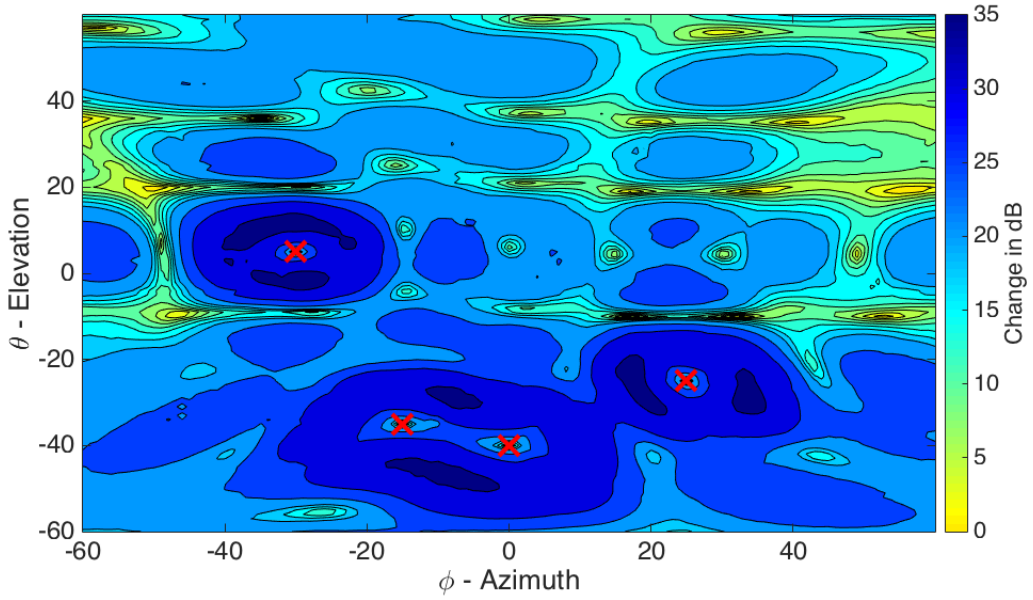

Figure 30. CIF of the KASPS-ADBF solution shown in Figure 25 over the unadapted solution shown in Figure 21 for the environment consisting of Jammers 1-4 from Table 2. The red X's indicate jammer locations.

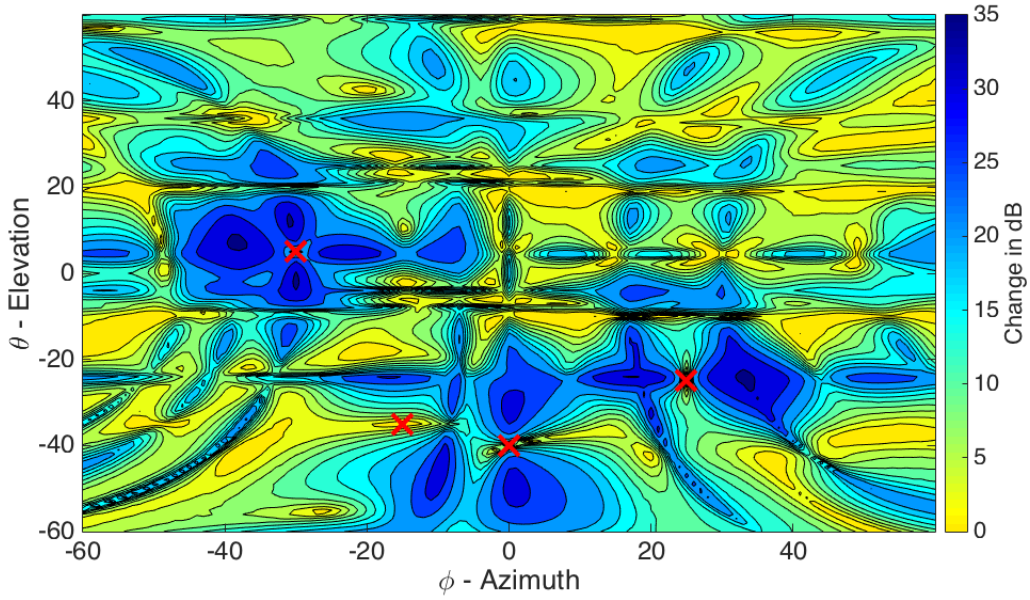

Figure 31. CIF of the SBS-ADBF solution shown in Figure 22 over the unadapted solution shown in Figure 21 for the environment consisting of Jammers 1-4 from Table 2. The red X's indicate jammer locations.

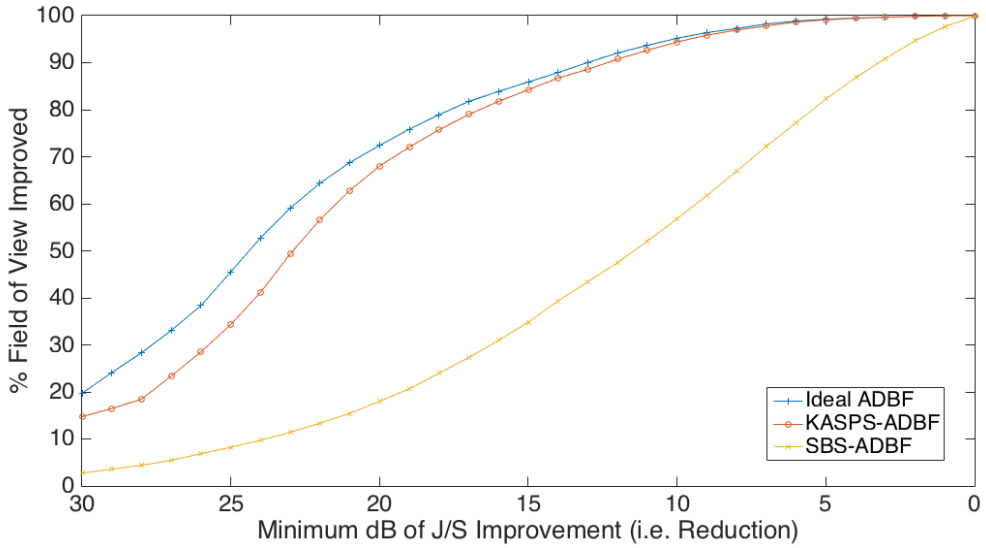

Figure 32. The percentage of the look angles for which a minimum of X dB CIF is achieved. All curves use the completely unadaptive case in Figure 21 as a reference.

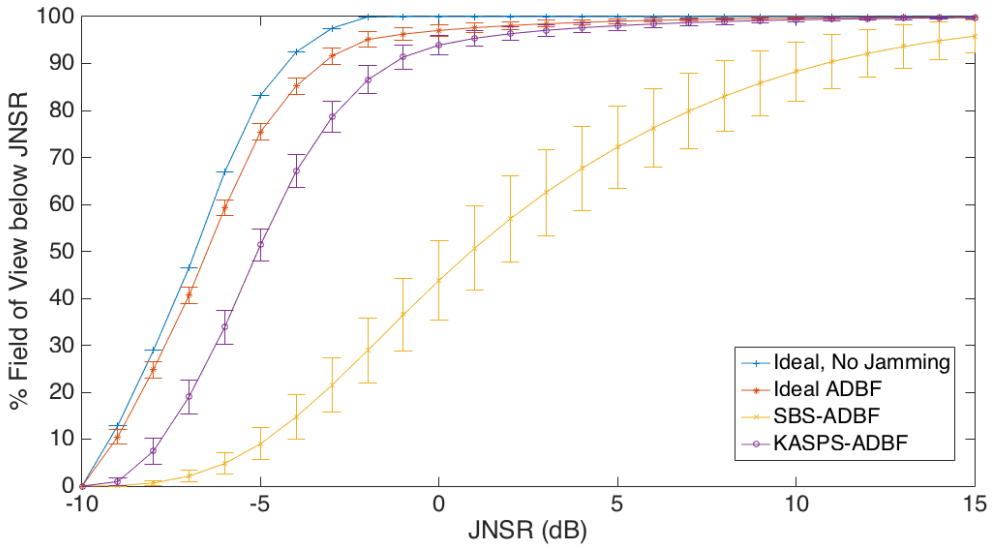

Figure 33. The percentage of the look angles for which JNSR is less than the x-axis value, comparing 4 different adaptation scenarios, averaged over 100 different random laydowns of 4 jammers in Scenario 1. The error bars indicate the standard deviation of the data.

Table 6. Antenna properties for the "idealized" case of Scenario 2.

Parameter	N_{ch}	P_{ch}	N_{sub}	P_{sub}
Value	20	20	1	1

the conventional SBS-ADBF technique by many standard deviations for most JNSR thresholds. As such, the plot shows the efficacy of the KASPS-ADBF technique against many varying jamming scenarios.

Similarly, Figure 34 shows the average CIF statistics of four different nulling solutions as applied to the same 100 different randomly created laydowns of 4 jammers from Figure 33. The error-bars show the standard deviation of the data. Figure 33 shows how the KASPS-ADBF technique can approach the ideal nulling solution, and shows the comprehensive outperformance of the KASPS-ADBF technique over the conventional SBS-ADBF technique.

Expanding the dimensionality of the array will give one a better sense of how the

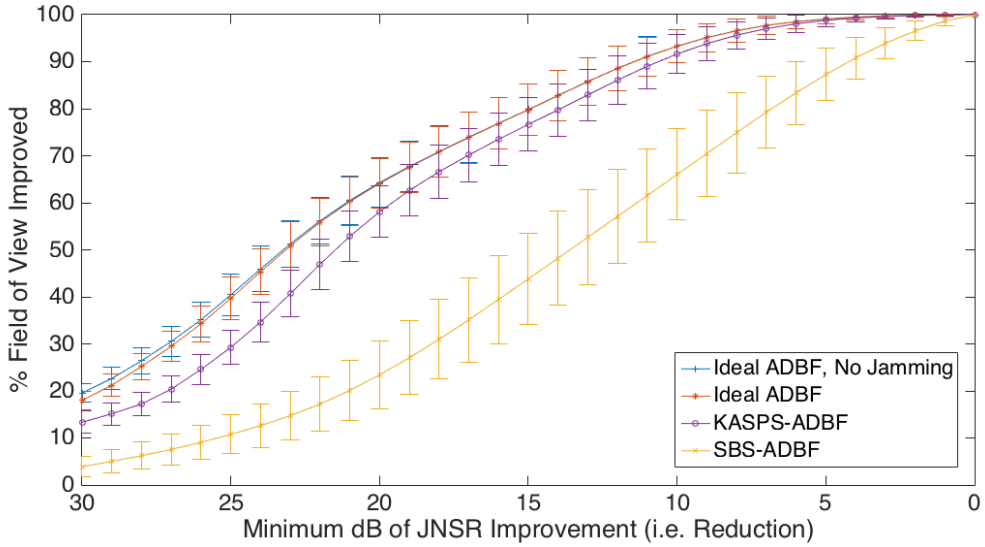

Figure 34. The percentage of the look angles for which a minimum of X dB CIF is achieved, averaged over 100 different random laydowns of 4 jammers in Scenario 1. All curves use the completely unadaptive case in Figure 21 as a reference. The error bars indicate the standard deviation of the data.

Table 7. Antenna properties for the subarrayed case of Sceanrio 2.

Parameter	N_{ch}	P_{ch}	N_{sub}	P_{sub}
Value	4	2	10	5

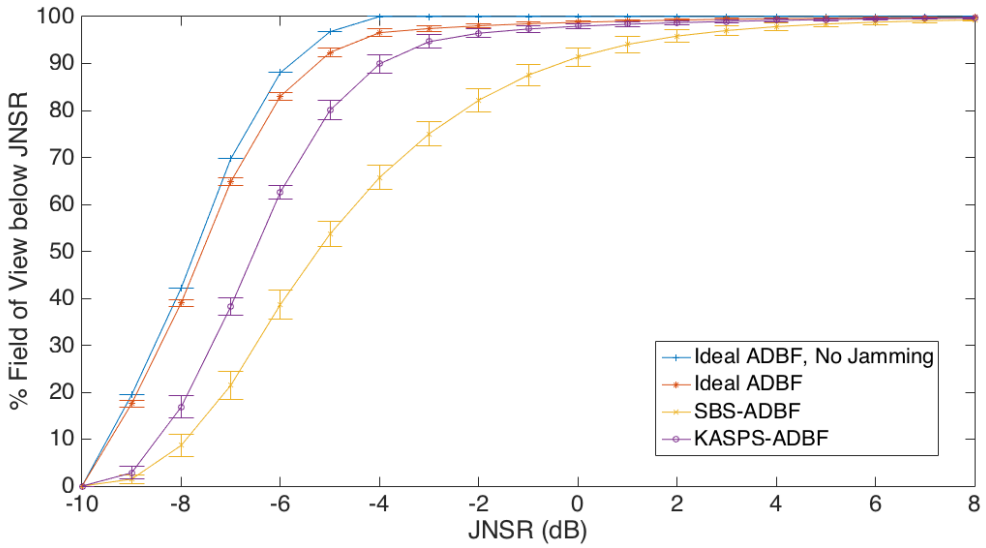

Figure 35. The percentage of the look angles for which JNSR is less than the x-axis value, comparing 4 different adaptation scenarios, averaged over 100 different random laydowns of 12 jammers in Scenario 2. The error bars indicate the standard deviation of the data.

KASPS technique would be used in real-world operations. Scenario 2 consists of the array described in Table 6 for the "ideal" case and the array described in Table 7 for the subarrayed case. Figure 35 shows the JNSR statistics of four different adaptation scenarios, averaged over 100 different random laydowns of 12 jammers. The error-bars show the standard deviation of the data. In the subarrayed case the $J = 12$ jammers eclipse the digital DOF afforded by the $C = 8$ channels. Compared to the Scenario 1 results shown in Figure 33, the SBS-ADBF solution performs admirably. This is because the pattern of a larger subarray provides more jammer attenuation from its quiescent pattern by virtue of a narrower main beamwidth. The "Ideal ADBF" curve representing the best possible adaptive solution closely approaches the "No Jamming" case. Finally, the KASPS-ADBF outperforms the SBS-ADBF solution by many standard deviations for most JNSR thresholds, though the extent of the improvement is not as drastic as in Scenario 1.

Figure 36 shows the average CIF statistics of four different nulling solutions as

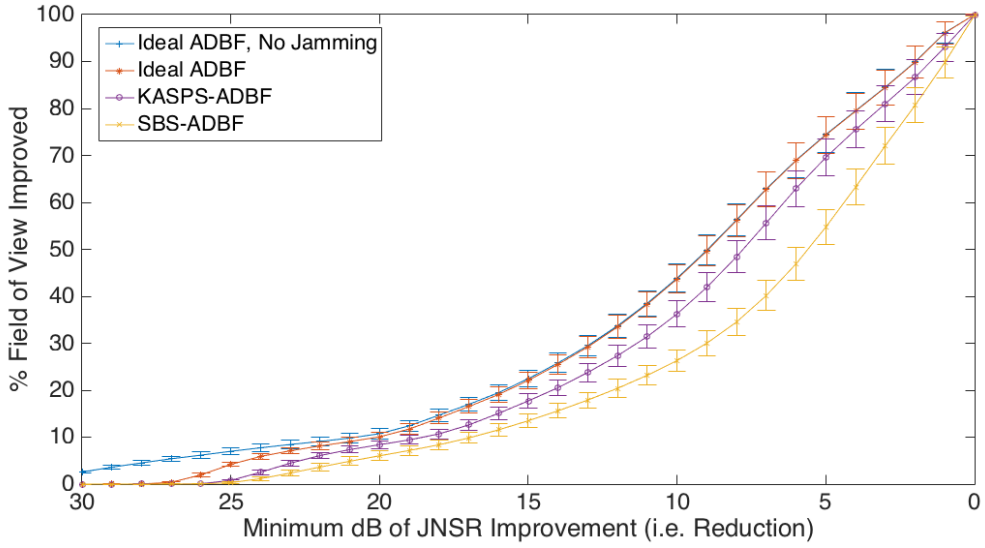

Figure 36. The percentage of the look angles for which a minimum of X dB CIF is achieved, averaged over 100 different random laydowns of 12 jammers in Scenario 2. All curves use the completely unadaptive case in Figure 21 as a reference. The error bars indicate the standard deviation of the data.

applied to the same 100 different randomly created laydowns of 12 jammers from Figure 35. The error-bars show the standard deviation of the data. Compared to the Scenario 1 CIF statistics shown in Figure 34, the overall improvement of all techniques over the unadapted case is not as drastic. This is again because the quiescent subarray pattern of a larger array provides more cancellation by virtue of a more narrow main beamwidth. Again, this plot shows how the KASPS-ADBF technique can approach the ideal nulling solution, and shows the comprehensive outperformance of the KASPS-ADBF technique over the SBS-ADBF technique.

4.3 Sensitivity Analysis Results

Section 3.3 outlines a methodology to analyze the sensitivity of the KASPS-ADBF method. The following section contains results and pertinent discussion to this analysis.

4.3.1 Angle of Arrival Estimation Error Results.

In the case that the jammer angle of arrivals (AOAs) are imperfectly estimated, performance of the KASPS algorithm will degrade as described in Section 3.3.1. Figure 37 shows the JNSR statistics for the antenna described in Table 5 with Jammer 1 from Table 2 present after KASPS has been applied using jammer properties which are known but purposefully put in error by increasing degrees in azimuth. The curves for 0^o of AOA estimation error when using KASPS-ADBF and SBS-ADBF are plotted for reference. When the AOA estimate is put in error and the KASPS algorithm is used, the performance is degraded from the accurate case. However, even when as much as 6^o of AOA estimation error is present, performance does not fall below the SBS-ADBF curve. In fact, performance will never fall below the SBS-ADBF curve, due to the logic of the KASPS algorithm. When casting a subarray pattern null no longer improves performance, the algorithm defaults to the quiescent subarray pattern. With that said, it is noteworthy that casting a subarray pattern null in error by as much as 6^o still shows interference suppression improvement over a portion of the field of view.

4.3.2 Aperture Error Results.

When the antenna manifold is uncalibrated, unknown, or subject to other means of aperture error, performance of the KASPS algorithm will degrade as described in Section 3.3.2.

Figure 38 shows JNSR statistics from using the KASPS-ADBF method for increasing amounts of aperture error. For instance, the "2%" line shows the result of allowing the true element locations stored in $\mathbf{D}$ to deviate in value by as much as 2% of the element spacing from the estimated element locations stored in $\hat{\mathbf{D}}$. For 2% aperture error, only slight degradation of the KASPS-ADBF method occurs. As

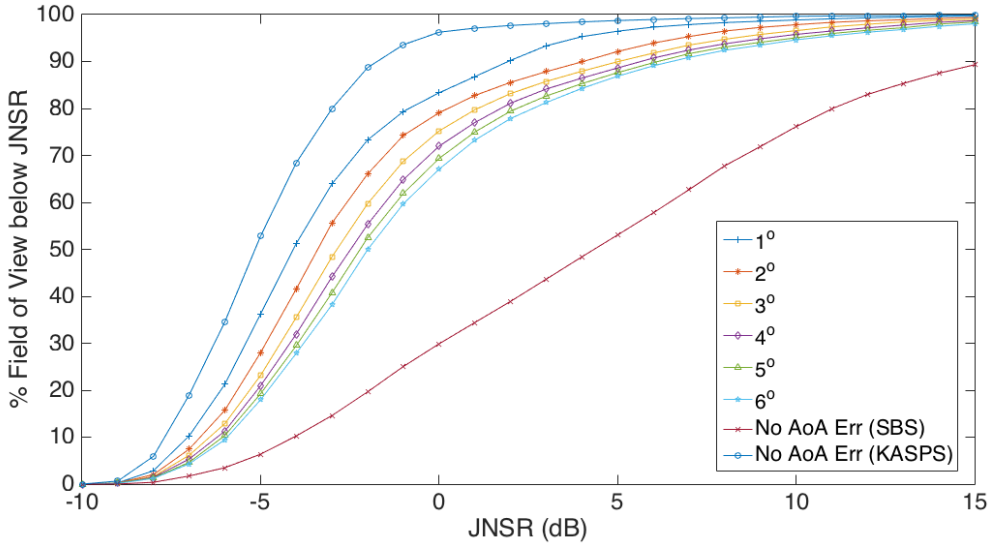

Figure 37. An analysis on the effect of AOA misestimation in the environment which includes the antenna from Table 5 and Jammers 1-4 from Table 2. The plot displays the resultant coverage statistics as the degree of azimuthal AOA estimation error is increased.

the extent of the error increases, performance further degrades. The 33.3% error line shows degradation of performance for a portion of the field of view that falls below the performance of the un-erred SBS-ADBF response. These findings reinforce the necessity of a known and calibrated manifold to experience the full performance benefits of the KASPS technique.

4.3.3 Weight Quantization Results.

Section 3.3.3 describes the quantized nature by which real weights are applied in hardware to the subarray elements. This section examines the effects of subarray weight quantization on the KASPS-ADBF method. Phase and gain bit levels, and the dynamic range of the quantized amplifier are examined indepently. For the sake of continuity, the study is performed for the environment using the antenna from Table 5 and Jammers 1-4 from Table 2.

To examine the effect of phase quantization on subarray weights, the number of

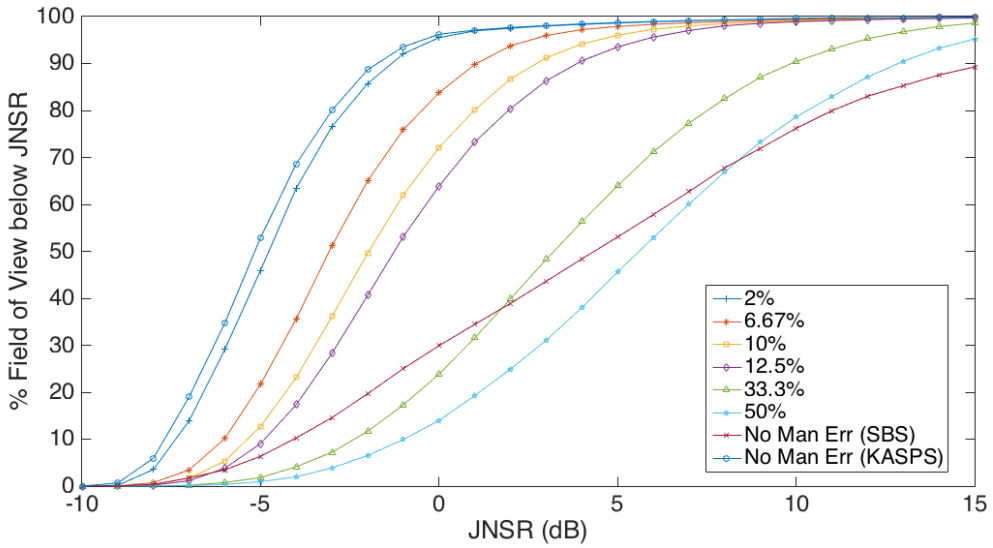

Figure 38. An analysis on the effect of aperture error on Scenario 1 including Jammers 1-4 from Table 2. The plot displays the resultant coverage statistics as the amount of aperture mismatch error is increased.

gain bits and the gain dynamic range are held at suitably high levels (12 bits and 4 dB respectively) while the number of phase bits is increased. At each step, the JNSR statistics are calculated using the given quantization level to modify the phase of the weights, $\bar{\mathbf{w}}_{sub}$, as calculated from Equation (79). Figure 39 shows the results of the study, where it can be observed that the performance of the non-quantized case (computing using 64 bits) can be closely approached with 8 phase bits. With 9 phase bits no further appreciable gains are realized. As the number of phase bits decreases, the steering of the subarray becomes less accurate (in pointing the mainbeam and placing nulls) and concurrently performance is seen to degrade.

To examine the effect of gain quantization on subarray weights, the number of phase bits and the gain dynamic range are held at suitably high levels (12 bits and 4 dB respectively) while the number of gain bits is increased. At each step, the JNSR statistics are calculated using the given quantization level to modify the gain of the weights, $\bar{\mathbf{w}}_{sub}$, as calculated from Equation (79). Figure 40 shows the results of the study, where it can be observed that the performance of the non-quantized

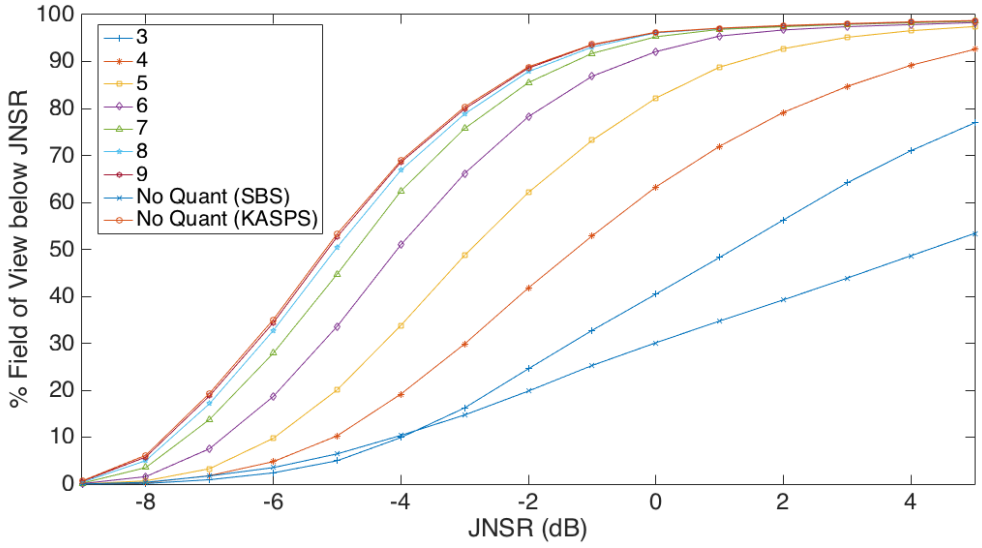

Figure 39. An analysis on the effect of phase quantization on subarray weights in the environment which includes the antenna from Table 5 and Jammers 1-4 from Table 2. The plot displays the resultant coverage statistics as the number of phase bits in the subarray element weights are increased. Non-quantized scenarios showing the KASPS-ADBF and SBS-ADBF statistics are shown for reference.

case (computing using 64 bits) can be closely approached with 6 gain bits. With 7 gain bits no further appreciable improvement is realized. As the number of gain bits decreases the subarray mainbeam becomes less accurately shaped (less gain in the look direction, more gain in the nulls) and concurrently performance is seen to degrade.

To examine the effect of dynamic range on subarray weights, the number of phase bits and gain bits are held at suitably high levels (12 bits each) while the extent of the dynamic range is increased in 1 dB intervals. At each step, the JNSR statistics are calculated using the given quantization dynamic range to modify the gain of the weights, $\bar{\mathbf{w}}_{sub}$, as calculated from Equation (79).. Figure 41 shows the results of the study, where it can be observed that the performance of the non-quantized case (i.e. ∞ dB of dynamic range) can be closely approached with 3 dB of dynamic range, after which no appreciable gains are realized. As with decreasing the number of gain bits, when the dynamic range decreases the subarray mainbeam becomes less accurately

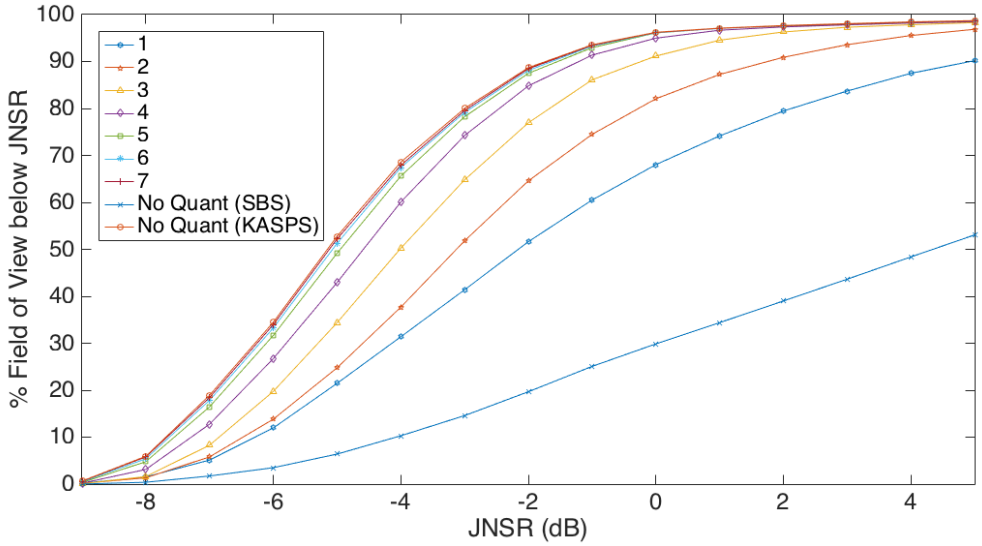

Figure 40. An analysis on the effect of gain quantization on subarray weights in the environment which includes the antenna from Table 5 and Jammers 1-4 from Table 2. The plot displays the resultant coverage statistics as the number of gain bits in the subarray element weights are increased. Non-quantized scenarios showing the KASPS-ADBF and SBS-ADBF statistics are shown for reference.

shaped (less gain in the look direction, more gain in the nulls) and concurrently performance degrades.

Across all three sets of results as shown in Figures 39, 40, and 41, it can be seen that the KASPS-ADBF method provides superior coverage over the SBS-ADBF case for situations in which the subarray weights have been quantized. Even at low quantization levels (as low as 3 phase bits, 1 gain bit, or 0 dB of dynamic range) superior interference suppression can be achieved using KASPS-ADBF.

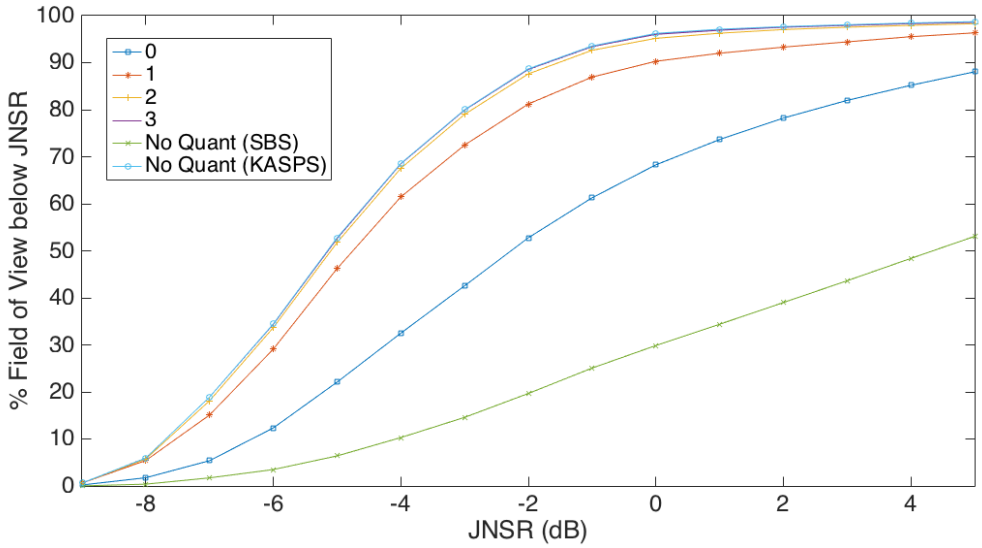

Figure 41. An analysis on the effect of gain dynamic range on subarray weights in the environment which includes the antenna from Table 5 and Jammers 1-4 from Table 2. The plot displays the resultant coverage statistics as the amount of dynamic range in the subarray element weights are increased. Non-quantized scenarios showing the KASPS-ADBF and SBS-ADBF statistics are shown for reference.

V. Conclusion

This research demonstrates techniques by which untapped spatial degrees of freedom (DOF) inherent to the subarrays of a phased array antenna may be used to mitigate spatially localised interference signals. Mitigation of interference can reduce the dynamic range requirements of the receive chain in order to avoid saturation, or preserve digital DOF for adaptive digital nulling in the processor. This thesis has shown how a set of subarray weights can be synthesized and applied to place subarray pattern nulls on any combination of jammers present in the scene.

The ability to synthesize subarray weights depends on knowledge of the jammers' angle of arrivals (AOAs) and powers as well as a known and calibrated antenna manifold. Placing nulls near the desired look direction results in a degradation of Signal-to-Noise Ratio (SNR) that cannot be recovered by digital adaptive processing. Thus, it is typically not advantageous to null jammers in the vicinity of the desired look direction with real subarray pattern nulls. However, using subarray pattern adaptation to null strong jamming signals some beamwidths away from the radar mainbeam does not significantly degrade SNR, and preserves digital DOF for nulling jamming signals near the mainbeam. Using this philosophy, subarray pattern synthesis was shown to effectively supplement digital adaptation to significantly improve performance. The implementation tradeoffs between nulling via the subarray pattern versus nulling via Adaptive Digital Beamforming (ADBF) were analyzed and used in divising a concept of operations for applying the Knowledge-Aided Subarray Pattern Synthesis (KASPS)-ADBF method across jamming signals.

The practical limitations of beamforming are an important factor in analyzing the KASPS technique. In general, physically adapted beams are inferior to ADBF in nulling interference for many reasons, including the introduction of quantization noise and the limits placed on dynamic range. The effectiveness of the KASPS technique

degrades when there has been error in the estimation of the jammer AOA, or when there is error in the knowledge of the antenna manifold. These errors result in inaccurate null placement. However, even under degraded conditions, the KASPS-ADBF technique still yields improved interference suppression capability over the conventional Subarray Beam Steering (SBS)-ADBF method. The concept of operations for the KASPS technique is designed to preclude potential performance degradation. Quantization of the subarray weights can also lead to inaccurate null placement, or sub-optimal null depths and mainbeam gains. However, improvement over the unquantized SBS-ADBF method can still be observed for various bit levels, and with at least 9 phase bits, 7 gain bits, and 3 dB of dynamic range, any deleterious quantization effects become inconsequential.

5.1 Contributions

This research set out to make three contributions to the field of Electronic Protection (EP) for phased array systems. The first was to offer a proof of concept of the potential benefits of the KASPS-ADBF method. This was accomplished through software simulations showing improved performance using the KASPS-ADBF method over conventional and unadapted methods. The second contribution is the concept of operations for the use of the KASPS-ADBF method. An analysis of the effects of placing subarray nulls given a desired look angle and jammer laydown is presented, resulting in an algorithmic implementation of the method. The final contribution was to test the sensitivty of the KASPS-ADBF method. To this end, an initial sensitivity study examining AOA estimation error, aperture error, and quantization show the efficacy of the KASPS-ADBF method under these practical conditions.

5.2 Future Work

To more accurately examine the potential of this technique to improve the performance of existing radar systems, a number of topics are reccomended for further study. Among them would be to repeat this analysis while accounting for mutual coupling, phase squint, aperture errors, and other random sources of error. The analysis should also be expanded to include clutter to investigate how subarray DOF may be used synergistically with digital DOF for clutter and jammer suppression. A litany of spectral estimation algorithms from the many techniques available in literature could be used to accurately estimate jammer AOA and thus improve the effectiveness of the KASPS-ADBF method. Additionally, the KASPS concept of operations should be analyzed for computational complexity and optimized for performance and processing demands. While the development here invokes a narrowband assumption, the KASPS technique should be extended for use in wideband systems. Finally, a proof-of-concept test on real hardware utilizing a known manifold should be conducted to prove real-world viability.

5.3 Final Thoughts

In an era of ever increasing Electronic Attack, it is increasingly important to provide means of EP at an affordable cost. Adaptive subarray pattern synthesis offers some of the EP benefits of more digitized channels without their cost. The existing DOF inherent in phased array subarrays can be employed via modest upgrades to existing radars. While digital adaptation does not require knowledge of the manifold, spatial DOF in the subarray are left dormant when ADBF is relied on as the sole means of interference suppression. KASPS will provide the radar designer with a powerful tool in preserving the maximum operable field of view when confronted by a highly populated hostile jamming environment.

Appendices

Appendix A. Jammer Parameter Estimation

The Knowledge-Aided Subarray Pattern Synthesis (KASPS)-Adaptive Digital Beamforming (ADBF) method requires prior knowledge of the angle of arrivals (AOAs) of the jamming signals, and the powers of the jammers at the array face. These parameters could potentially be known from external sources, such as intelligence reports or external sensor packages. However, in the case that the jammer parameters are not known the radar system may be able to estimate them using an algorithmic technique that combines a raster scan of the field of view with spectral estimation techniques to find more jammers than the adaptive digital degrees of freedom (DOF) would allow via conventional spectral estimation techniques. The method proposed in this appendix is not postulated as an optimum solution, but rather presented to suggest that jammer parameter estimation using a phased array is possible in circumstances when the number of jammers is greater than the amount of digital DOF.

A.1 Spectral Estimation

Interference source AOAs can be found using spectral estimation techniques. While a vast number of spectral estimation techniques are available in literature to choose from, the method proposed here utilizes the Minimum Variance (MV) method [29]. MV estimators are capable of providing high resolution AOA estimates. The MV method is also referred to as Capon's method [42]. The method operates by leveraging the signal eigenvalues of the jamming covariance matrix. Doing so relies on the presence of white noise (so as to ensure a non-singular covariance matrix), and also limits the number of signals able to be resolved to $C-1$ [41]. A summary of the MV technique is given here, and can be studied in greater detail in [29].

The output power from MV estimation is

$$P_{MV,ch}(\theta,\phi) = \left(\mathbf{v}_{ch}^{H}(\theta,\phi)\hat{\mathbf{R}}_{ch}^{-1}\mathbf{v}_{ch}(\theta,\phi)\right)^{-1}. \tag{a.94}$$

in which $\mathbf{v}_{ch}(\theta,\phi)$ is a steering vector (as defined in Equation (69)), and $\hat{\mathbf{R}}_{ch}$ is the estimated covariance matrix as observed through the digitized channels (as defined in (60)). Where there is orthogonality between the steering vector, $\mathbf{v}_{ch}(\theta,\phi)$, and the estimated covariance matrix, $\hat{\mathbf{R}}_{ch}$, there results in a steep negative peak. These minimums are inverted yielding maximums in the power spectrum at the locations of the interfering signals [29]. The nature of orthogonality results in sharp peaks yielding high resolution estimates with low susceptibility to corruption by noise. When performing MV estimation with a subarrayed antenna, array factor grating lobes (described in Section 2.1.1) can cause ambiguous estimates in the spectrum.

Because MV estimation uses orthogonality to find minimums, the amplitude information yielded from it does not provide realistic power measurements. A power spectrum can also be estimated using the Signal Match (SM) filter. Signal matching is provides low resolution in AOA estimation, but yields accurate power estimates. The SM power spectrum is given by

$$P_{SM,ch}(\theta,\phi) = \frac{\mathbf{v}_{ch}^{H}(\theta,\phi)\hat{\mathbf{R}}_{ch}\mathbf{v}_{ch}(\theta,\phi)}{\mathbf{v}_{ch}^{H}(\theta,\phi)\mathbf{v}_{ch}(\theta,\phi)}. \tag{a.95}$$

In determining the power output, the $\mathbf{v}_{ch}(\theta,\phi)$ steering vector may be colinear with components in $\hat{\mathbf{R}}_{ch}$, yielding maximums in the power spectrum. In a noise and interference only environment, these maximums represent jamming returns.

MV estimation is useful for AOA estimation, while signal matching is well suited for power estimation.

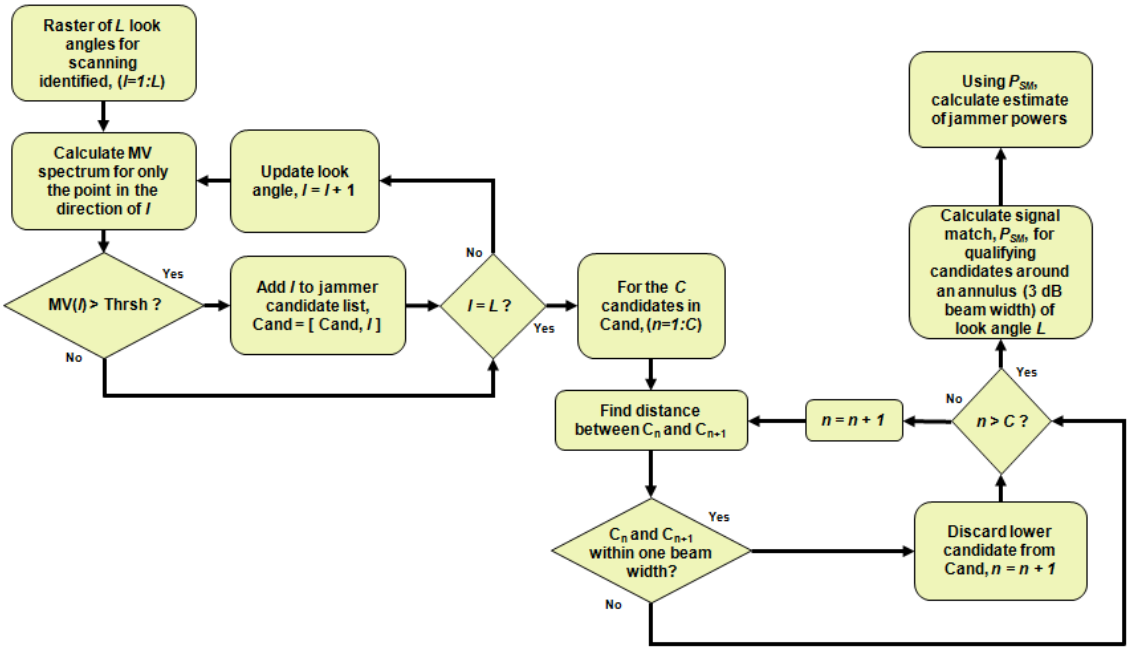

Figure A-42. Flow diagram demonstrating how jammer parameters are estimated using spectral estimation techniques.

A.2 Jammer Parameter Estimation Method

Spectral estimation techniques, specifically the MV method as described in Equation (a.94) (described in Section A.1) can be used to ascertain jammer AOAs in environments where the number of jammers is less than the digital DOF of the array. When the number of jammers exceeds the digital DOF of the array conventional spectral estimation methods fail to produce meaningful outputs. Thus, without outside knowledge of the jammer parameters (i.e. intelligence, external sensor packages, etc), an algorithmic method to ascertain jammer locations is necessary in order to use the KASPS-ADBF method to null select interference signals with the subarray pattern. One such algorithmic solution is outlined by the flow diagram in Figure A-42 and detailed in this section.

In pursuit of ascertaining the jammer locations, the radar will enter a scanning mode, in which the beam is electronically steered through the raster of look angles

across elevation and azimuth. For each look angle a covariance matrix, $\hat{\mathbf{R}}_{ch}$, will be estimated. The MV operation is then performed for only the look angle in question (as opposed to calculating the full spectrum) as given by

$$\hat{P}_{MV,ch}(\theta_0, \phi_0) = \left(\mathbf{v}_{ch}^H(\theta_0, \phi_0) \hat{\mathbf{R}}_{ch}^{-1} \mathbf{v}_{ch}(\theta_0, \phi_0) \right)^{-1}. \tag{a.96}$$

This operation is performed for every look angle in the raster. By scanning the beam to create the spectrum as opposed to calculating the spectrum from a single look angle, the subarray beam naturally "knocks down" the received power of jammers which are far from the look angle in question. Similarly, as the beam is scanned, jammers will fall completely into natural nulls of the subarray pattern at certain look angles. This also means that when jammers fall into a sidelobe for a given look angle, these jammers will increase the impinging signal, possibly leading to false jammer detections at the said look angle. However, mainbeam gain will always be strongest in the direction of the look angle in question, and thus any jammer directly in the boresight of the radar for a given look angle will feature prominently in the final spectrum regardless of spurious returns.

Once the spectrum has been calculated, the radar processor must make a decision on whether jammers have been detected. The relative maxima are identified and compared against a threshold. Values under the threshhold are considered to be results of ambiguities due to the array factor (examined in greater detail in Section 4.2) and those candidates are discarded. The remaining candidates are compared to each other via location. If any two candidates are within a subarray mainbeam distance apart from each other, only the more powerful candidate is retained (as the other maxima is likely from jammers entering and exiting sidelobes as the radar is scanned). Any candidates still remaining register as detected jammers and their locations in azimuth and elevation are stored in the processor's memory.

In order to synthesize a clairvoyant subarray covariance matrix by which analog weights, $\bar{\mathbf{w}}_{sub}$ can be calculated, the power of the jammer impingent upon the array also needs to be known. To measure the power, the SM method is used. For the found locations of the jammers, the SM power spectrum is used (as in Equation (a.95)). In order to get an accurate representation of the power present at the array face, one must calculate the SM spectrum for an annulus of angles around the found location, yielding an estimate of the b^{th} jammer's power, $P_{j,ch,b}$. Appropriate sizing of this annulus may have to be tuned for different array configurations. The power of the jammer as received by the array is given in Equation (49). However, the subarray pattern will change as the beam is steered, so in order to be able to synthesize an $\bar{\mathbf{R}}_{sub}$ for any look angle, the effects of the array must be backed out in order to estimate the power just outside (as opposed to within) the array face. In the case of the b^{th} jammer this is given by

$$\frac{S_{j,b}}{R_{j,b}^2} = \frac{P_{j,ch,b} L_s}{G_{sub}(\theta_{j,b}, \phi_{j,b})}. \tag{a.97}$$

With $\frac{S_{j,b}}{R_{j,b}^2}$ known, the Jammer to Noise Ratio (JNR) for any given look angle and accounting for any combination of jammers can be calculated, enabling $\bar{\mathbf{w}}_{sub}$ to be appropriately synthesized (Equation (79)).

The resolution of this technique in determing AOA is limited by the resolution of the raster of scan angles tested. The ability of the algorithm to resolve two seperate jammers, however, is limited by the subarray mainbeam width. Any two or more jammers which are within an angular distance of each other less than the subarray mainbeam width will be unresolved (i.e., appear as one jammer with power contributions from both). This technique is not limited by the number of jamming signals in the environment; there is no limit on the number of jammers able to be found. However, more jammers in the environment will lead to "dirtier" spectral estimates (enough jammer power in sidelobes can cause misrepresentative data), leading to

inaccurate location and power estimates.

A.3 Jammer Parameter Estimation Results

The results shown in Section 4.2 rely on the ability to precisely know the AOA of and the powers of the jamming signals at the radar array face. Section A.2 describes the Jammer Parameter Estimation (JPE) algorithm; a technique by which these parameters may be ascertained. Results of this algorithm derived from Scenario 1 (described in Chapter IV) are presented in this section.

Figure A-43 shows the MV spectrum, $\hat{\mathbf{P}}_{MV,ch}$ (Equation a.94), as estimated from the JPE algorithm in the environment including the antenna from Table 5 and Jammers 1-4 from Table 2. The algorithm scanned from -60^o to 60^o in azimuth and elevation in 1^o increments. Table 8 details the estimated jammer parameters returned by the algorithm for this environment. Jammer 1 is the most spatially isolated of the jammers. Because of this it can be observed that Jammer 1 has the most steeply defined peak, as all other jammers have been knocked down substantially by the subarray pattern when the MV is taken for look angles in the vicinity of Jammer 1. Jammer 3 and Jammer 4 both align closely in the azimuthal direction. As such, smearing of the spectrum can be observed in the azimuthal direction in the vicinity of both Jammer 3 and Jammer 4. The jammers in this environment are spatially disparate enough that all can be accurately resolved by the algorithm, given the subarray beamwidth of the antenna. While Table 8 reports no error for the elevation and azimuth estimates, all jammers were placed directly on the raster grid that was searched. Practically some error should be expected. The error in the power estimate is always positive due to some amount of power leaking in through the subarray pattern sidelobes from jammers other than the one whose power is being estimated.

Figure A-44 shows the Jamming and Noise-to-Signal Ratio (JNSR) output after

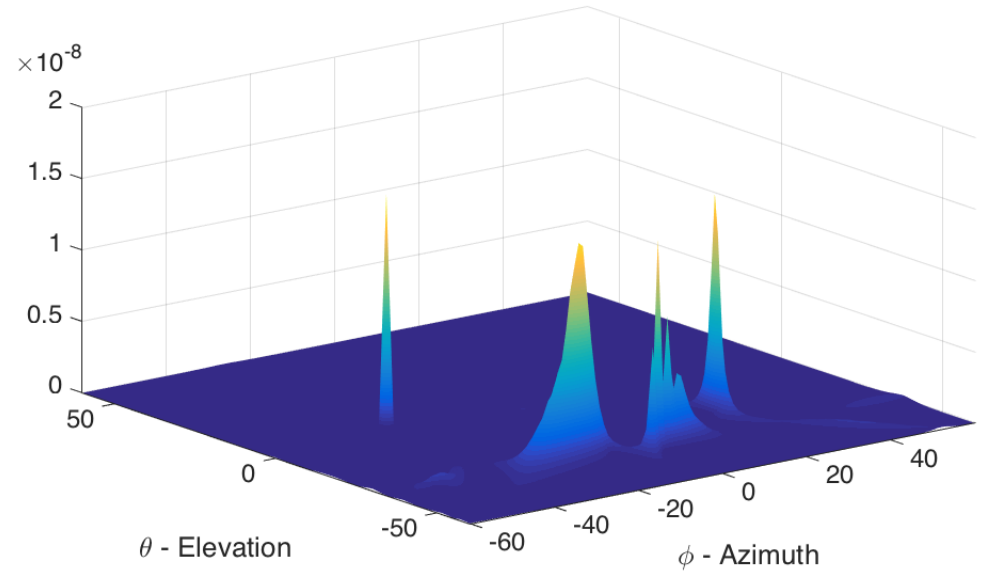

(a) Angled View

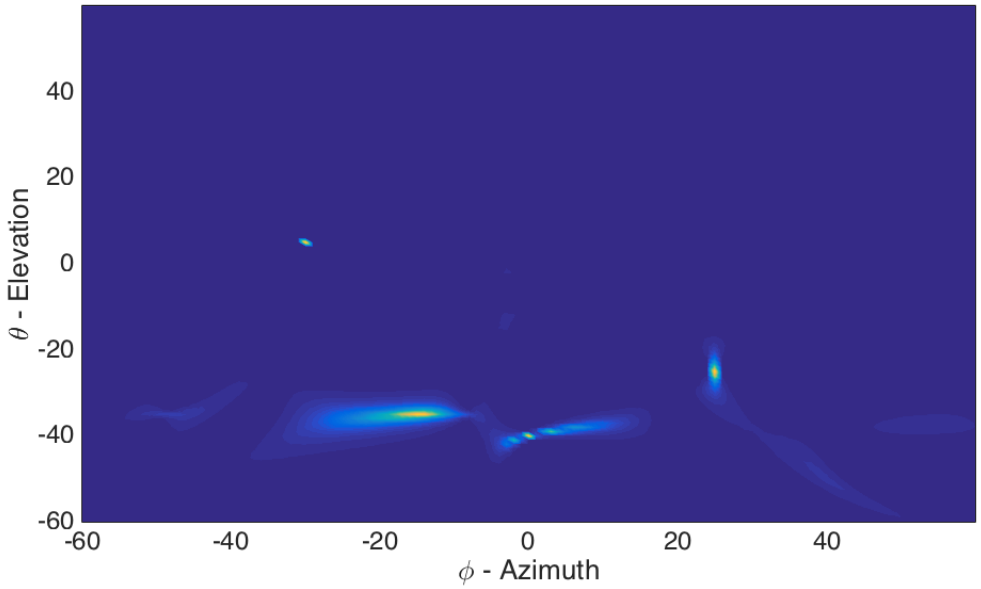

(b) Birds Eye View

Figure A-43. The minimum variance spectrum, $\hat{\mathbf{P}}_{MV,ch}$, as estimated from the JPE algorithm in the environment including the antenna from Table 5 and Jammers 1-4 from Table 2 shown from two vantage points. The spectrum values (z-axis) are purely relative.

Table 8. Jammer parameters ascertained by the JPE algorithm, as described in Section A.2, in the environment containing the antenna from Table 5 and Jammers 1-4 from Table 2.

Jam. Det.	ϕ (^{o})	θ (^{o})	$\frac{S_j}{R_j^2}$ (W)	ϕ Error (^{o})	θ Error (^{o})	$\frac{S_j}{R_j^2}$ Error (W)
1	-30	5	1.18 x 10^{-8}	0	0	+1.8 x 10^{-9}
2	25	-25	1.09 x 10^{-8}	0	0	+0.9 x 10^{-9}
3	-15	-35	1.28 x 10^{-8}	0	0	+2.8 x 10^{-9}
4	0	-40	1.43 x 10^{-8}	0	0	+4.3 x 10^{-9}

KASPS-ADBF, as applied using the jammer parameters found by the jammer location algorithm shown in Table 8. Examining the coverage statistics in Figure A-45 show that the results from the estimated parameters are equivalent to the case in which clairvoyantly known parameters were assumed (Figure 25).

Figure A-46 shows the MV spectrum, $\hat{\mathbf{P}}_{MV,ch}$, as estimated from the JPE algorithm in the environment including the antenna from Table 5 and Jammers 1-8 from Table 2. Similarly, Table 9 details the estimated jammer parameters returned by the algorithm for this environment. Foremost, it stands to note that only seven jammers have been detected. Jammer 1 and Jammer 8 are within a subarray beamwidth of each other (in this case, they are seperated by 10^o in elevation). The spectrum shows that a peak exists in between the two at $(-30^o, 10^o)$, which the algorithm is unable to distinguish from a single, more powerful jammer. Again the other six jammers in Table 9 report no error for the elevation and azimuth estimates, but all jammers were placed directly on the raster grid that was searched. Practically some error should be expected. All other jammers are spatially disparate enough to be resolved by the algorithm. Again, power estimates remain positive as even more leakage through the subarray pattern sidelobes occurs in this "dirtier" jamming environment.

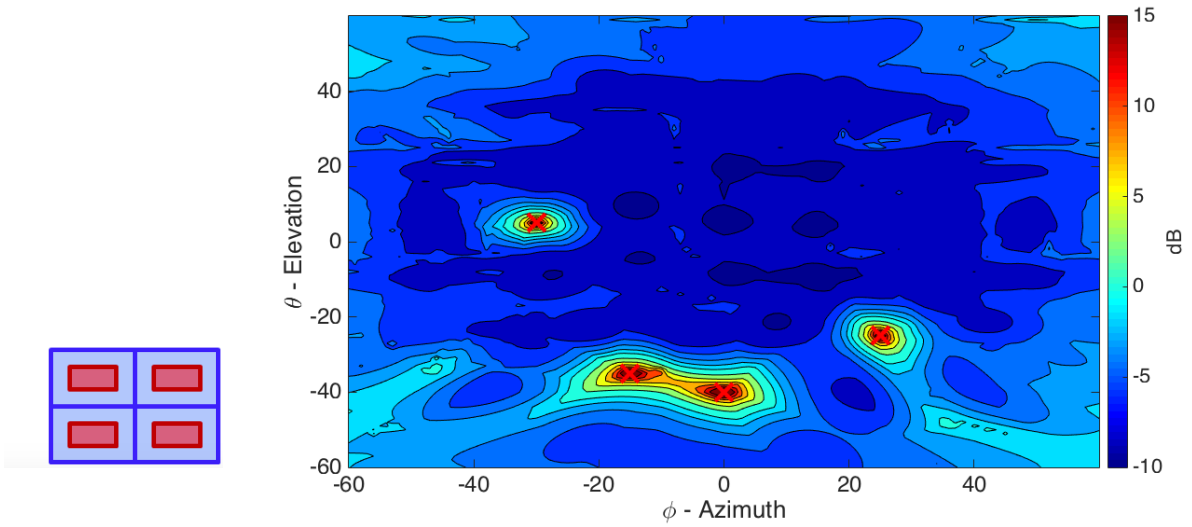

(a) KASPS-ADBF (b) JNSR Output

Figure A-44. JNSR output for the antenna described in Table 5 with Jammers 1-4 from Table 2 present, after KASPS-ADBF is applied using jammer properties as found by the JPE algorithm. The red X's indicate jammer locations.

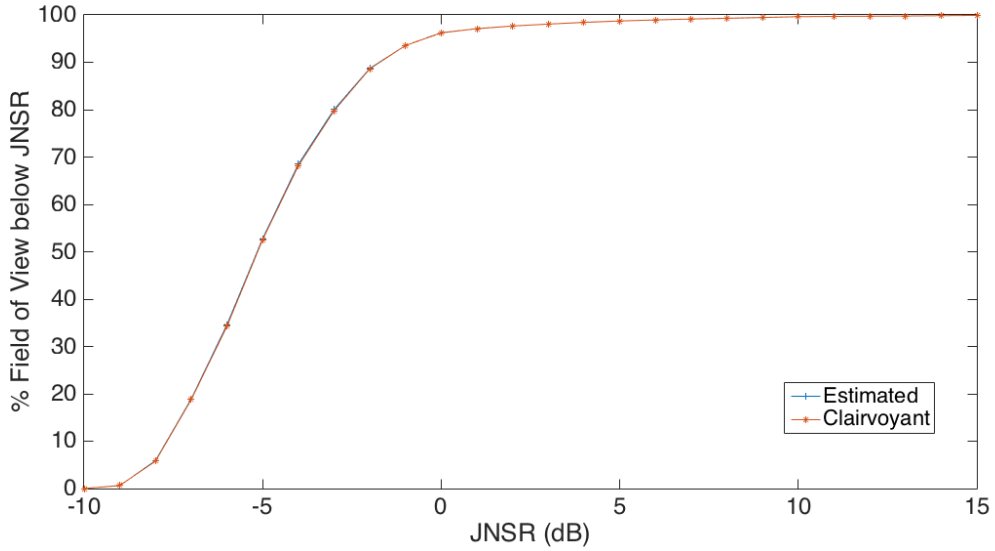

Figure A-45. The "Estimated" curve shows percentage of the look angles from Figure A-44 for which JNSR is less than the x-axis value. A curve depicting the KASPS-ADBF response for clairvoyantly known jammer parameters (as in Figure 25) is shown for reference.

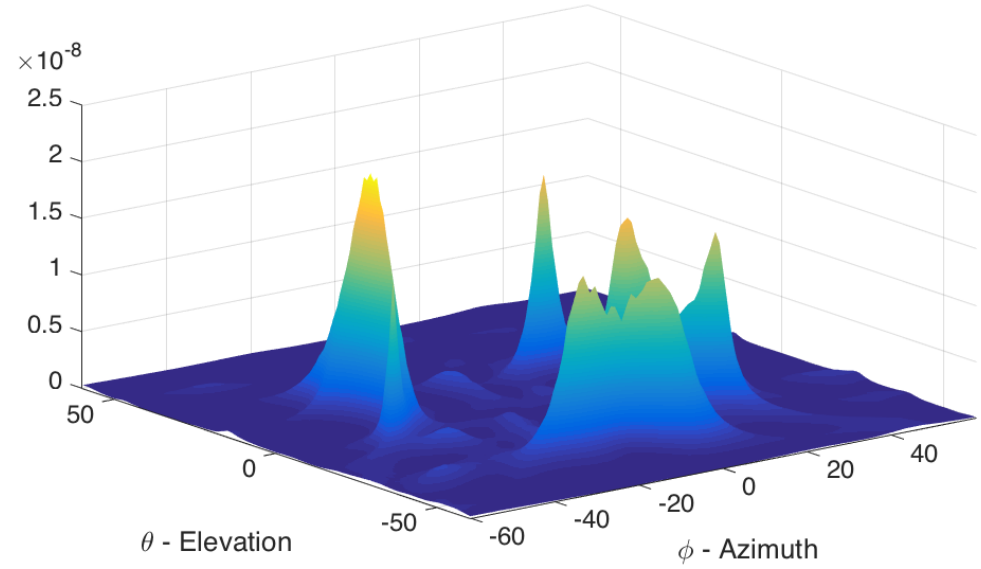

(a) Angled View

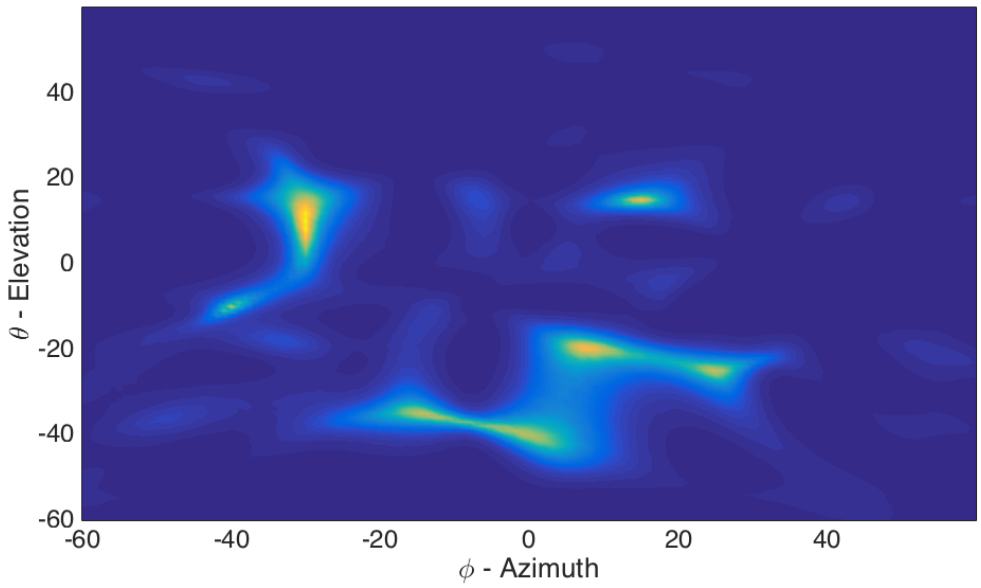

(b) Birds Eye View

Figure A-46. The minimum variance spectrum, $\hat{\mathbf{P}}_{MV,ch}$, as estimated from the JPE algorithm in the environment including the antenna from Table 5 and Jammers 1-8 from Table 2 shown from two vantage points. The spectrum values (z-axis) are purely relative.

Table 9. Jammer parameters ascertained by the JPE algorithm, as described in Section A.2, in the environment containing the antenna from Tabe 5 and Jammers 1-8 from Table 2.

Jam. Det.	ϕ (^{o})	θ (^{o})	$\frac{S_j}{R_j^2}$ (W)	ϕ Error (^{o})	θ Error (^{o})	$\frac{S_j}{R_j^2}$ Error (W)
1	-30	10	1.60 x 10^{-8}	0	+5, -5	N/A
2	25	-25	1.11 x 10^{-8}	0	0	+1.1 x 10^{-9}
3	-15	-35	1.29 x 10^{-8}	0	0	+2.9 x 10^{-9}
4	0	-40	1.46 x 10^{-8}	0	0	+4.6 x 10^{-9}
5	15	15	1.09 x 10^{-8}	0	0	+0.9 x 10^{-9}
6	-40	-10	1.36 x 10^{-8}	0	0	+3.6 x 10^{-9}
7	8	-20	1.10 x 10^{-8}	0	0	+1.0 x 10^{-9}

Bibliography

1. P. M. Corbell, "Adaptive illumination patterns for radar applications," Ph.D. dissertation, Air Force Institute of Technology, 2006.

2. J. Ward, "Space-time adaptive processing for airborne radar," Massachusetts Institute of Technology, Tech. Rep. 1015, 1994.

3. T. B. Hale, "Airborne radar interference suppression using adaptive three-dimensional techniques," Ph.D. dissertation, Air Force Institute of Technology, 2002.

4. A. Jaffer, M. Baker, W. Ballance, and J. Staub, "Adaptive space-time processing techniques for airborne radars," *Contract F30602-89-D-0028, Hughes Aircraft Company, Fullerton, CA*, vol. 92634, 1991.

5. R. Mailloux, *Phased array antenna handbook.* Boston, MA: Artech House, 1994.

6. R. Klemm, *Applications of space-time adaptive processing.* London: Institution of Electrical Engineers, 2004.

7. H. Hang and X. Pan, "Two-dimensional spatial spectrum estimation direction finding method at subarray level," in *IEEE Antennas and Propagation Society International Symposium*, vol. 2B, July 2005, pp. 374–377 vol. 2B.

8. U. Nickel, "Spotlight MUSIC: super-resolution with subarrays with low calibration effort," *IEEE Proceedings on Radar, Sonar and Navigation*, vol. 149, no. 4, pp. 166–173, August 2002.

9. G. Sanford and L. Klein, "Increasing the beamwidth of a microstrip radiating element," in *Antennas and Propagation Society International Symposium, 1979*, vol. 17, Jun 1979, pp. 126–129.

10. C. A. Balanis, *Antenna Theory: Analysis and Design, 3rd Edition.* Hoboken, NJ: Wiley-Interscience, 2005.

11. R. K. Hersey, "Adaptive detection and estimation using a conformal array antenna," Ph.D. dissertation, Georgia Institute of Technology, 2004.

12. T. B. Hale, "EENG 668: Advanced radar systems analysis," Class Notes, 3 2006, air Force Institute of Technology.

13. I. Reed, J. Mallett, and L. Brennan, "Rapid convergence rate in adaptive arrays," *IEEE Transactions on Aerospace and Electronic Systems*, vol. AES-10, no. 6, pp. 853–863, Nov 1974.

14. General Services Administration, *Federal Standard 1037C Telecommunications: Glossary of Telecommunication Terms*. National Communications Systems, US Goverment, August 1996. [Online]. Available: http://www.its.bldrdoc.gov/fs-1037/fs-1037c.htm

15. T. Brockett and Y. Rahmat-Samii, "Subarray design diagnostics for the suppression of undesirable grating lobes," *IEEE Transactions on Antennas and Propagation*, vol. 60, no. 3, pp. 1373–1380, March 2012.

16. J. Ruze, "The effect of aperture errors on the antenna radiation pattern," *Il Nuovo Cimento (1943-1954)*, vol. 9, pp. 364–380, 1952.

17. Z. Zhang, Q. Ding, K. Liu, H. Zhao, and G. Liu, "Array manifold calibration in shipborne radar," in *Second International Conference on Innovations in Bio-inspired Computing and Applications (IBICA)*, Dec 2011, pp. 156–159.

18. J. Rao, T. Cheston, J. Choe, M. Parent, and P. Hughes II, "Phased arrays with sub-array architecture," in *IEEE International Conference on Phased Array Systems and Technology Proceedings*, 2000, pp. 453–456.

19. C. Lin and H. Ly, "Sidelobe reduction through subarray overlapping for wideband arrays," in *Proceedings of the 2001 IEEE Radar Conference*, 2001, pp. 228–233.

20. S. Rengarajan and J. Rao, "Arrays of overlapping sub-arrays for improved sidelobe level performance," in *IEEE International Conference on Phased Array Systems and Technology Proceedings*, 2000, pp. 497–500.

21. A. H. Nuttall, "Some windows with very good sidelobe behavior," *IEEE Transactions on Acoustics, Speech and Signal Processing*, vol. 29, no. 1, pp. 84–91, Feb 1981.

22. U. Nickel, "Subarray configurations for digital beamforming with low sidelobes and adaptive interference suppression," in *Record of the IEEE 1995 International Radar Conference*, May 1995, pp. 714–719.

23. S. Applebaum and D. Chapman, "Adaptive arrays with main beam constraints," *IEEE Transactions on Antennas and Propagation*, vol. 24, no. 5, pp. 650–662, Sep 1976.

24. L. L. Horowitz, H. Blatt, W. G. Brodsky, and K. D. Senne, "Controlling adaptive antenna arrays with the sample matrix inversion algorithm," *NASA STI/Recon Technical Report A*, vol. 80, p. 23283, 1979.

25. C. Baird and G. Rassweiler, "Adaptive sidelobe nulling using digitally controlled phase-shifters," *IEEE Transactions on Antennas and Propagation*, vol. 24, no. 5, pp. 638–649, Sep 1976.

26. R. Shore, "Nulling a symmetric pattern location with phase-only weight control," *IEEE Transactions on Antennas and Propagation*, vol. 32, no. 5, pp. 530–533, May 1984.

27. S. Smith, "Optimum phase-only adaptive nulling," *IEEE Transactions on Signal Processing*, vol. 47, no. 7, pp. 1835–1843, Jul 1999.

28. K. McDonald and R. Blum, "Analytical analysis of stap algorithms for cases with mismatched steering and clutter statistics," in *The Record of the 1999 IEEE Radar Conference*, 1999, pp. 267–272.

29. R. Klemm, *Space-time adaptive processing : principles and applications*. London: Institution of Electrical Engineers, 1998.

30. N. Wiener, *Extrapolation, interpolation, and smoothing of stationary time series with engineering applications*. Cambridge, MA: Technology Press of the Massachusetts Institute of Technology, 1964.

31. N. Wiener and E. Hopf, "On a class of singular integral equations," *Proc. Prussian Acad., Math.-Phys. Ser*, p. 696, 1931.

32. B. Widrow and J. McCool, "A comparison of adaptive algorithms based on the methods of steepest descent and random search," *IEEE Transactions on Antennas and Propagation*, vol. 24, no. 5, pp. 615–637, Sep 1976.

33. R. A. Monzingo, *Introduction to Adaptive Arrays (Electromagnetics and Radar)*. SciTech Publishing, 2011.

34. G. Niezgoda, J. Krolik, and D. Swingler, "Broadband adaptive beamforming in the presence of transient interference," Concordia University, Tech. Rep., 1994.

35. H. Cox, "Multi-rate adaptive beamforming (MRABF)," in *Proceedings of the 2000 IEEE Sensor Array and Multichannel Signal Processing Workshop*, 2000, pp. 306–309.

36. ——, "Multi-rate adaptive nulling of moving interferers," ORINCON Corporation, Tech. Rep., 2000.

37. D. Rabideau, "Closed-loop multistage adaptive beamforming," in *Conference Record of the Thirty-Third Asilomar Conference on Signals, Systems, and Computers*, vol. 1, Oct 1999, pp. 98–102 vol.1.

38. D. Rabideau and M. Zatman, "Closed-loop multistage beamformer," Jul. 22 2003, uS Patent 6,598,014. [Online]. Available: http://www.google.com/patents/US6598014

39. D. Rabideau, "Multistage adaptation for large digital arrays," Massachusetts Institute of Technology, Tech. Rep., 1999.

40. J. Guerci and E. Baranoski, "Knowledge-aided adaptive radar at DARPA: an overview," *IEEE Signal Processing Magazine*, vol. 23, no. 1, pp. 41–50, Jan 2006.

41. R. Schmidt, "Multiple emitter location and signal parameter estimation," *IEEE Transactions on Antennas and Propagation*, vol. 34, no. 3, pp. 276–280, Mar 1986.

42. J. Capon, "Probability distributions for estimators of the frequency-wavenumber spectrum," *Proceedings of the IEEE*, vol. 58, no. 10, pp. 1785–1786, Oct 1970.

43. S. Reddi, "Multiple source location-a digital approach," *IEEE Transactions on Aerospace and Electronic Systems*, vol. AES-15, no. 1, pp. 95–105, Jan 1979.

44. A. Berni, "Angle-of-arrival estimation using an adaptive antenna array," *IEEE Transactions on Aerospace and Electronic Systems*, vol. AES-11, no. 2, pp. 278–284, March 1975.

45. S. K. Mitra, *Digital Signal Processing: A Computer-Based Approach*, 4th ed. New York, NY: McGraw-Hill School Education Group, 2006.

REPORT DOCUMENTATION PAGE

Form Approved
OMB No. 0704–0188

1. REPORT DATE *(DD–MM–YYYY)*	2. REPORT TYPE	3. DATES COVERED *(From — To)*
03–24–2016	Master's Thesis	Sept 2014 — Mar 2016

4. TITLE AND SUBTITLE

Interference Suppression Using Knowledge-Aided Subarray Pattern Synthesis

5a. CONTRACT NUMBER

5b. GRANT NUMBER

5c. PROGRAM ELEMENT NUMBER

6. AUTHOR(S)

New, David A., 1 Lt, USAF

5d. PROJECT NUMBER

5e. TASK NUMBER

5f. WORK UNIT NUMBER

7. PERFORMING ORGANIZATION NAME(S) AND ADDRESS(ES)

Air Force Institute of Technology
Graduate School of Engineering and Management (AFIT/EN)
2950 Hobson Way
WPAFB OH 45433-7765

8. PERFORMING ORGANIZATION REPORT NUMBER

AFIT-ENG-MS-16-M-037

9. SPONSORING / MONITORING AGENCY NAME(S) AND ADDRESS(ES)

Intentionally Left Blank

10. SPONSOR/MONITOR'S ACRONYM(S)

11. SPONSOR/MONITOR'S REPORT NUMBER(S)

12. DISTRIBUTION / AVAILABILITY STATEMENT

DISTRIBUTION STATEMENT A:
APPROVED FOR PUBLIC RELEASE; DISTRIBUTION UNLIMITED.

13. SUPPLEMENTARY NOTES

14. ABSTRACT

Phased array systems typically subarray many antenna elements into far fewer digitized channels, to the point where just one subarray may theoretically have many more spatial degrees of freedom DOF than digital DOF afforded from the number of digitized channels, C. More DOF yields better performance, but adding more channels drives system cost and data throughput requirements. DOF within the subarrays could be designed to mitigate selected interference signals at the subarray pattern stage if the antenna manifold and the angle of arrival AOA of interference sources are known. A jammers AOA can be derived from additional knowledge sources and/or algorithmic processing of the channel data. Simulations are used to illustrate important implementation trades and a notional concept of operation for dividing spatial nulling duties between real and digital beamformers.

15. SUBJECT TERMS

phased array, subarray, electronic protection, adaptive nulling

16. SECURITY CLASSIFICATION OF:			17. LIMITATION OF ABSTRACT	18. NUMBER OF PAGES	19a. NAME OF RESPONSIBLE PERSON
a. REPORT	b. ABSTRACT	c. THIS PAGE			Lt Col P. M. Corbell, AFIT/ENG
U	U	U	UU	108	19b. TELEPHONE NUMBER *(include area code)* (937) 255-3636, x4370; phillip.corbell@afit.edu